Chapter 15

Wing Scans: Analysis

Terrance J. Gaetz

In this chapter we discuss the analysis of the wing scan experiment at XRCF. The experiment was designed to map out the far wings of the Point Spread Function, or PSF, at angles $\gtrsim$1 mm (about 20″ away from the core) by using a series of pinhole scans across the PSF. Because of time constraints, only selected portions of the wings could be mapped in detail; a series of horizontal (Y) or vertical (Z) pinhole scans were sampled using pinhole diameters of 1, 4, 10, 20, and 35 mm. Quadrant shutters were used to isolate quadrants of individual mirror pairs; in order to provide illumination of the surface more nearly resembling on-orbit conditions, the HRMA was also pitched or yawed by the mean graze angle for the shell in question. The experiment, the reduction of the X-ray data, and the raytrace simulations of the pinhole measurements are discussed in more detail in Chapter 14.

The analysis of these data can provide information about two properties of the mirror: First, they allow the measurement of the RMS surface roughness of the mirrors, and a diagnosis of the amount of dust on the optics (if any). Second, by simply looking at the surface brightness as a function of off-axis angle, we can extrapolate the wings of the point spread function to discover how much of the effective area falls outside of the largest pinhole used in the Encircled Energy tests. This allows us to correct the measured effective areas at selected energies for scattering beyond the largest aperture used.

In this chapter we discuss the analysis of X-ray wing scan data and the analysis of raytrace simulations of the wing scan experiment. The knowledge of the PSD based on the mirror metrology measurements is briefly discussed. The pinhole effective areas are combined to form surface brightness profiles for each of the sampled quadrants and energies, and the surface brightness profiles are in turn combined into PSD's in the form of "$2W_1$" profiles. As a consistency check, the surface brightness profile is compared to that obtained by differentiating the effective area function in the one case which permits a relatively low-noise numerical derivative.

15.1 PSD based on HDOS metrology

Prior to X-ray testing at XRCF, knowledge of the microroughness of the HRMA optics depended on measurements of the HRMA mirror metrology performed at the Hughes Danbury Optical Systems, Inc. (HDOS) in Danbury, CT. Measurements were performed for each mirror after final polishing but before the mirror was shipped to OCLI for coating. The instruments used in the metrology were the CIDS (Circularity and Inner Diameter Station), the PMS (Precision Metrology

Station), and the MPMI or WYKO (Micro Phase Measuring Interferometer, a slightly modified WYKO Corporation instrument). The CIDS was used to determine circularity and the inner diameters of the HRMA shells. The PMS was used to measure along meridians. With these two instruments, HDOS essentially measured both the 'hoops' and 'staves' of each 'barrel' (optic), and thus mapped the entire surface. Finally, microroughness was sampled on each mirror using the WYKO.

The HDOS mirror metrology was processed by the AXAF Telescope Scientist into a low-frequency mirror map (based on PMS axial scan data and CIDS circularity data) and high frequency errors (based on WYKO measurements). These data were split into two pieces and processed into a mirror map for low-frequency errors (modeled in the raytrace using 2D splines periodic in one direction) and high frequency components (treated in the raytrace statistically as a scattering component).

The mirror map files represent a combination of PMS axial scan data and CIDS circularity data. Each of these files had solid body translations and rotations removed and was divided into two complementary maps by passing the data through a filter; the low pass portions were combined with the modeled distortions induced by the mirror supports (1G and epoxy-induced distortions), fit with 2D spline functions, and used deterministically in the ray-tracing. The high frequency portions were combined with the WYKO data and treated statistically in the raytraces. The standard HDOS filter was used for the separation; the parameters were such that the transition between low and high frequency pass bands occurred from 0.02 to 0.03 mm^{-1}.

The WYKO data at each magnification ($\times$1.5, $\times$10, and $\times$40) were combined into mean PSD files, and these files were processed with the program `foldw1` (which is similar to the HDOS program `eegraz`) to calculate scattering distributions. The calculation was based on the Kirchoff theory of scattering Beckmann and Spizzichino (1963). The PSD files do not agree perfectly in the overlap regions, so a linear weighting was used in the overlap regions such that the weight given to the lower frequency file would decrease from 1.0 to 0.0 while the weight given to the high frequency file would increase from 0.0 to 1.0. The frequency intervals are, in units of mm^{-1}, 0.000 to 0.226, 0.226 to 0.5, 0.5 to 1.5, 1.5 to 2.0, 2.0 to 5.0, 5.0 to 10.0, and 10.0 to 1000.0.

Because the mirror surface roughness is worse near the end of each mirror, the PSDs were calculated for a set of axial zones (ranging from 5 to 11 zones) for each optic, with a center zone covering about 80% of the mirror surface and end zones covering the rest.

15.2 Surface Brightness Profiles

Once the wing scan pinhole effective areas are obtained (see Chapter 14), the next level of processing is to stitch together the pinhole effective areas into surface brightness profiles for a given shell, quadrant, and energy. The pinhole effective area is converted to a surface brightness, ψ, normalized to the effective area within a 35 mm diameter pinhole on-axis and scaled by a factor of $2 \times 88/360$ to account for the fact that the experiment used a single quadrant at a time. The effective area measured within a 35 mm diameter on-axis pinhole will be denoted A_{eff}^{tot}; in the raytrace simulation, A_{eff}^{tot} was evaluated from an on-axis raytrace with a 35 mm diameter pinhole at the appropriate axial location.

The *scaled* on-axis 35 mm effective area is a_{eff}^{tot}, where

$$a_{\mathit{eff}}^{tot} = 2 \times \frac{88}{360} A_{\mathit{eff}}^{tot}. \tag{15.1}$$

The factor 88/360 arises because each "quadrant" is really 88° (because of the overlap of adjacent closed quadrants). The factor of 2 comes about because scattering is predominantly in-plane so

that the scattered flux at a given off-axis location comes primarily from two opposing portions of the mirror; having only one shutter open should provide about half the flux, provided that the pinhole doesn't actually contain the core of the PSF. This factor should be verified by raytrace experiments; however, obtaining sufficiently small errors would require significantly longer raytraces than performed thus far.

The surface brightness is estimated as

$$\psi = w \times \frac{A_{\mathit{eff}}}{a_{\mathit{eff}}^{tot}} \times \frac{4F_{fc}^2}{\pi d^2}, \tag{15.2}$$

where w is a wing correction factor (see below), F_{fc} is the telescope finite conjugate focal length (taken to be 10.252500 m), A_{eff} is the measured effective area through the off-centered aperture of diameter d obtained as part of the wingscan test, and a_{eff}^{tot} the rescaled on-axis 35 mm effective area with all four quadrants exposed (see Eq. Eq. 15.1).

The surface brightness, ψ, should really be normalized to $\int_{2\pi} \psi \, d\Omega = 1$; by normalizing to a 35 mm diameter pinhole we neglect the flux which falls outside the pinhole. This is at most a 4% **(TBR)** effect for the XRCF data (and usually smaller), and an even smaller effect in the case of the current raytrace simulations.

In evaluating the surface brightness, the pinhole effective areas need to be corrected for the fact that the pinhole has a finite diameter and samples the wings of a PSF which is falling steeply with radius. Consequently, the flux can vary strongly with position within the pinhole; in some cases the pinhole diameter is as large as the pinhole off-axis distance, so the effect can be significant. The analysis currently assumes that the brightness falls as a power law across the width of a pinhole, *i.e.*

$$\psi = \psi_0 \theta^{-\gamma}, \tag{15.3}$$

with γ constant across the pinhole. The pinhole correction then becomes the factor

$$w \approx \frac{1}{{}_2F_1\left(\frac{\gamma}{2}, \frac{\gamma}{2}, 2; \frac{a^2}{r^2}\right)} \tag{15.4}$$

where a is the pinhole radius, r is the off-axis distance, and ${}_2F_1$ is a hypergeometric function.

The value of γ was obtained by using the local logarithmic derivative of the fit function (Eq. 15.5) at the location of the pinhole center (see below).

The surface brightness data are fit with functions of the form

$$\psi(R) = aR^{-b}e^{-R/c} \tag{15.5}$$

where R is the distance (in mm) in the $Y - Z$ plane of the pinhole center from the finite conjugate focus; R is related to off-axis angle θ by

$$\theta \approx R/F_{fc}, \tag{15.6}$$

where F_{fc} is the distance from the HRMA node to the finite conjugate focus.

It is necessary to obtain the wing correction iteratively. We begin by assuming $\gamma = 2$, compute surface brightnesses, and fit the surface brightness to an exponentially truncated power law (Eq. Eq. 15.5). In the case of $\gamma = 2$, the hypergeometric function reduces to

$${}_2F_1\left(1, 1, 2; \frac{a^2}{r^2}\right) = -\frac{\ln(1-z)}{z} \tag{15.7}$$

We take the logarithmic derivative of this function to obtain the local power-law index γ at each data point θ, recompute the wing correction using the hypergeometric function, and iterate until

$$\Delta \equiv \sum_{\text{ap pos}} \left(\frac{w_{old} - w_{new}}{w_{old}} \right)^2 \leq 0.01 \tag{15.8}$$

or 5 iterations, whichever is smaller. In the case of the data from raytrace simulations, 5 iterations were always performed. The raytrace data are not fit well by this form; the raytrace surface brightness profiles contain much structure from the underlying assumed surface PSD, so an unconstrained fit can be a poor approximation to the overall data set. In particular, in attempting to reduce large χ^2 contributions from large curvature portions at small radius, the unconstrained fit may introduce a relatively small value for the exponential cutoff scale length so that the fit function cuts off well before the data. It was decided against attempting to fit more realistic functions to the raytrace data; ultimately we need to compare against the fits to the XRCF data, and the sparseness of the XRCF data set would not support a functional form with even more free parameters. In order to reduce the problems with the exponential cutoff scale, the exponential scale length parameter for the raytrace fits was typically limited to a range of values (typically 20 – 10000 mm); the lower limit was a value chosen (by trial and error) to reproduce the overall shape of the curve at large radii. This worked in some cases (*e.g.*, Figure 15.3) but not very well in other cases (*e.g.*, Figure 15.6). For the present we use the same limits for the exponential cutoff, but future analyses should consider applying different limit ranges on a case by case basis. The XRCF data sets were much sparser and this seems to have been less of a problem; see the shell 6 fits, however.

As noted in §14.2.3, vignetting resulting from the adjacent closed quadrant shutters can be significant. Because of this, separate fits were made for scattering towards the optic (*i.e.*, towards larger radii at the focal plane) and away from the optic (towards smaller radii at the focal plane) for each shell, quadrant, and energy. In the case of the raytrace data, the data points subject to vignetting were removed from the plots and the fits; the adopted cutoffs are listed in Table 15.1.

Table 15.1: Wing scan shutter vignetting cutoffs

Shell	Towards optic (mm)	Away from optic (mm)
1	70	500
3	500	30
4	50	500
6	500	500

The XRCF data are compared to the raytrace simulations in the following tables and figures. In the following, §15.2.1 presents the surface brightness data for the shell 1 single quadrant wing scans in the order: quadrant, energy. Similarly, §15.2.2, §15.2.3, and §15.2.4 present the single quadrant wing scan data for shells 3, 4, and 6, respectively. Finally, §15.2.5 presents the surface brightness data for the shell 4 and shell 6 double-quadrant wing scans. Tables 15.2 to 15.8 present the parameters for the fits to the XRCF data points and to the raytrace data. The fits are also used to evaluate the fractional excess effective area falling outside the largest (35 mm diameter pinhole); this is at most ∼4% (**TBR**) in the case of the XRCF data and at most ∼2% (**TBR**) for the raytrace simulations. Note that in most cases the fractional excess effective area is considerably smaller than the worst case.

The agreement between the XRCF data and the raytrace simulations seems to be reasonably good for the smallest pinholes. The data for the 1S scan at Al-Kα seem to show considerably more

scattering in the direction away from the optic than towards the optic. This is also particularly noticeable in all four quadrants for the the Al-Kα scans shell 3, and for quadrant 4S. This effect seems to be less prominent in the other quadrant/shell/energy combinations. The reason for – and significance of – this effect is not well understood at present.

15.2.1 Shell 1 scans

Table 15.2: Surface brightness fits and fractional excess effective area beyond the 35 mm pinhole. (Raytrace simulations and XRCF data, Shell 1)

Type	Quad	Line	Dir	a	b	c	fractional extra area
sim	1T	Al	in	177526.000	2.447	145.081	0.001618
sim	1T	Al	out	100141.600	2.039	32.969	0.001009
sim	1N	Al	in	188074.000	2.414	100.808	0.001539
sim	1N	Al	out	140240.000	2.145	36.331	0.001089
sim	1B	Al	in	229218.000	2.540	354.215	0.002089
sim	1B	Al	out	142126.000	2.074	33.888	0.001309
sim	1S	Al	in	239490.000	2.442	68.289	0.001245
sim	1S	Al	out	135748.000	2.063	32.608	0.001222
sim	1T	Ti	in	638360.000	2.083	22.409	0.002511
sim	1T	Ti	out	491692.000	1.982	20.000	0.002182
sim	1N	Ti	in	651161.000	2.069	22.748	0.002793
sim	1N	Ti	out	544555.000	1.992	20.000	0.002326
sim	1B	Ti	in	715540.000	2.108	23.324	0.002788
sim	1B	Ti	out	514720.000	1.923	20.000	0.002870
sim	1S	Ti	in	709070.000	2.053	20.000	0.002390
sim	1S	Ti	out	495692.000	1.923	20.000	0.002761
xrcf	1T	Al	in	174886.000	2.202	374.817	0.007554
xrcf	1T	Al	out	161181.000	2.061	188.814	0.009362
xrcf	1N	Al	in	146541.000	1.933	48.627	0.004132
xrcf	1N	Al	out	151190.000	1.965	88.460	0.007418
xrcf	1B	Al	in	135389.000	2.271	10000.000	0.008287
xrcf	1B	Al	out	123336.000	1.947	76.618	0.005657
xrcf	1S	Al	in	90294.800	1.837	47.734	0.003680
xrcf	1S	Al	out	209820.000	2.214	10000.000	0.017700
xrcf	1T	Ti	in	588435.000	1.640	32.729	0.028977
xrcf	1T	Ti	out	650222.000	1.713	29.945	0.020186
xrcf	1N	Ti	in	654973.000	1.624	26.366	0.022367
xrcf	1N	Ti	out	741870.000	1.851	39.998	0.021932
xrcf	1B	Ti	in	564424.000	1.803	63.980	0.038846
xrcf	1B	Ti	out	477645.000	1.605	27.270	0.018891
xrcf	1S	Ti	in	518891.000	1.634	30.179	0.022434
xrcf	1S	Ti	out	686177.000	1.759	32.517	0.020691

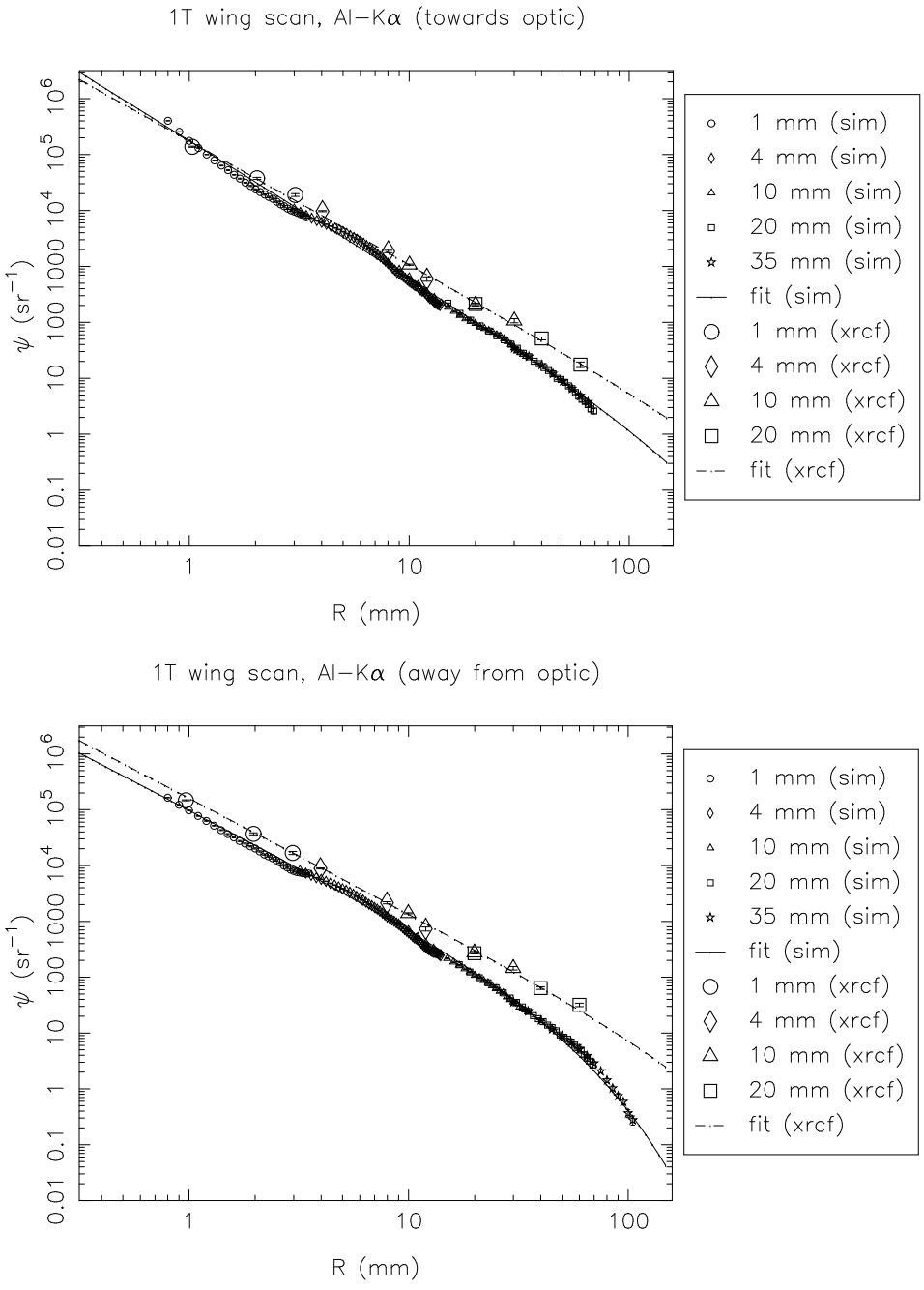

Figure 15.1: Shell 1T: Al-Kα surface brightness, towards and away from the optic

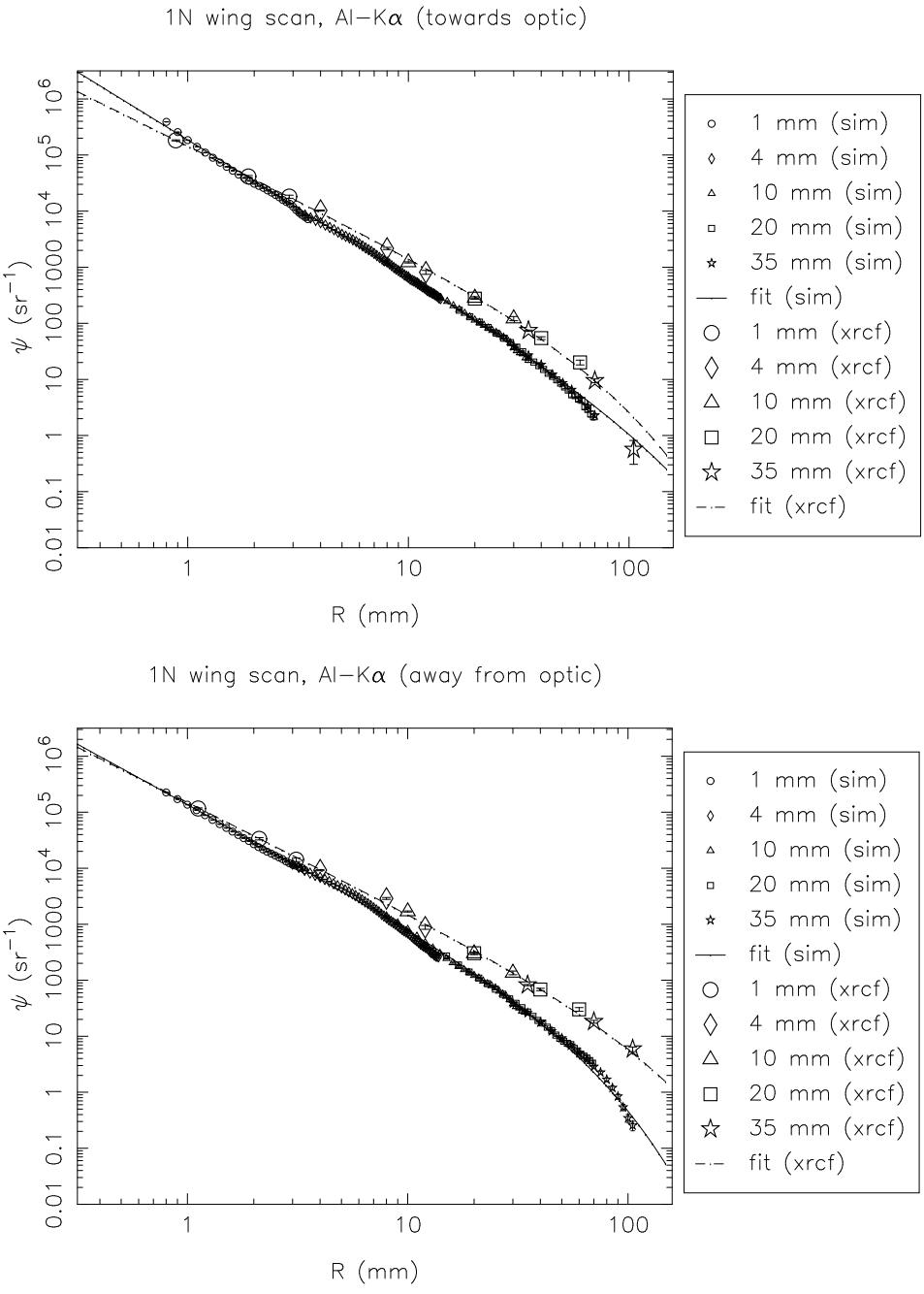

Figure 15.2: Shell 1N: Al-Kα surface brightness, towards and away from the optic

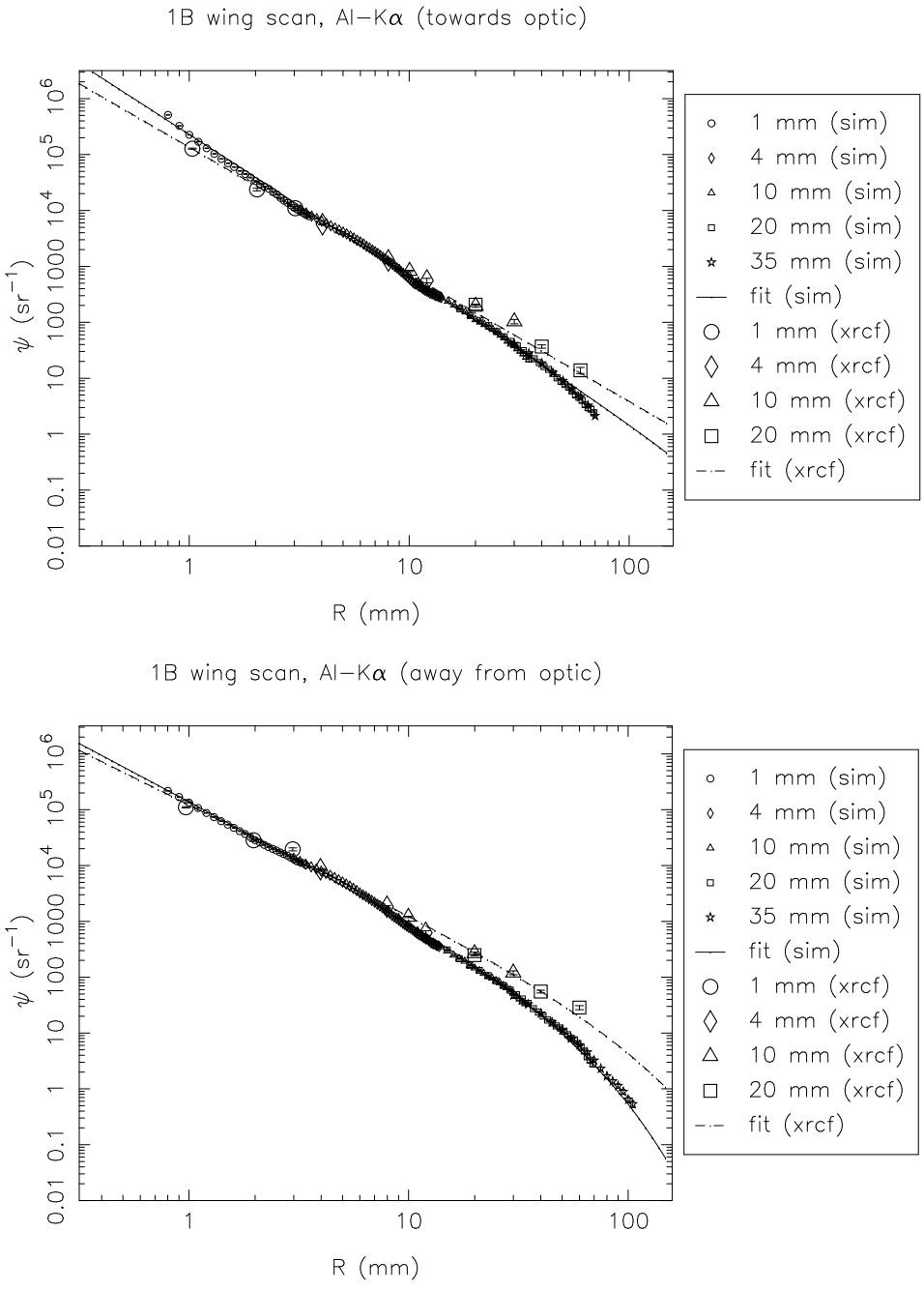

Figure 15.3: Shell 1B: Al-Kα surface brightness, towards and away from the optic

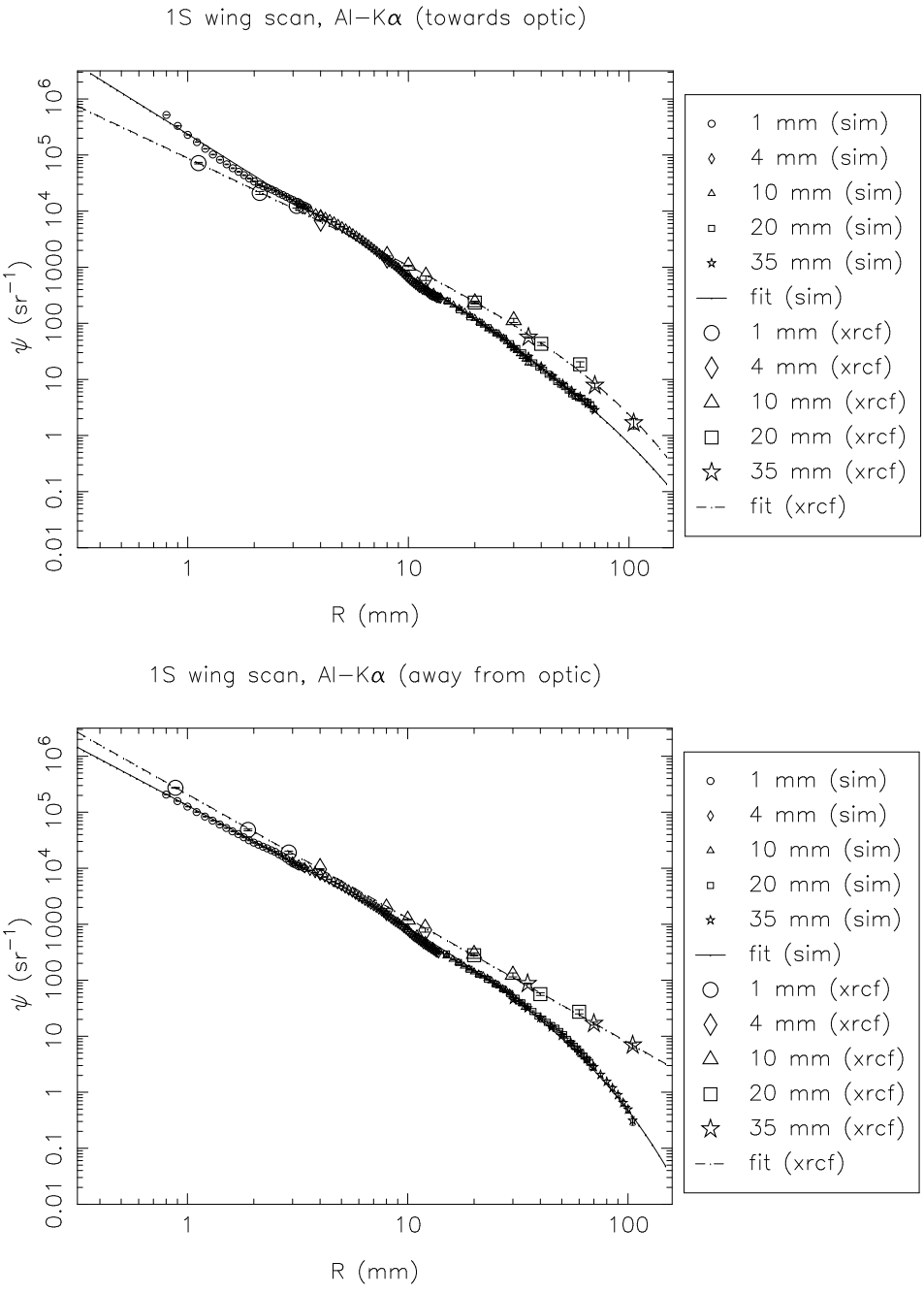

Figure 15.4: Shell 1S: Al-Kα surface brightness, towards and away from the optic

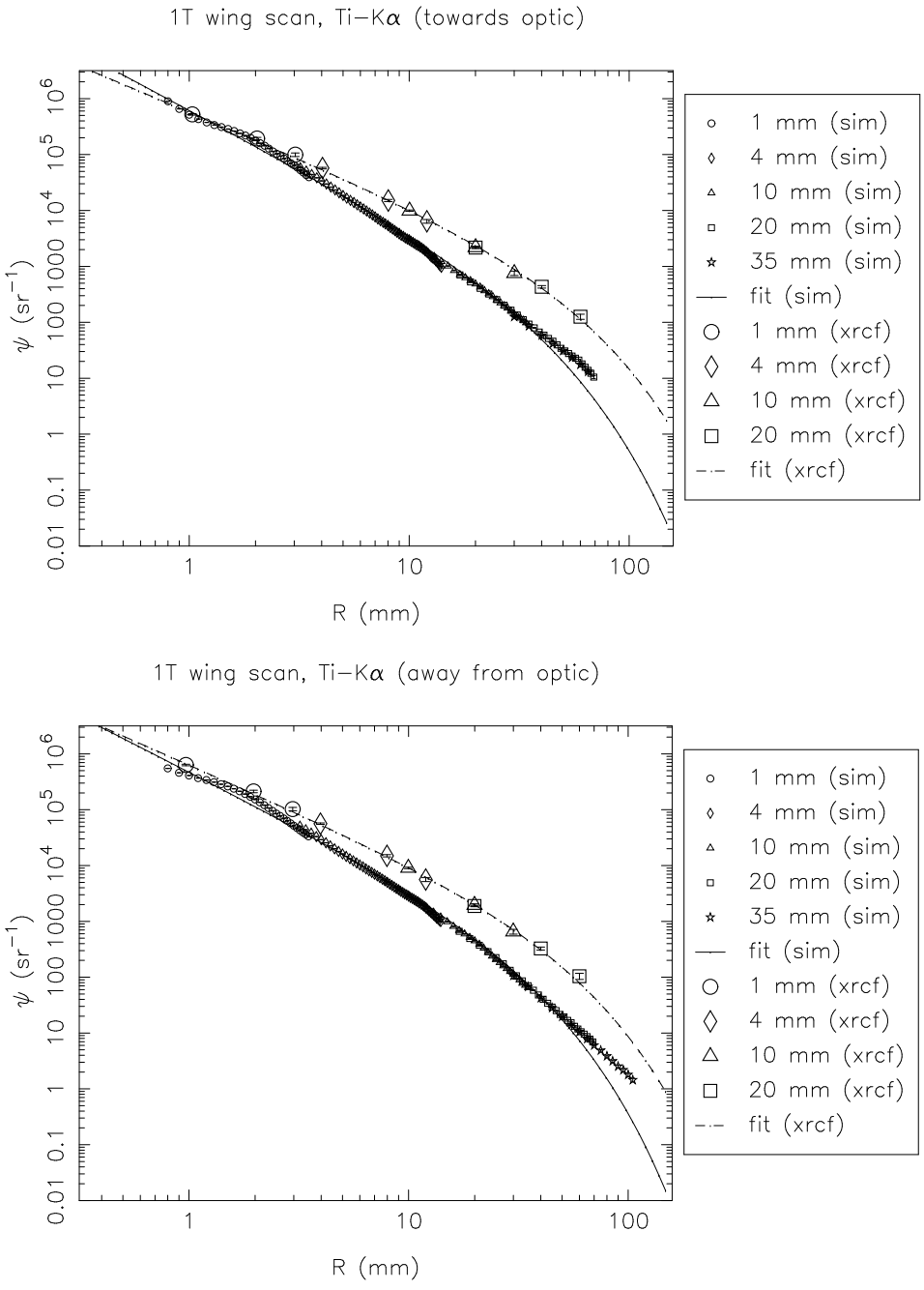

Figure 15.5: Shell 1T: Ti-Kα surface brightness, towards and away from the optic

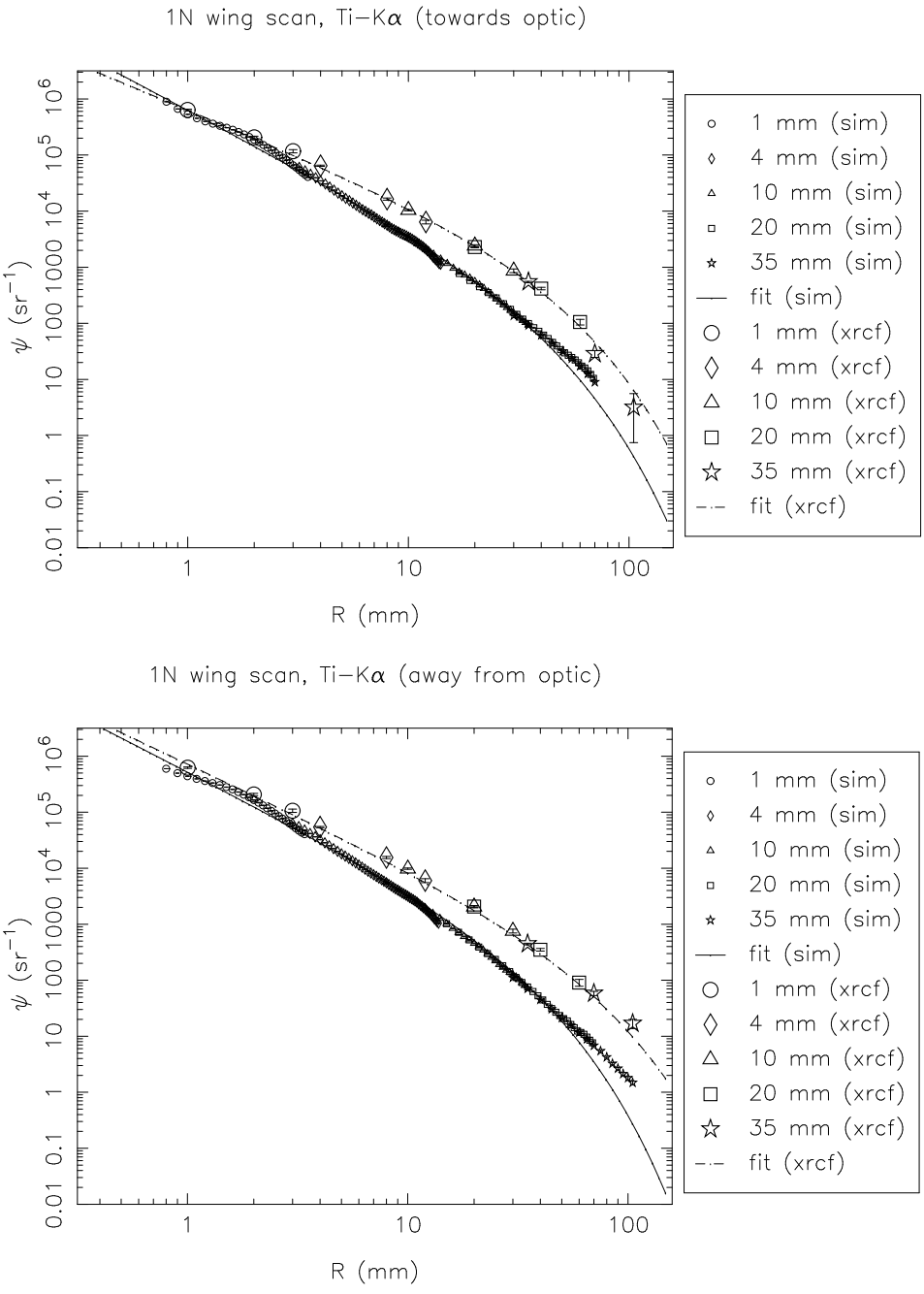

Figure 15.6: Shell 1N: Ti-Kα surface brightness, towards and away from the optic

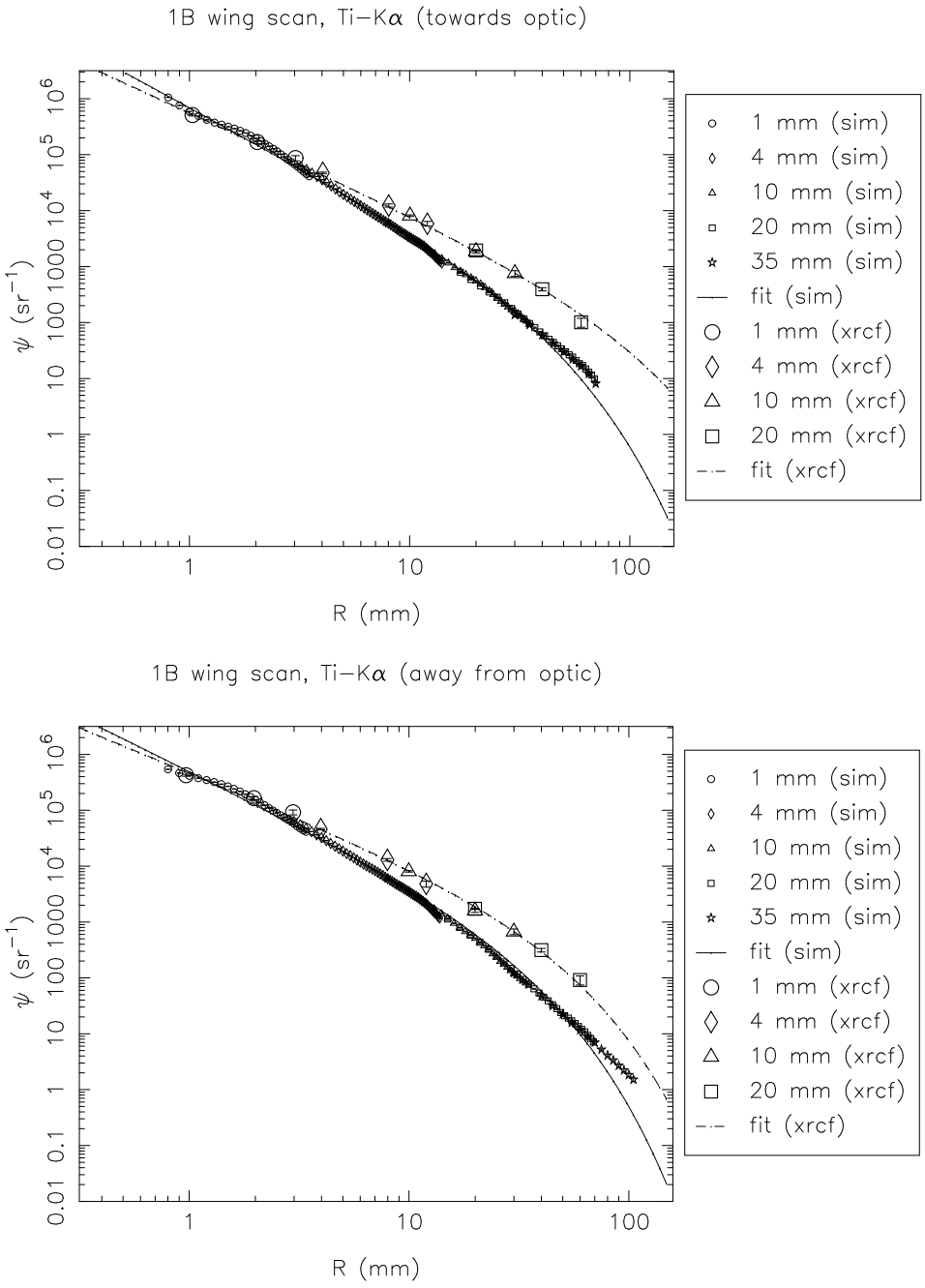

Figure 15.7: Shell 1B: Ti-Kα surface brightness, towards and away from th e optic

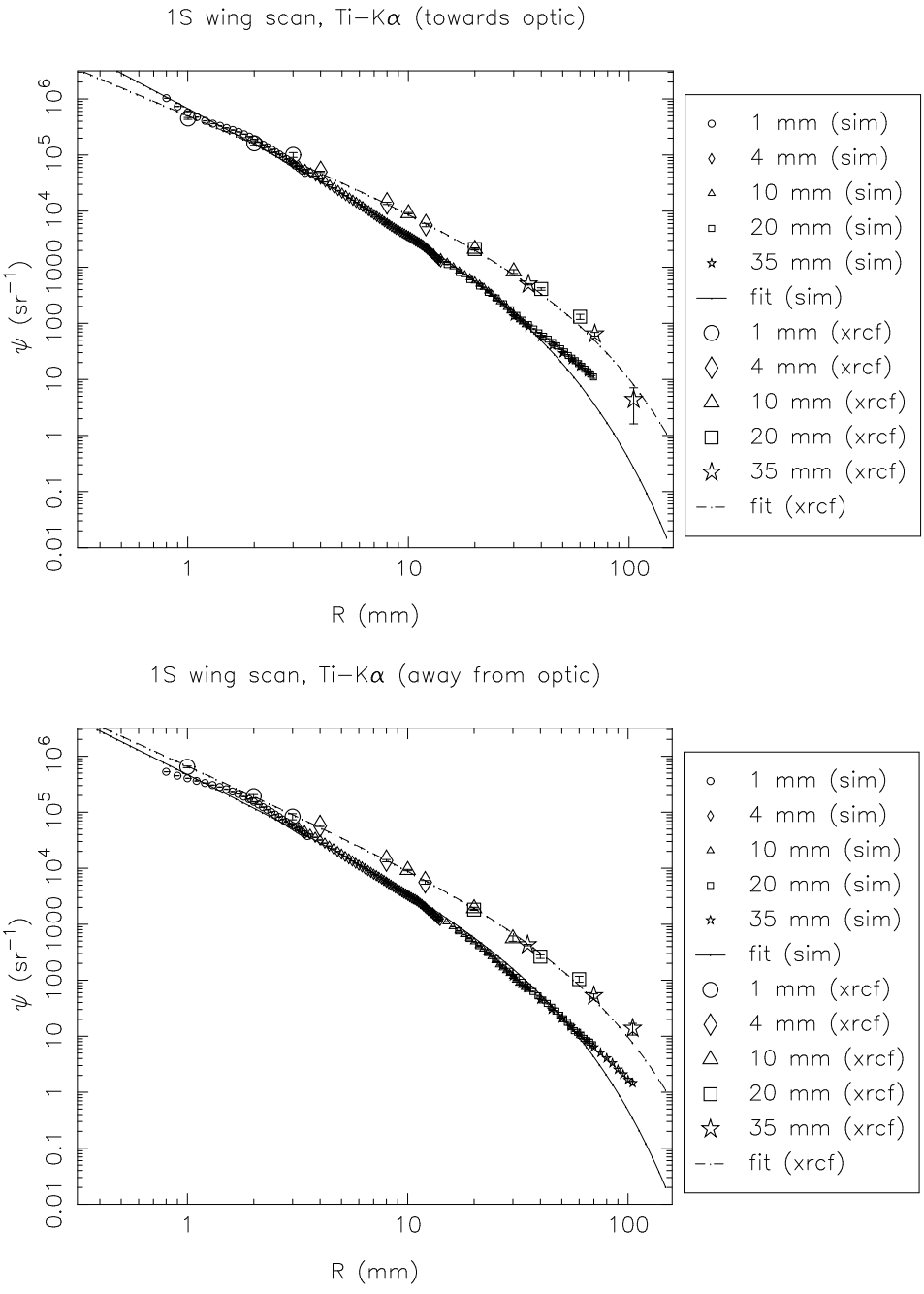

Figure 15.8: Shell 1S: Ti-Kα surface brightness, towards and away from the optic

15.2.2 Shell 3 scans

Table 15.3: Surface brightness fits and fractional excess effective area beyond the 35 mm pinhole. (Raytrace simulations, Shell 3)

Type	Quad	Line	Dir	a	b	c	fractional extra area
sim	3T	Al	in	33670.200	2.630	10000.000	0.000318
sim	3T	Al	out	18158.600	2.123	70.000	0.000361
sim	3N	Al	in	43456.300	2.810	10000.000	0.000173
sim	3N	Al	out	21399.700	2.290	164.721	0.000415
sim	3B	Al	in	33533.400	2.612	10000.000	0.000345
sim	3B	Al	out	20187.700	2.193	70.000	0.000301
sim	3S	Al	in	33600.500	2.621	10000.000	0.000332
sim	3S	Al	out	15612.400	2.026	70.000	0.000466
sim	3S	Ti	in	186937.000	2.570	70.000	0.000591
sim	3S	Ti	out	124877.000	2.335	70.000	0.001034
sim	3S	Cr	in	246429.000	2.579	70.000	0.000749
sim	3S	Cr	out	176035.000	2.408	70.000	0.001081
sim	3T	Fe	in	349548.000	2.561	85.408	0.001361
sim	3T	Fe	out	270453.000	2.539	70.000	0.000968
sim	3B	Fe	in	353953.000	2.603	117.001	0.001461
sim	3B	Fe	out	254630.000	2.510	70.000	0.001028
sim	3N	Fe	in	377381.000	2.626	148.135	0.001626
sim	3N	Fe	out	293686.000	2.532	70.000	0.001081
sim	3S	Fe	in	362943.000	2.575	70.000	0.001125
sim	3S	Fe	out	226964.000	2.524	70.000	0.000866

Table 15.4: Surface brightness fits and fractional excess effective area beyond the 35 mm pinhole. (XRCF data, Shell 3)

Type	Quad	Line	Dir	a	b	c	fractional extra area
xrcf	3T	Al	in	42694.600	2.545	10000.000	0.000615
xrcf	3T	Al	out	139570.000	2.700	10000.000	0.000937
xrcf	3N	Al	in	25452.400	1.980	42.306	0.000486
xrcf	3N	Al	out	123052.000	2.509	71.304	0.000507
xrcf	3B	Al	in	18670.600	1.721	20.099	0.000231
xrcf	3B	Al	out	55033.600	2.205	77.562	0.000863
xrcf	3S	Al	in	16015.000	1.783	30.189	0.000382
xrcf	3S	Al	out	62529.500	2.125	25.698	0.000281
xrcf	3S	Ti	in	278681.000	2.231	122.589	0.005740
xrcf	3S	Ti	out	195982.000	1.925	31.936	0.002944
xrcf	3S	Cr	in	260346.000	2.095	65.196	0.005399
xrcf	3S	Cr	out	310305.000	2.009	25.242	0.002115
xrcf	3T	Fe	in	560465.000	2.253	459.946	0.020630
xrcf	3T	Fe	out	736608.000	2.304	33.052	0.002609
xrcf	3B	Fe	in	568188.000	2.304	232.852	0.012476
xrcf	3B	Fe	out	484538.000	2.107	29.203	0.003001
xrcf	3N	Fe	in	422225.000	2.114	59.864	0.007351
xrcf	3N	Fe	out	563223.000	2.168	21.617	0.001465
xrcf	3S	Fe	in	503919.000	2.113	58.980	0.008658
xrcf	3S	Fe	out	428822.000	2.027	20.240	0.001646

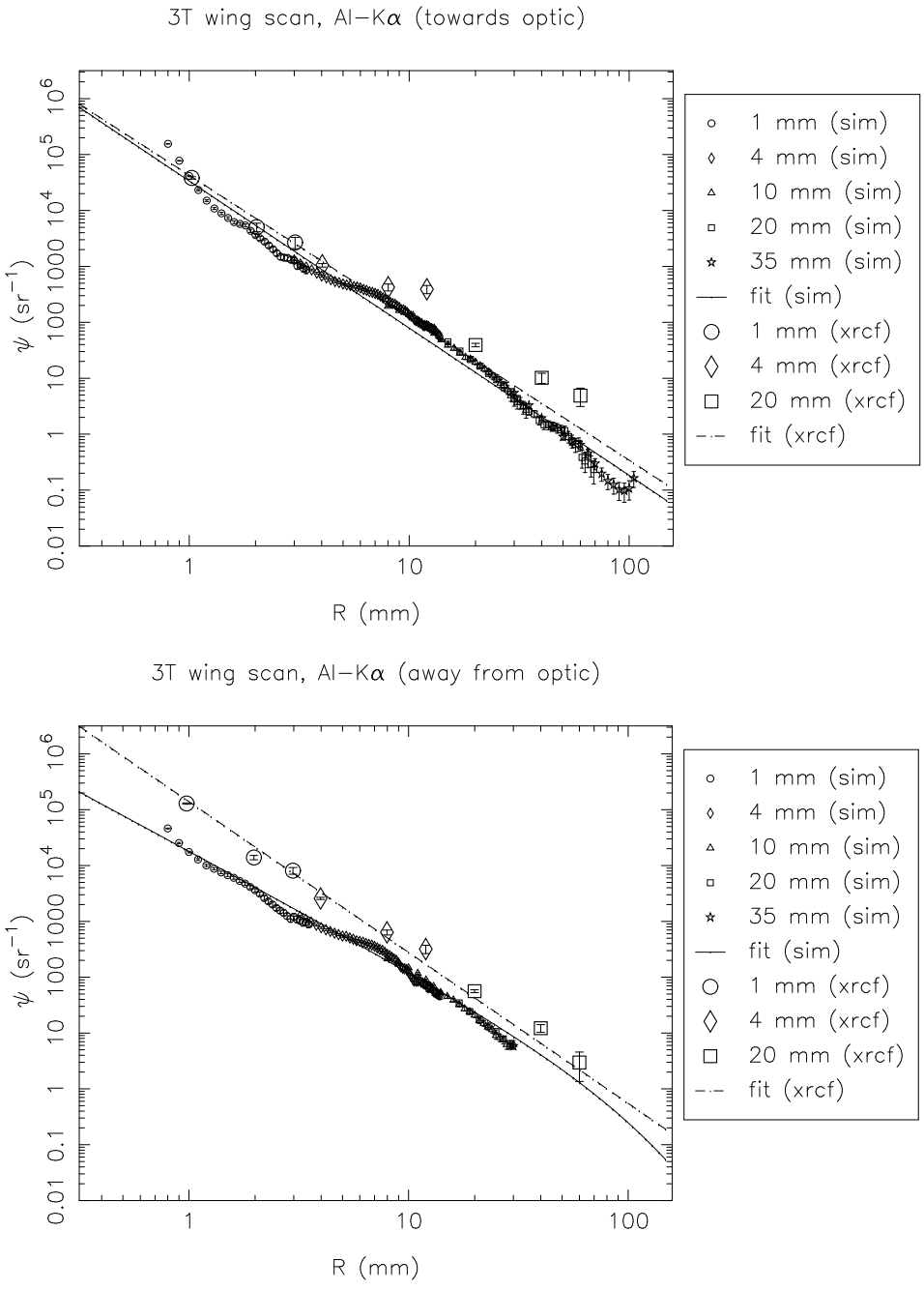

Figure 15.9: Shell 3T: Al-Kα surface brightness, towards and away from the optic

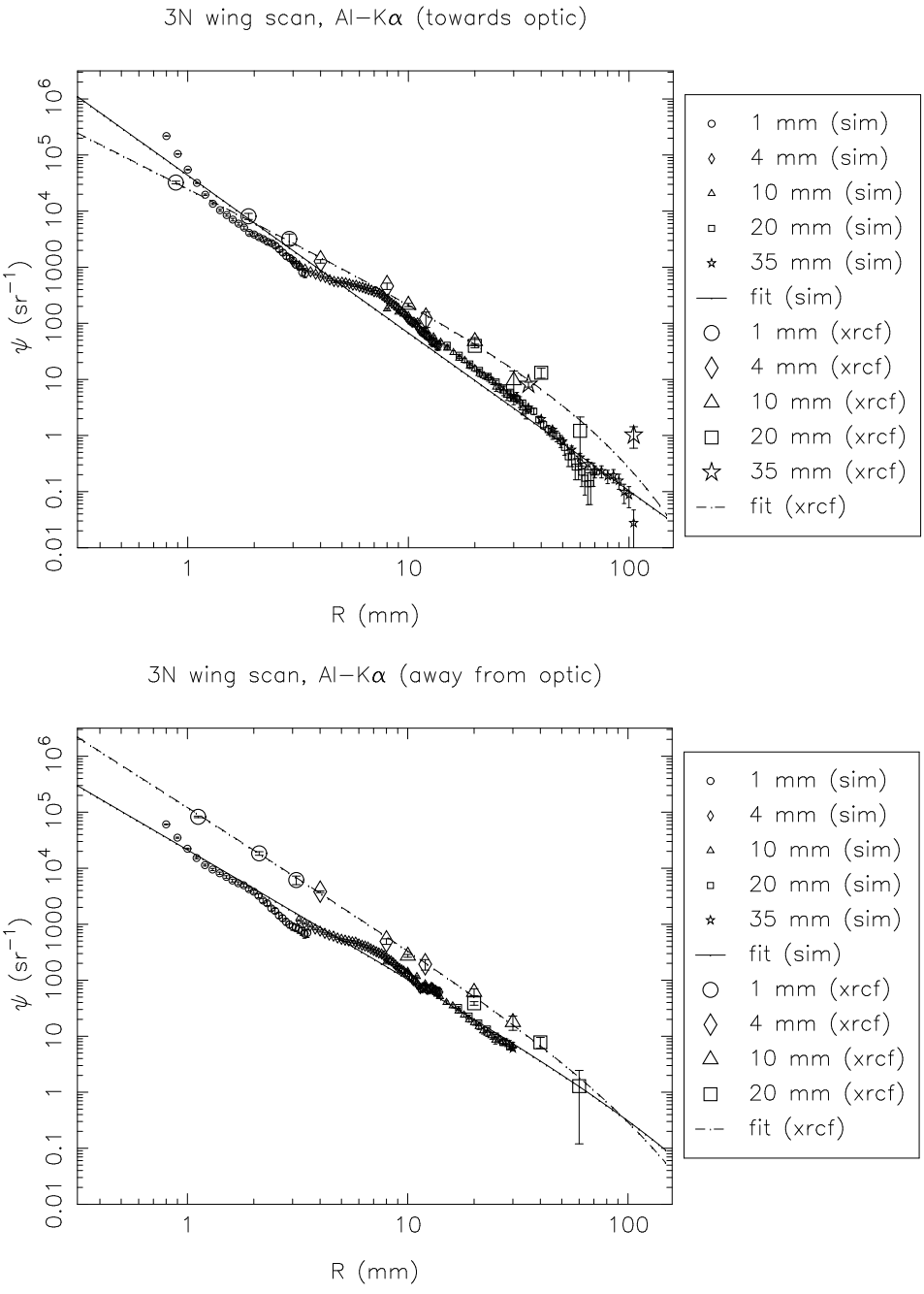

Figure 15.10: Shell 3N: Al-Kα surface brightness, towards and away from the optic

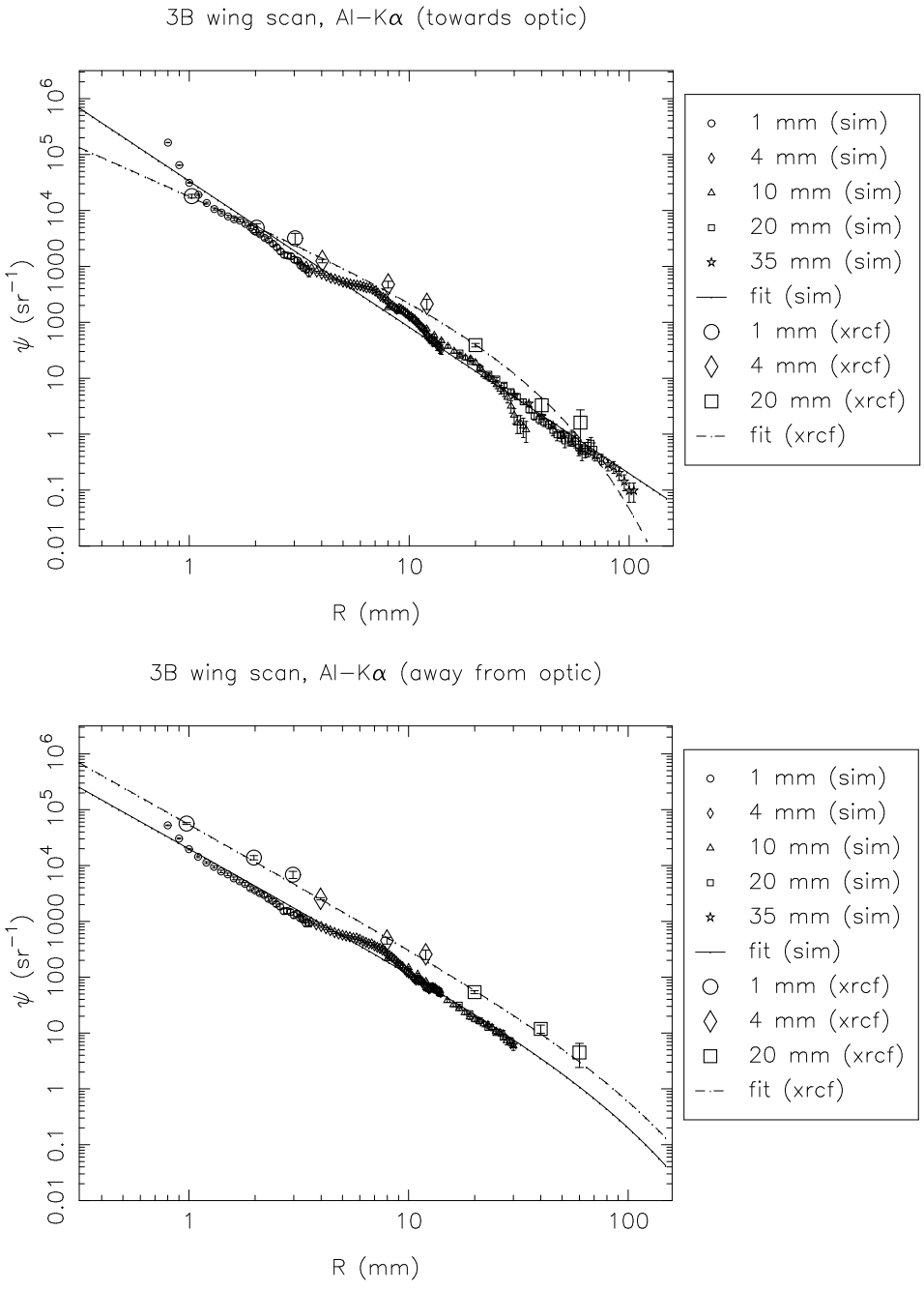

Figure 15.11: Shell 3B: Al-Kα surface brightness, towards and away from the optic

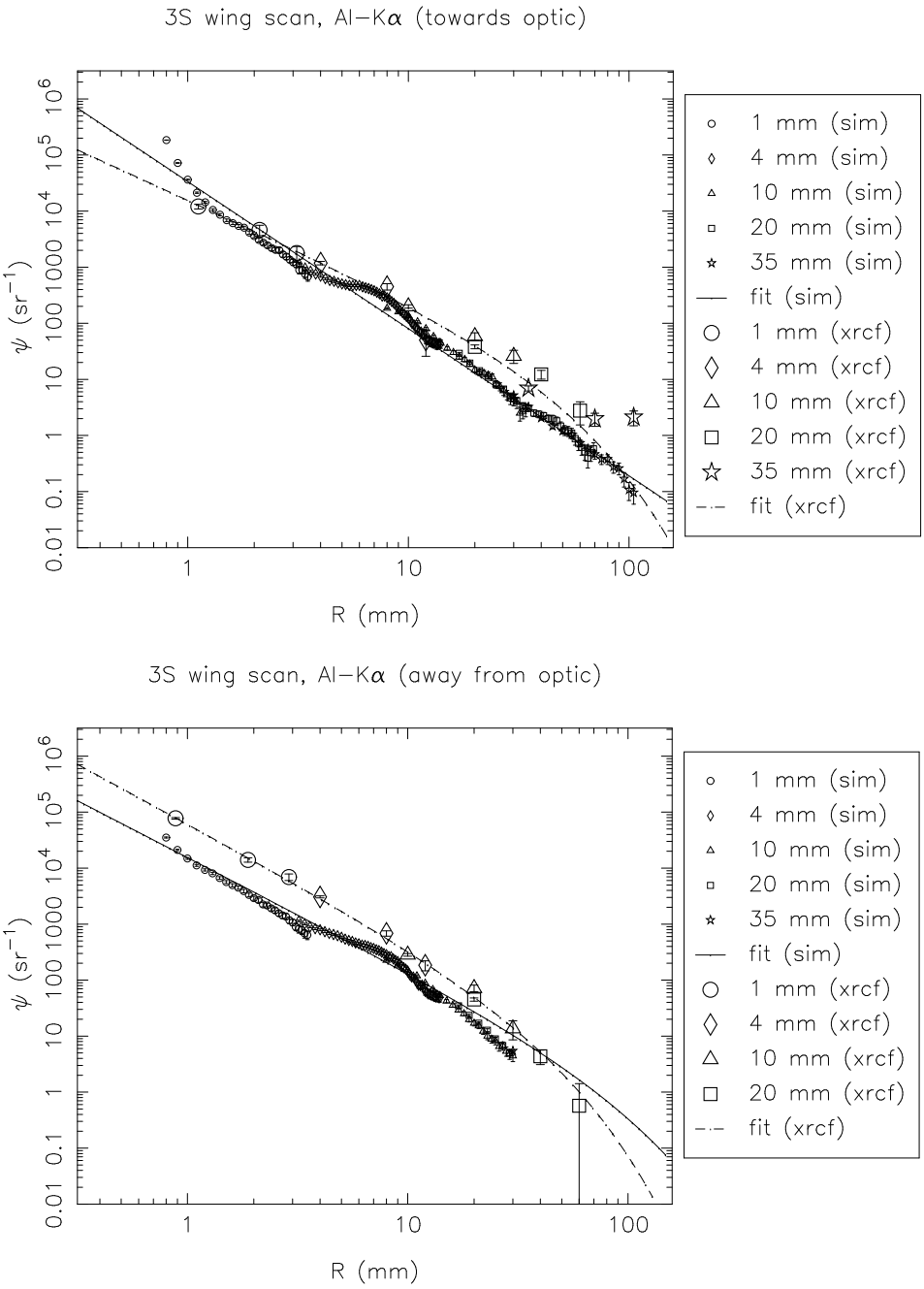

Figure 15.12: Shell 3S: Al-Kα surface brightness, towards and away from the optic

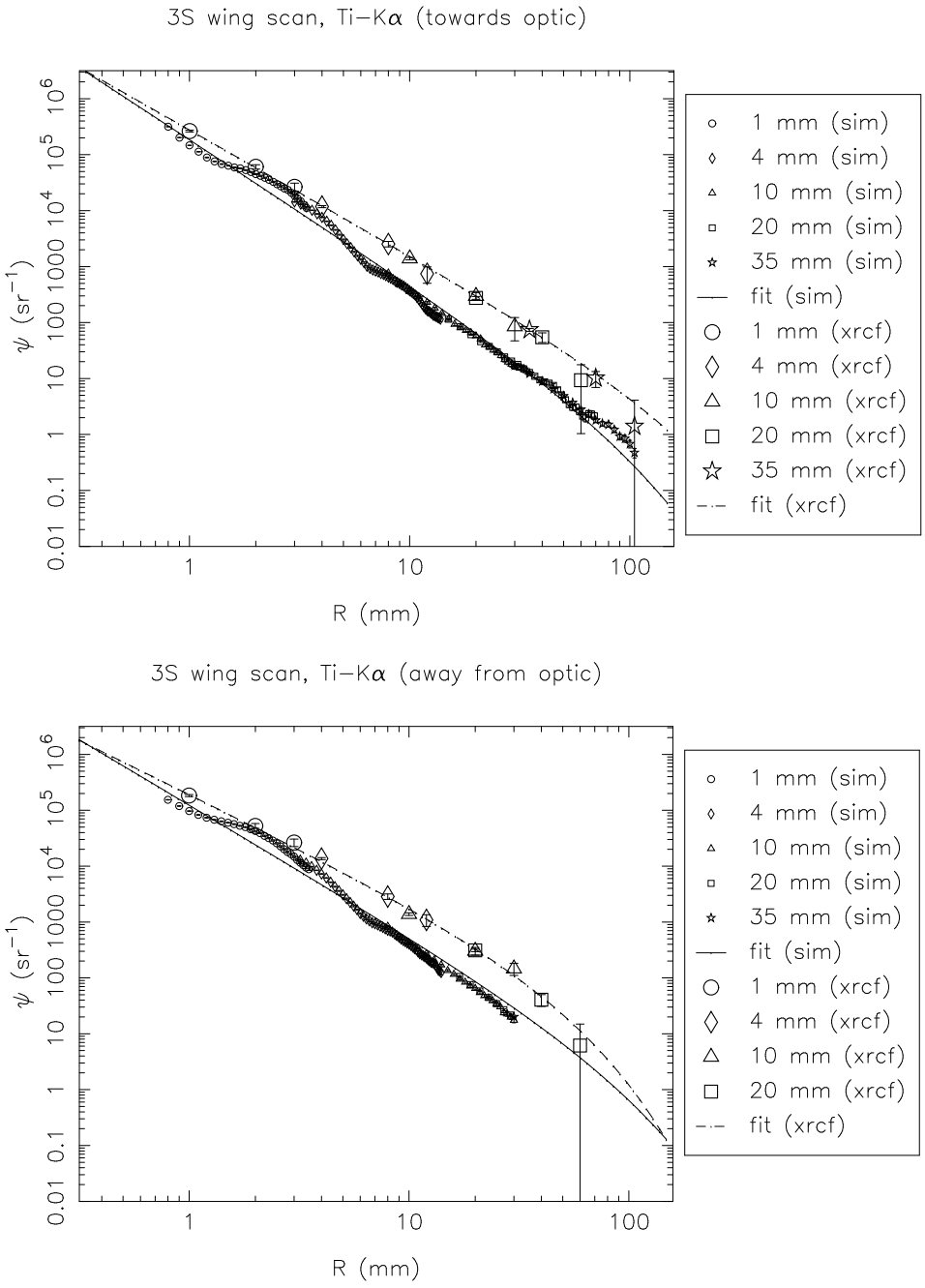

Figure 15.13: Shell 3S: Ti-Kα surface brightness, towards and away from the optic

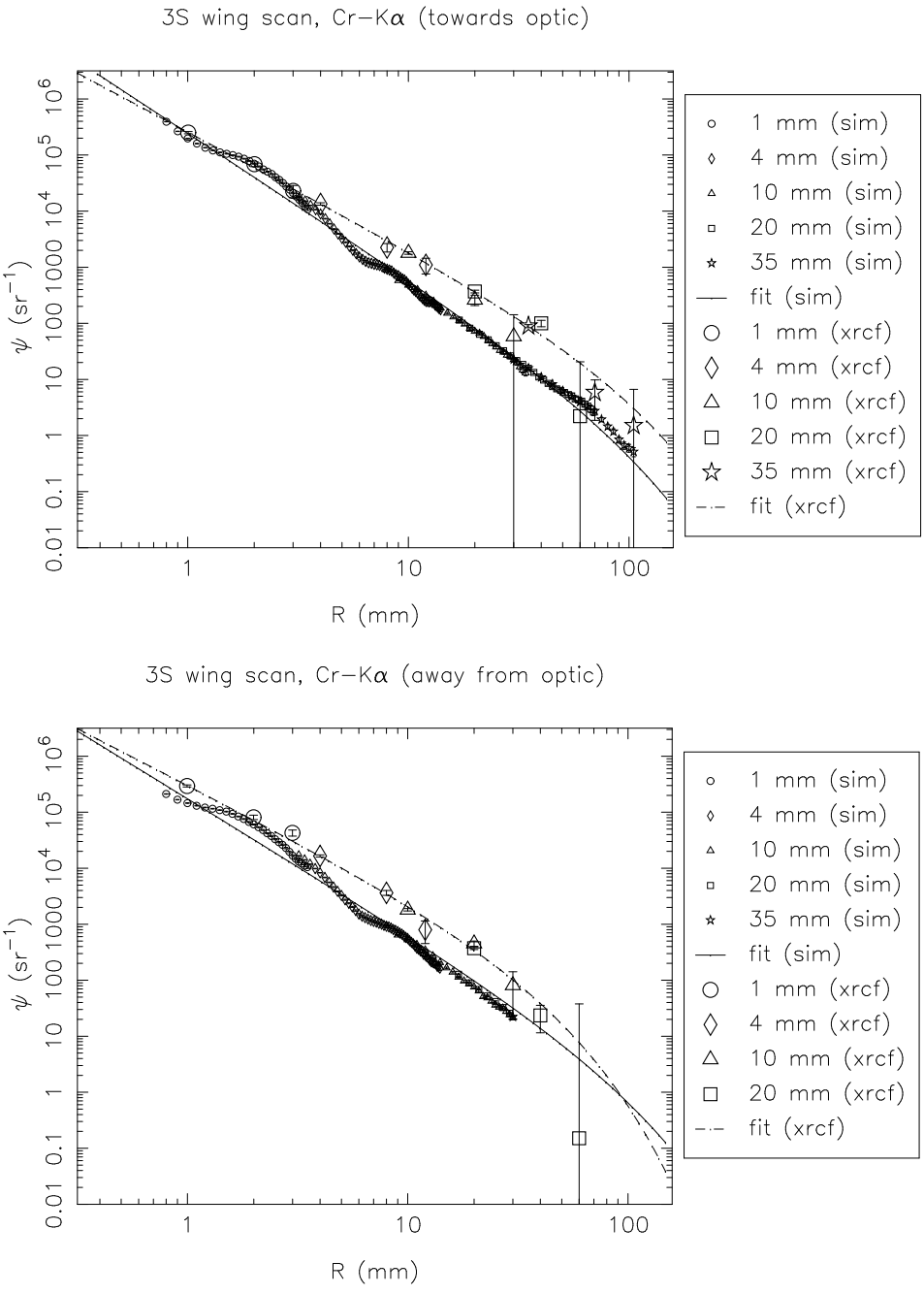

Figure 15.14: Shell 3S: Cr-Kα surface brightness, towards and away from the optic

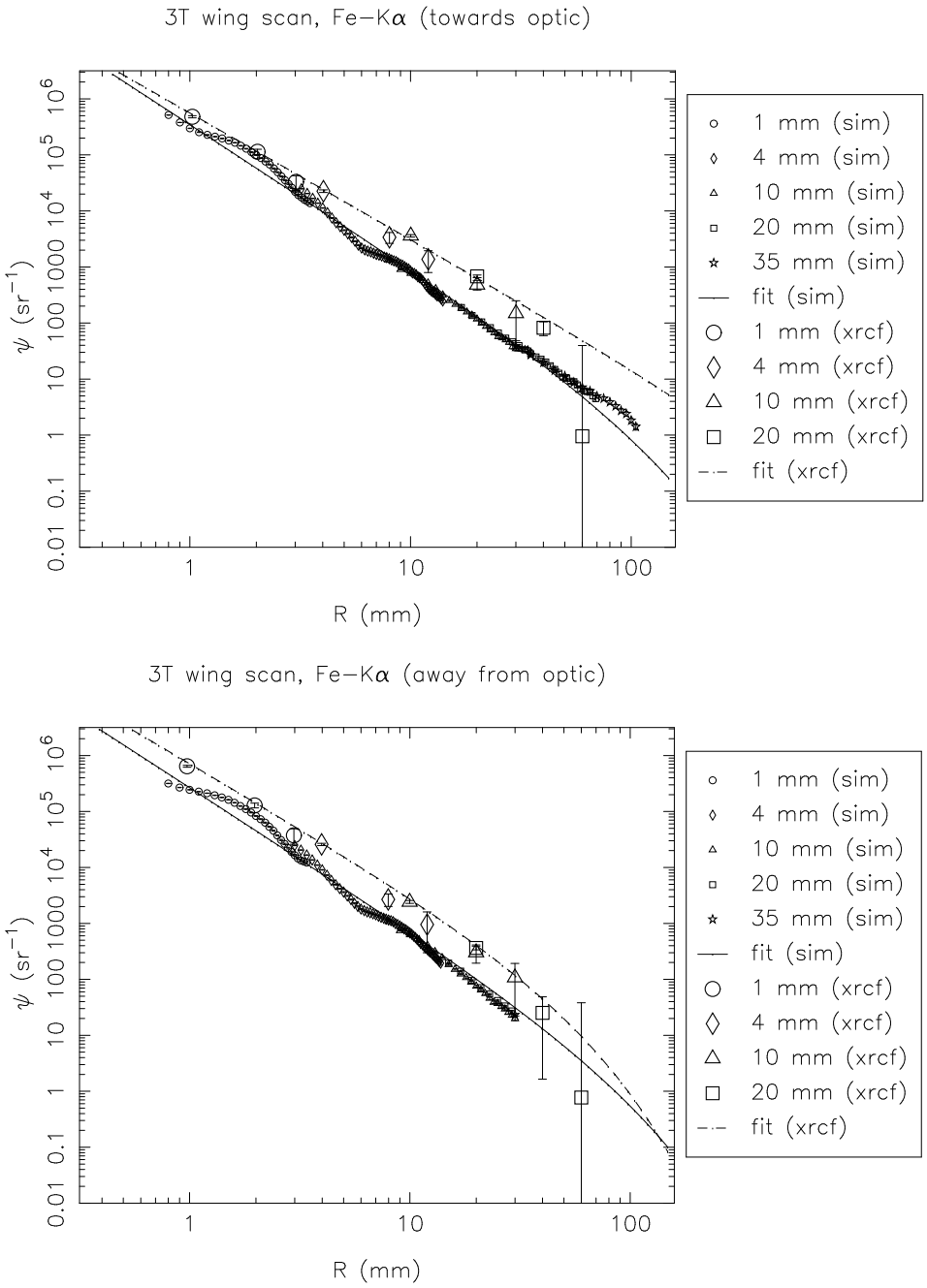

Figure 15.15: Shell 3T: Fe-Kα surface brightness, towards and away from the optic

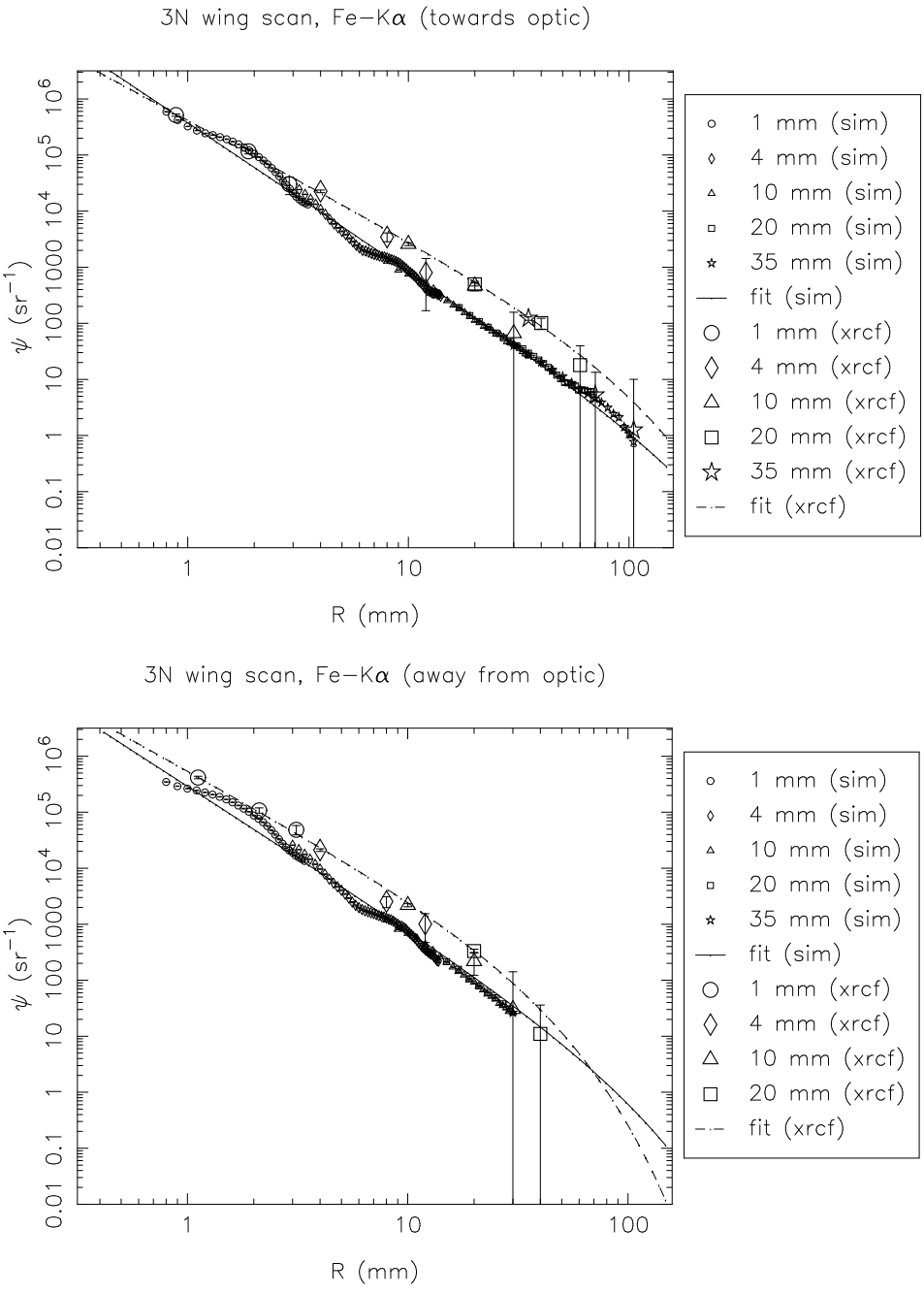

Figure 15.16: Shell 3N: Fe-Kα surface brightness, towards and away from the optic

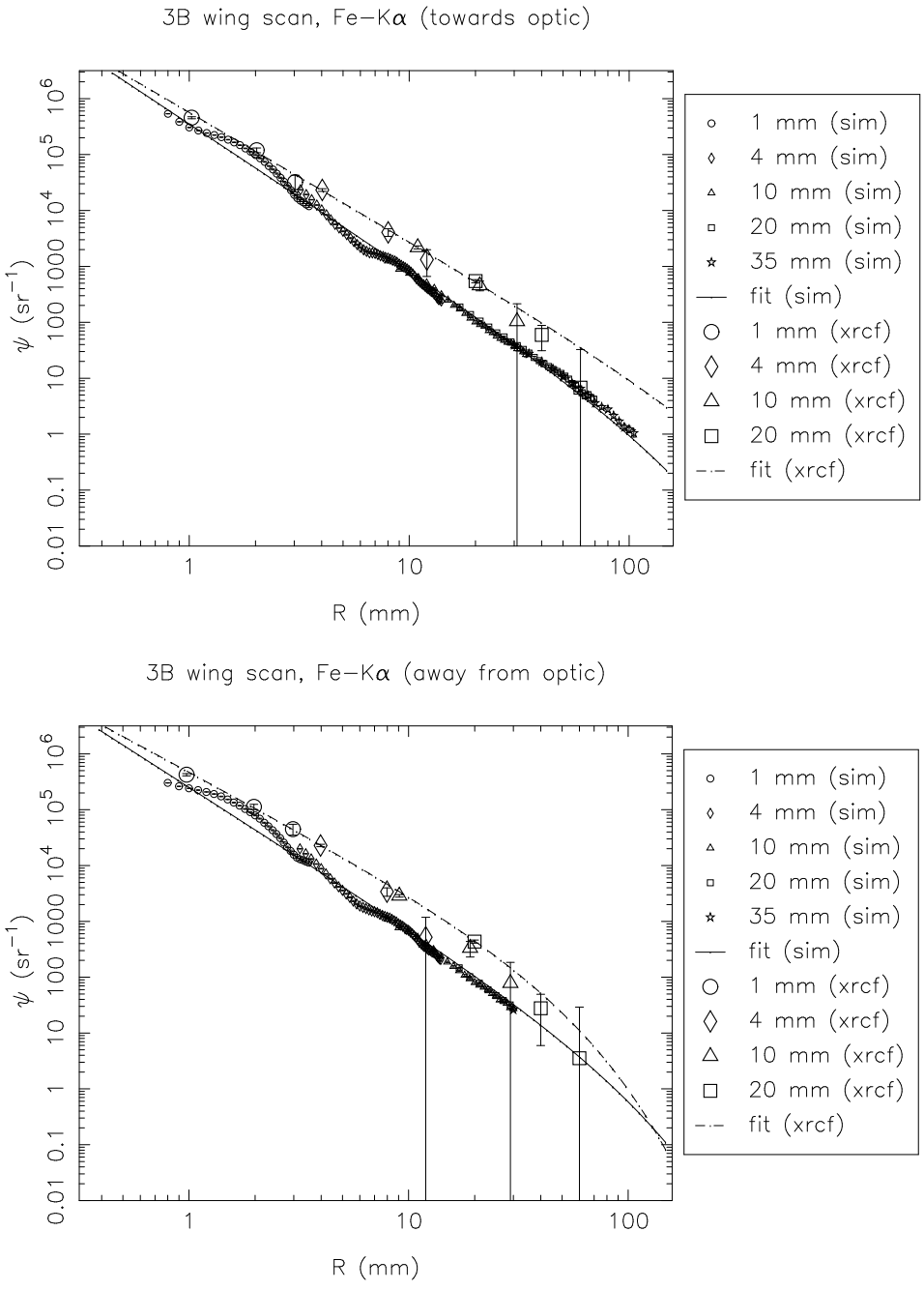

Figure 15.17: Shell 3B: Fe-Kα surface brightness, towards and away from the optic

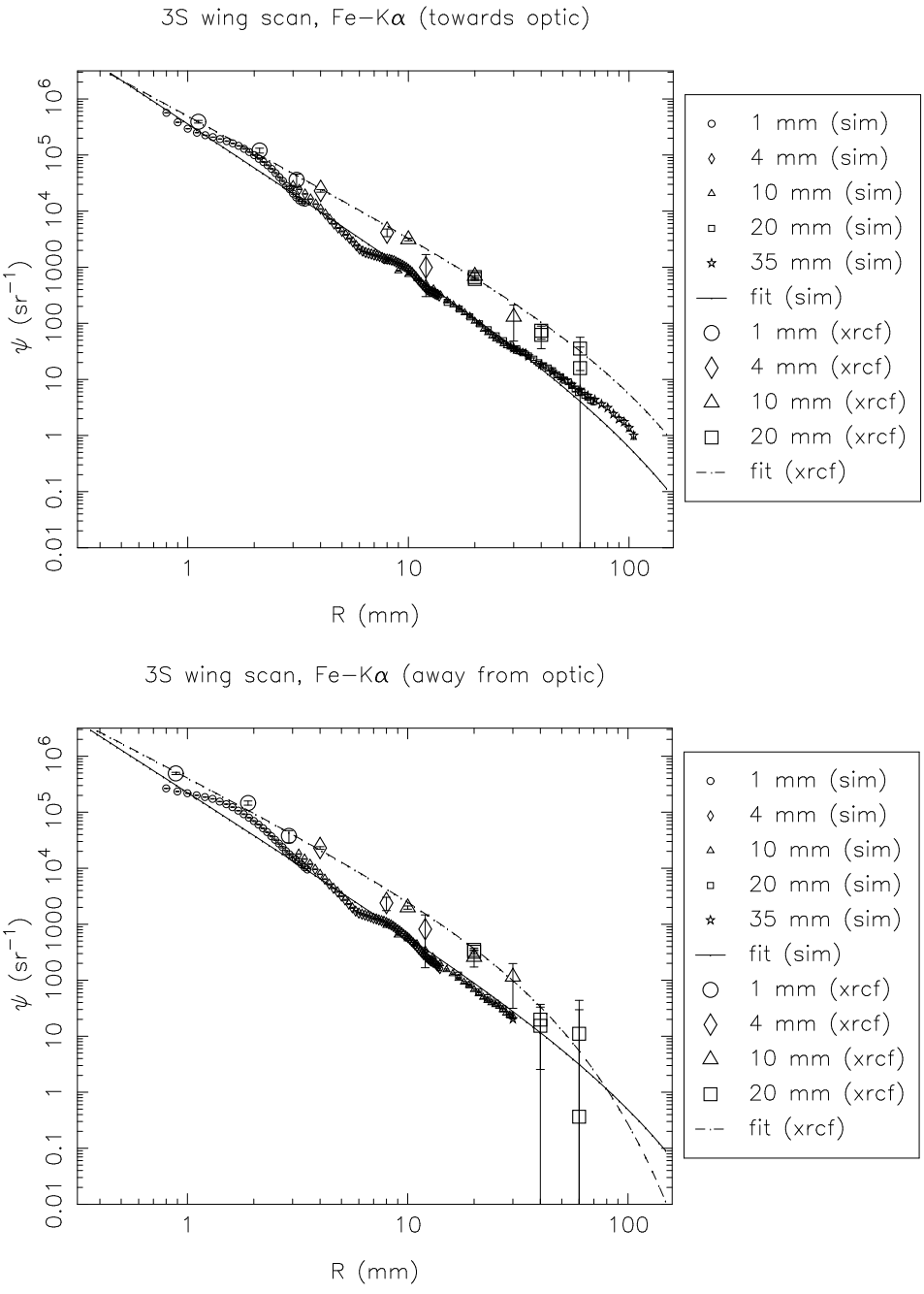

Figure 15.18: Shell 3S: Fe-Kα surface brightness, towards and away from the optic

15.2.3 Shell 4 scans

Table 15.5: Surface brightness fits and fractional excess effective area beyond the 35 mm pinhole. (Raytrace simulations, Shell 4)

Type	Quad	Line	Dir	a	b	c	fractional extra area
sim	4T	Al	in	45522.100	2.862	10000.000	0.000143
sim	4T	Al	out	29538.700	2.500	10000.000	0.000535
sim	4N	Al	in	133732.000	3.433	10000.000	0.000034
sim	4N	Al	out	72861.700	2.880	10000.000	0.000209
sim	4B	Al	in	155290.000	3.686	10000.000	0.000014
sim	4B	Al	out	54287.800	2.719	10000.000	0.000333
sim	4S	Al	in	48438.200	2.912	10000.000	0.000120
sim	4S	Al	out	23695.800	2.435	10000.000	0.000601
sim	4S	Ti	in	207308.000	2.531	278.904	0.001804
sim	4S	Ti	out	148785.000	2.320	85.397	0.001574
sim	4S	Cr	in	271072.000	2.517	597.682	0.003174
sim	4S	Cr	out	200191.000	2.321	70.615	0.001770
sim	4T	Fe	in	309523.000	2.447	600.865	0.005007
sim	4T	Fe	out	254766.000	2.354	70.000	0.001953
sim	4N	Fe	in	420038.000	2.549	8658.530	0.005870
sim	4N	Fe	out	330389.000	2.390	70.000	0.002183
sim	4B	Fe	in	457006.000	2.622	10000.000	0.004478
sim	4B	Fe	out	284517.000	2.365	70.000	0.002078
sim	4S	Fe	in	330882.000	2.487	5767.630	0.006168
sim	4S	Fe	out	222297.000	2.317	70.000	0.001980
sim	4S	Cu	in	489937.000	2.355	10000.000	0.018923
sim	4S	Cu	out	316625.000	2.401	95.931	0.002631

Table 15.6: Surface brightness fits and fractional excess effective area beyond the 35 mm pinhole. (XRCF data, Shell 4)

Type	Quad	Line	Dir	a	b	c	fractional extra area
xrcf	4T	Al	in	113177.000	2.656	10000.000	0.000940
xrcf	4T	Al	out	90027.300	2.756	10000.000	0.000462
xrcf	4N	Al	in	64983.900	2.475	6510.170	0.001299
xrcf	4N	Al	out	67406.900	2.523	10000.000	0.001084
xrcf	4B	Al	in	163766.000	2.881	10000.000	0.000469
xrcf	4B	Al	out	88631.200	2.352	89.746	0.000857
xrcf	4S	Al	in	37857.300	2.152	77.512	0.000741
xrcf	4S	Al	out	106539.000	2.529	10000.000	0.001662
xrcf	4S	Ti	in	281656.000	2.156	54.267	0.003672
xrcf	4S	Ti	out	222767.000	2.077	91.891	0.007020
xrcf	4S	Cr	in	311700.000	2.121	57.218	0.005000
xrcf	4S	Cr	out	323288.000	2.089	47.867	0.004719
xrcf	4T	Fe	in	575581.000	2.220	85.123	0.009246
xrcf	4T	Fe	out	576353.000	2.161	33.536	0.003687
xrcf	4N	Fe	in	462355.000	2.123	51.746	0.006503
xrcf	4N	Fe	out	504010.000	2.151	47.334	0.005633
xrcf	4B	Fe	in	593296.000	2.317	184.370	0.010897
xrcf	4B	Fe	out	549030.000	2.131	31.303	0.003510
xrcf	4S	Fe	in	476664.000	2.171	46.147	0.004748
xrcf	4S	Fe	out	406663.000	1.985	19.077	0.001580
xrcf	4S	Cu	in	842582.000	1.885	42.887	0.024146
xrcf	4S	Cu	out	1173790.000	2.335	48.786	0.006481

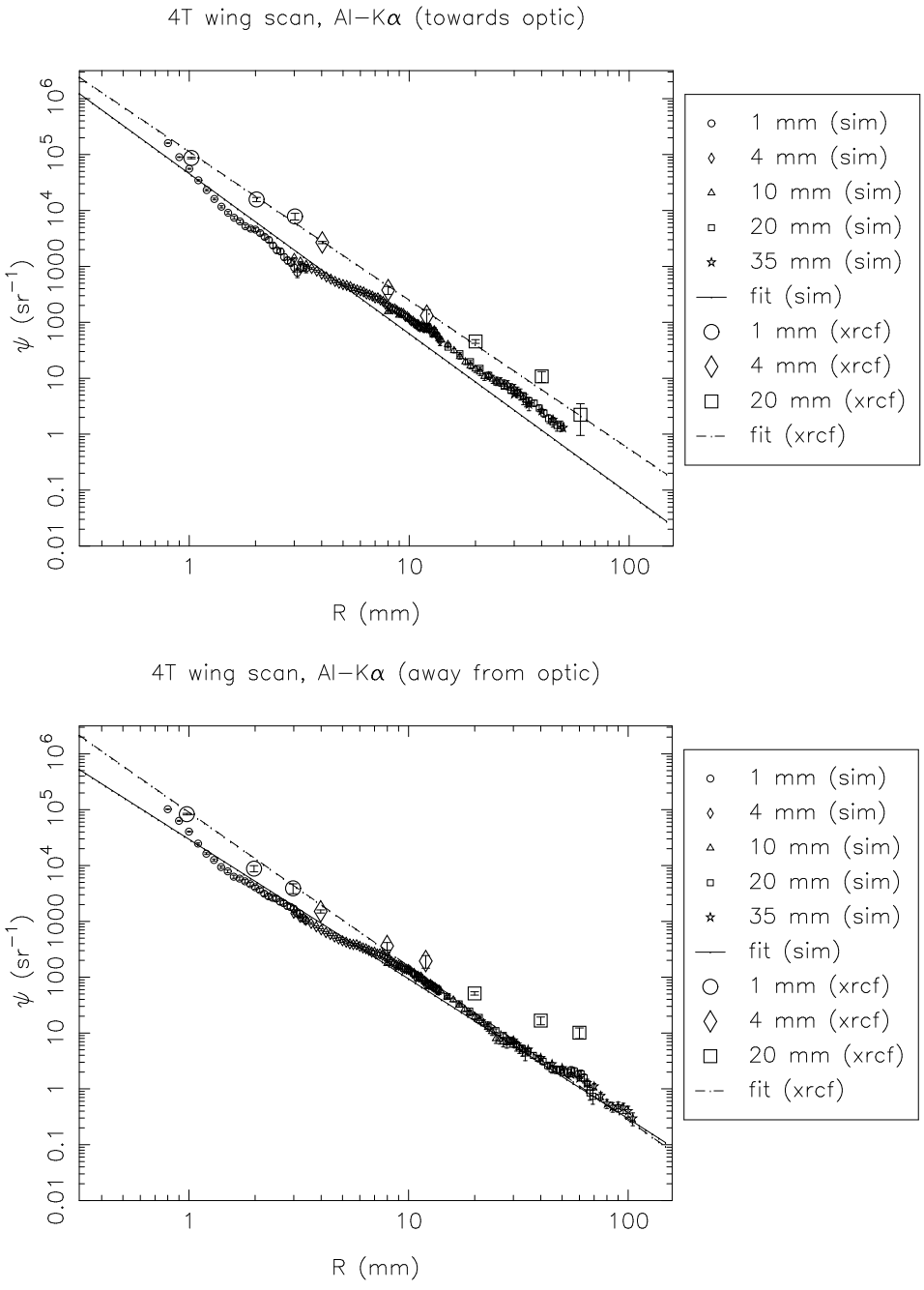

Figure 15.19: Shell 4T: Al-Kα surface brightness, towards and away from the optic

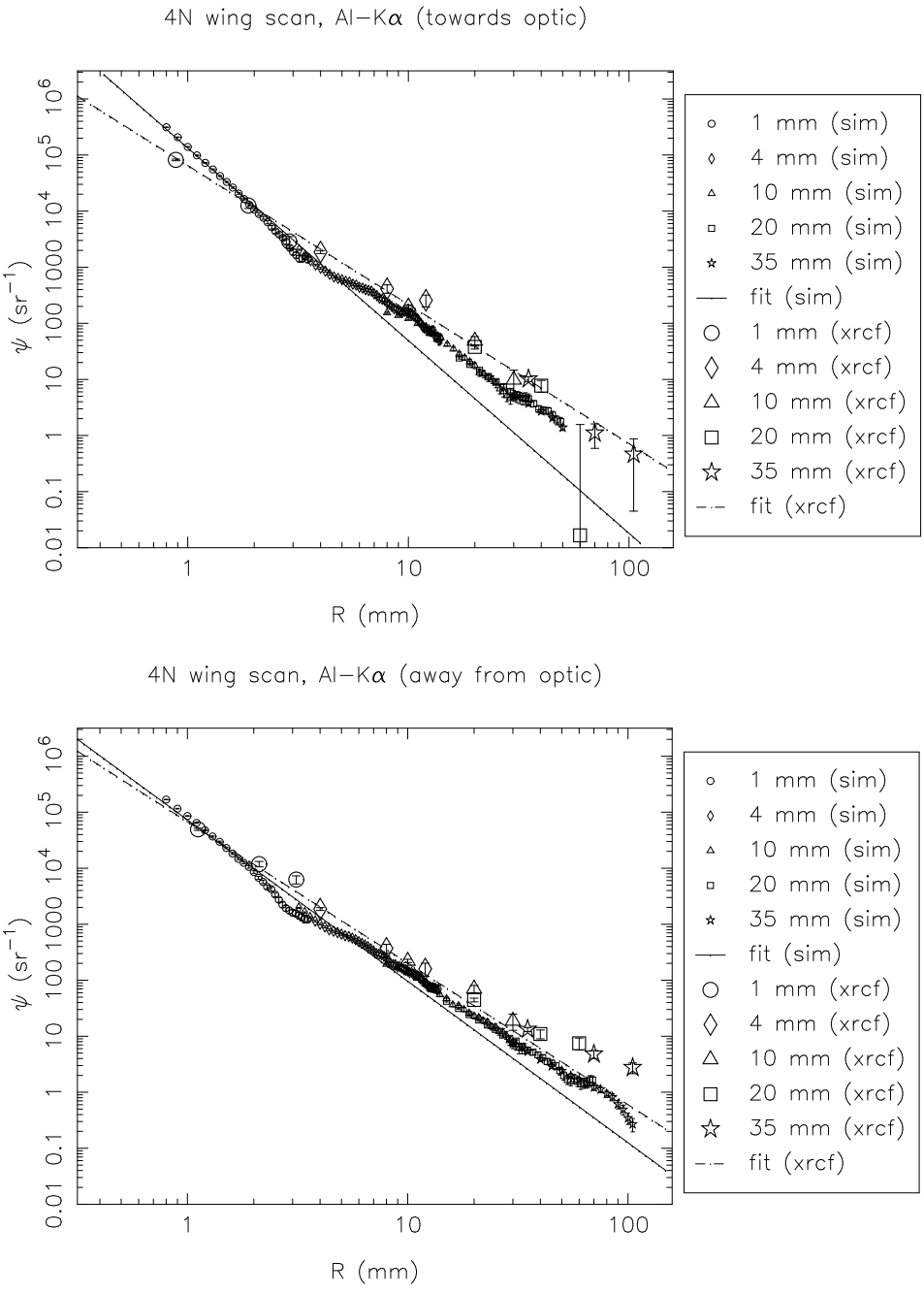

Figure 15.20: Shell 4N: Al-Kα surface brightness, towards and away from the optic

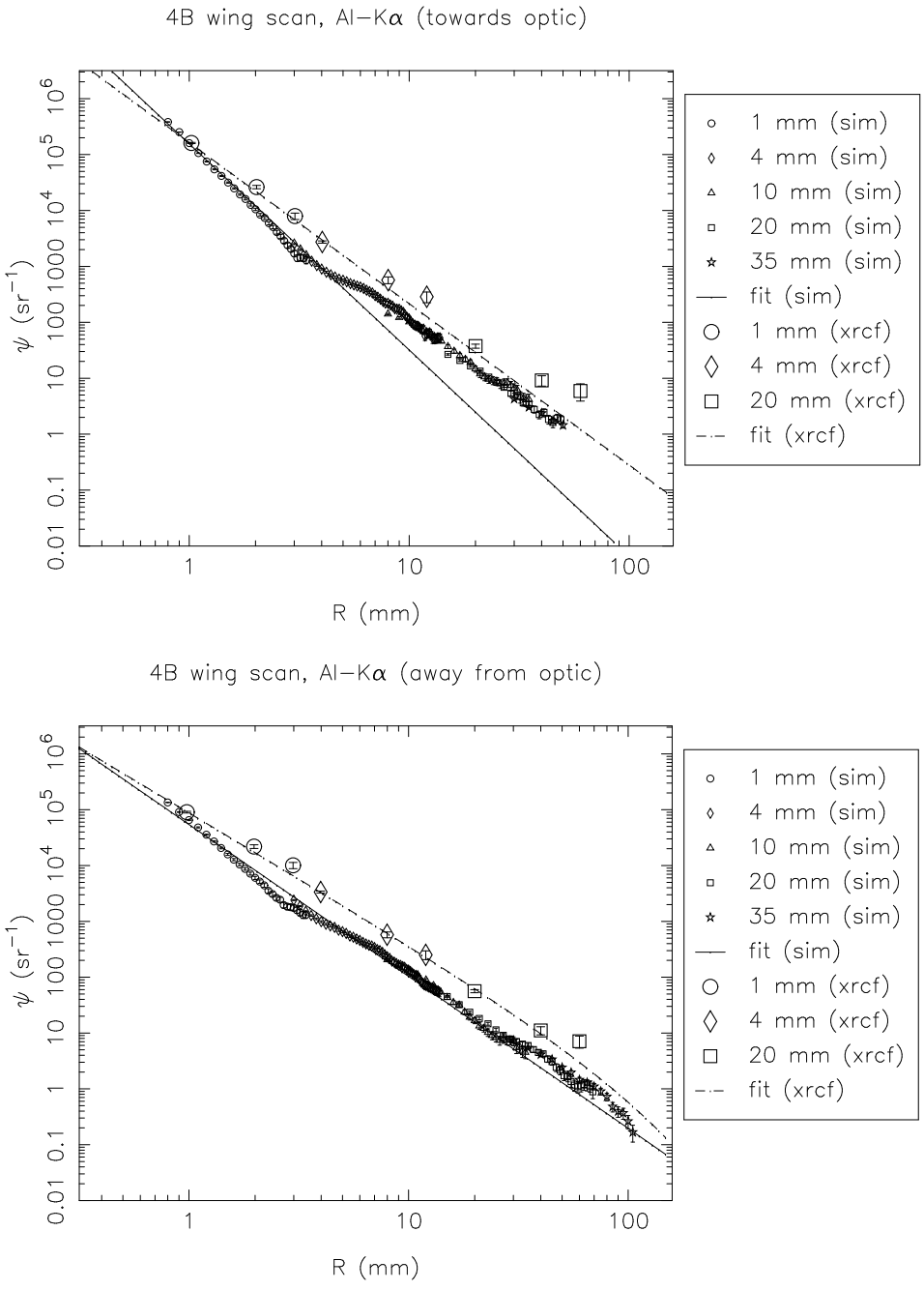

Figure 15.21: Shell 4B: Al-Kα surface brightness, towards and away from the optic

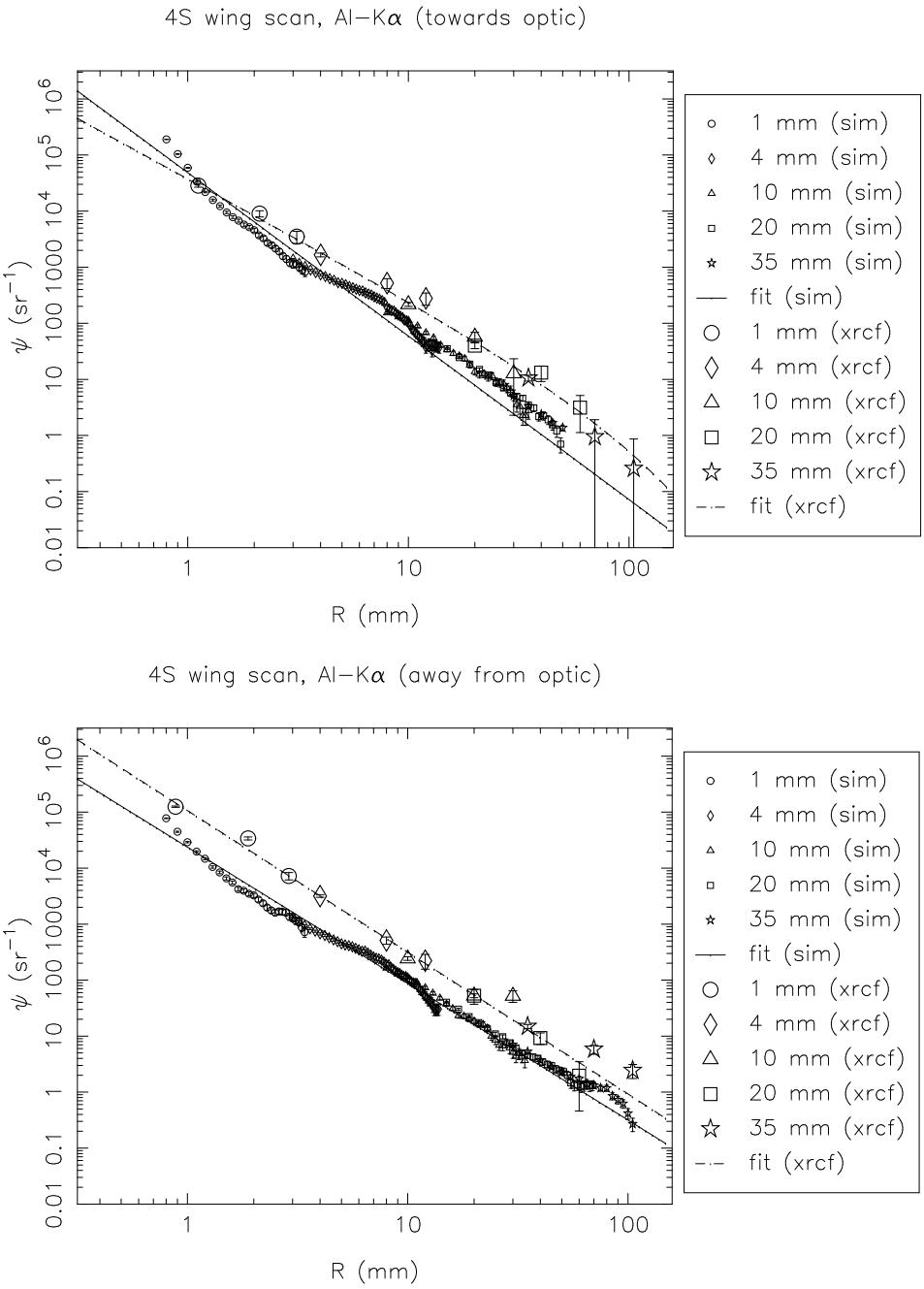

Figure 15.22: Shell 4S: Al-Kα surface brightness, towards and away from the optic

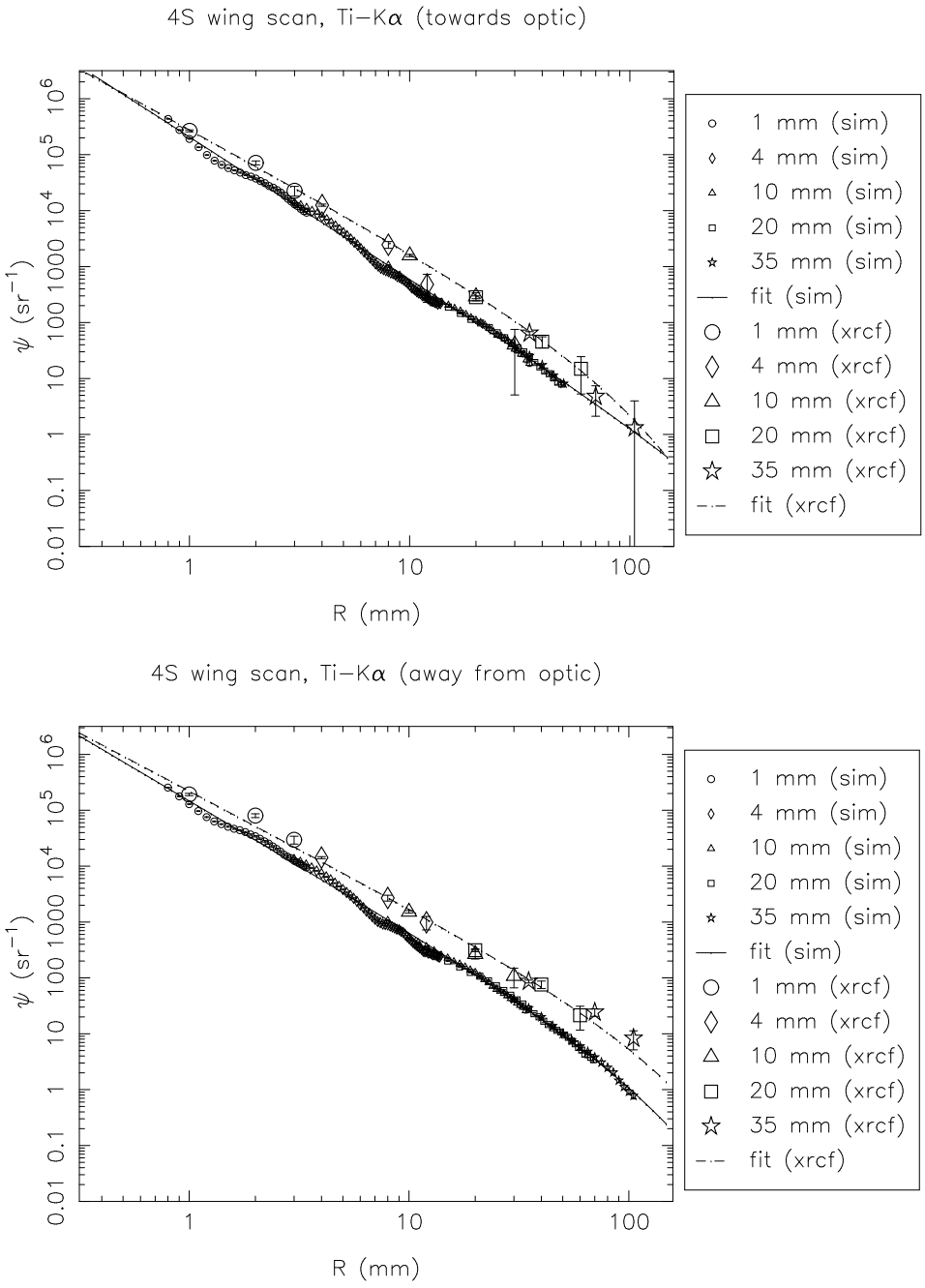

Figure 15.23: Shell 4S: Ti-Kα surface brightness, towards and away from the optic

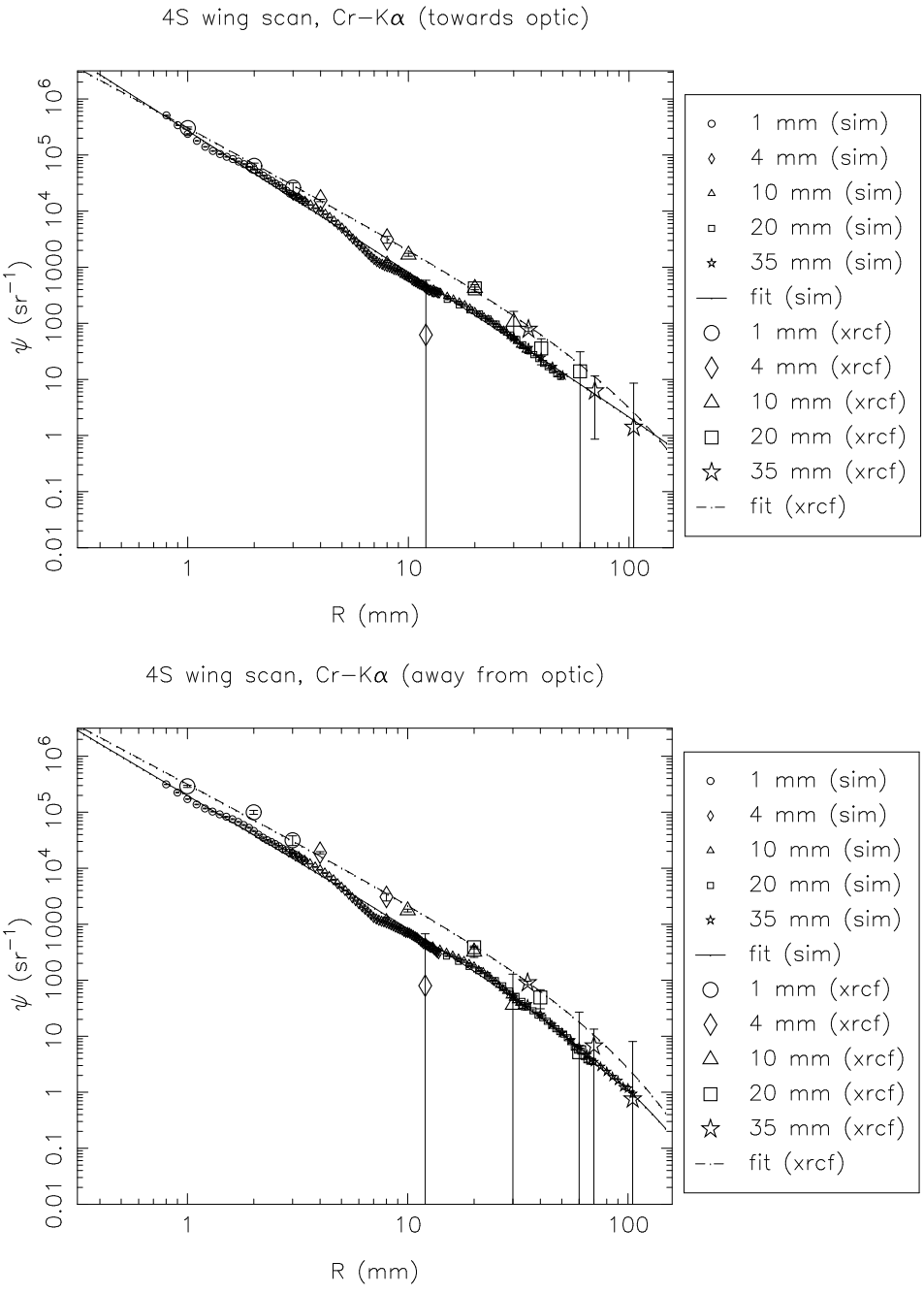

Figure 15.24: Shell 4S: Cr-Kα surface brightness, towards and away from the optic

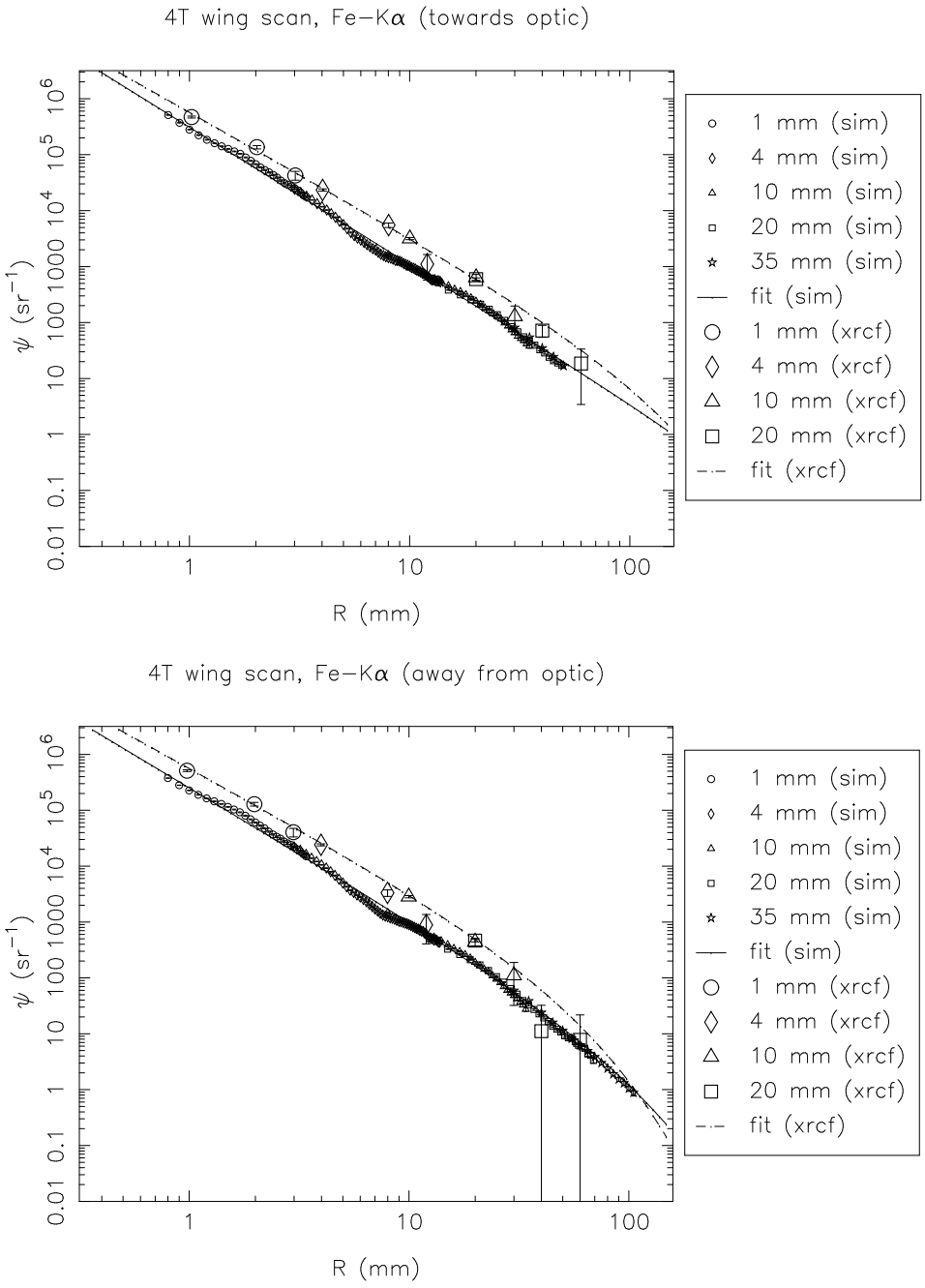

Figure 15.25: Shell 4T: Fe-Kα surface brightness, towards and away from the optic

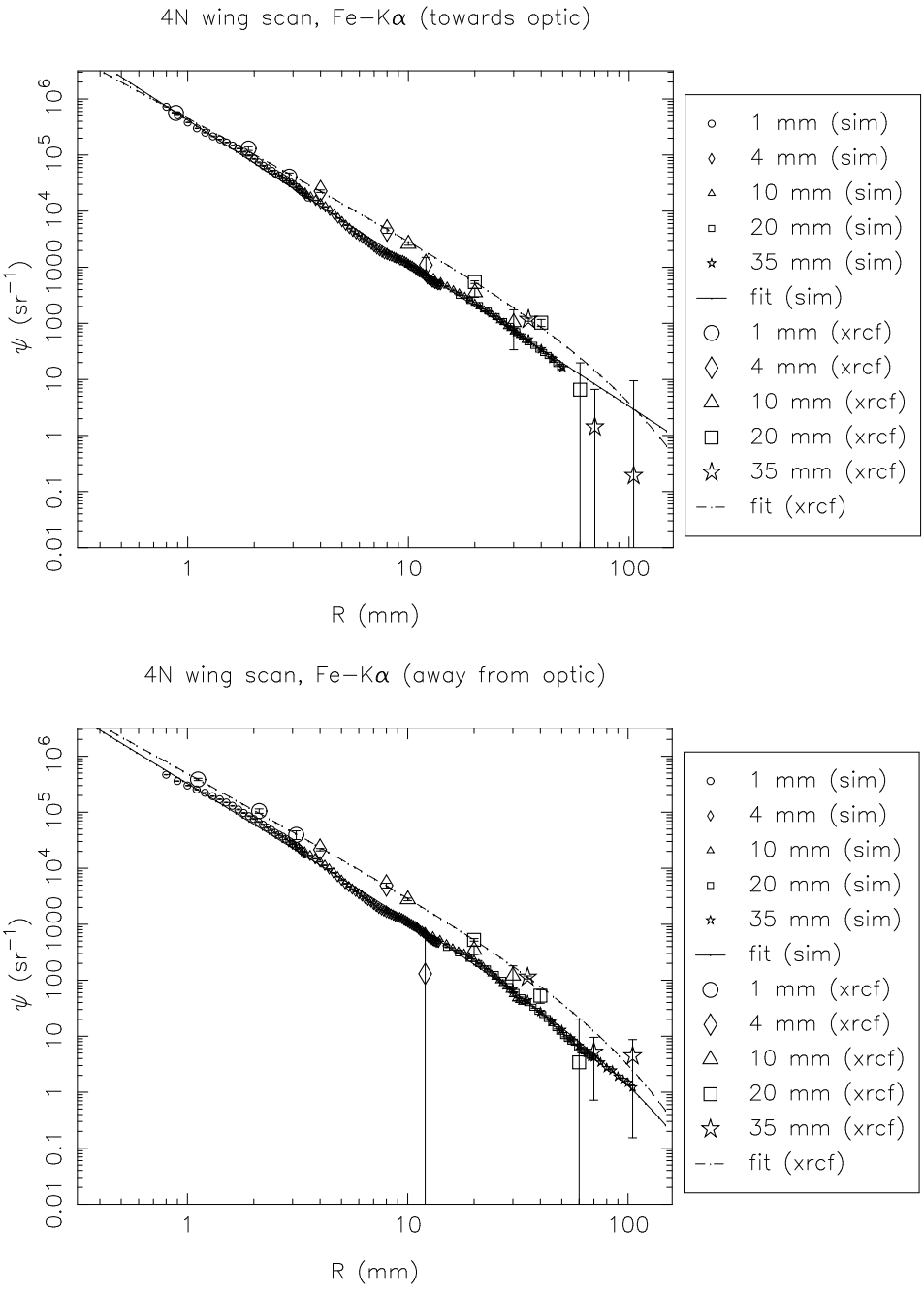

Figure 15.26: Shell 4N: Fe-Kα surface brightness, towards and away from the optic

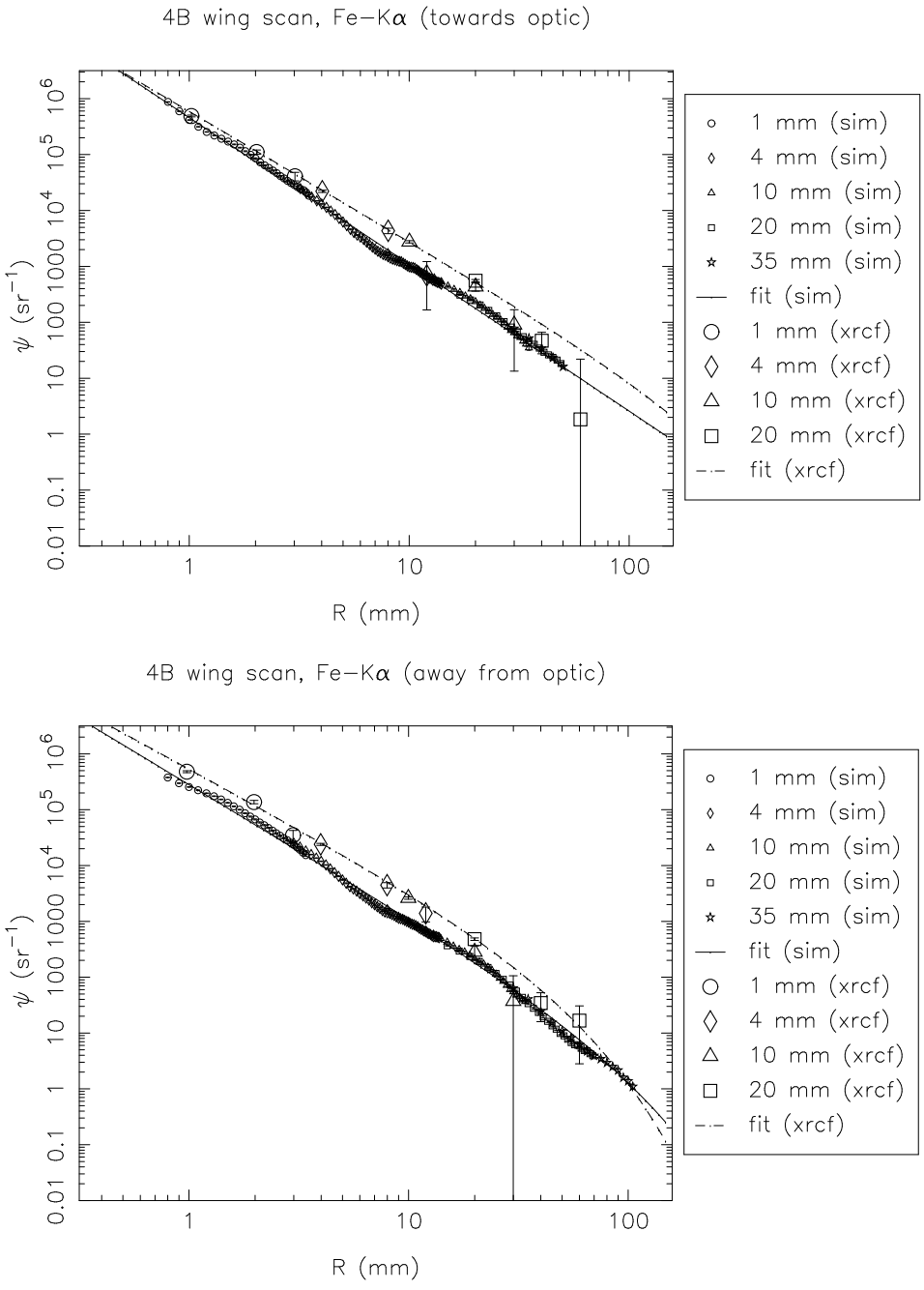

Figure 15.27: Shell 4B: Fe-Kα surface brightness, towards and away from the optic

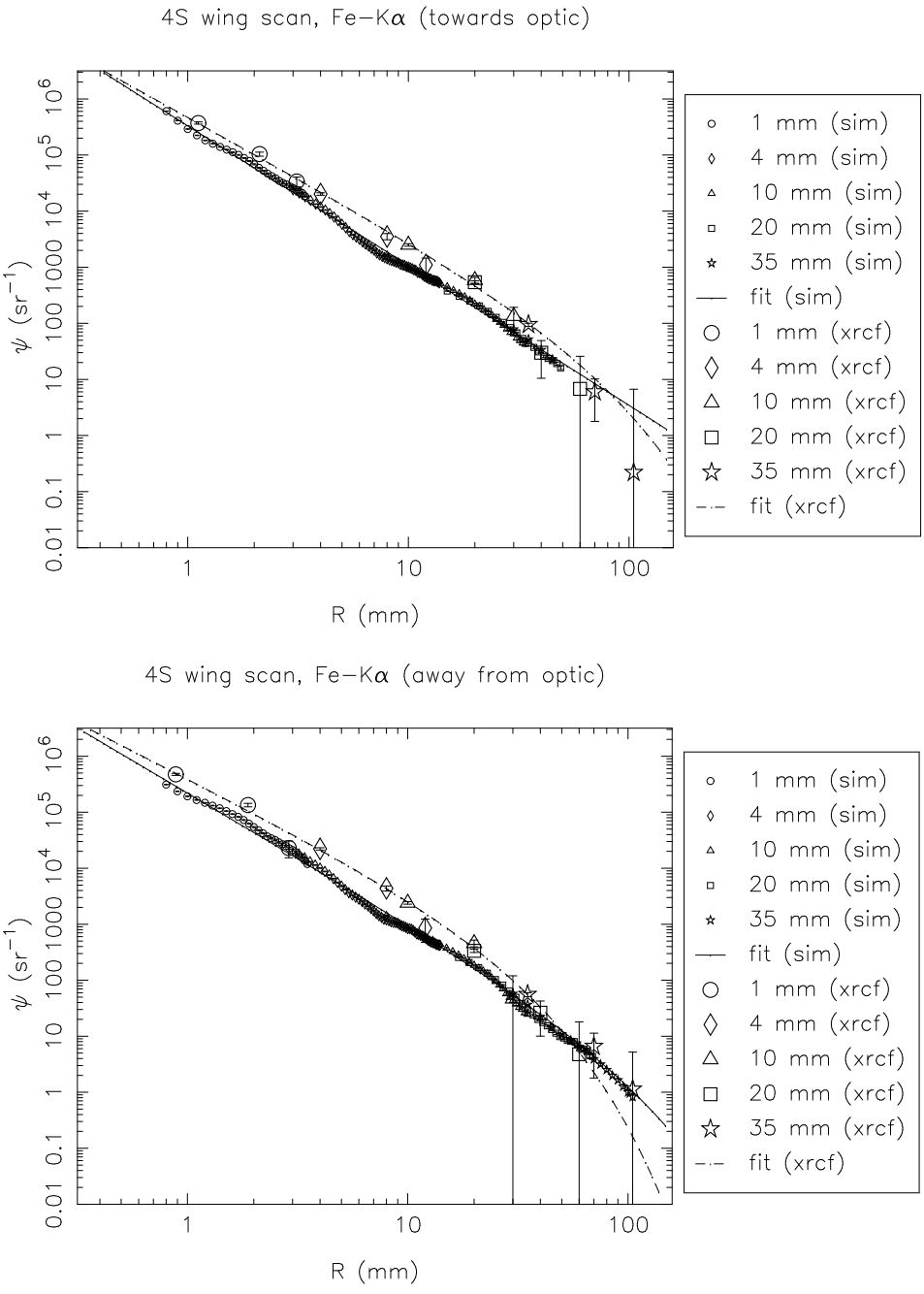

Figure 15.28: Shell 4S: Fe-Kα surface brightness, towards and away from the optic

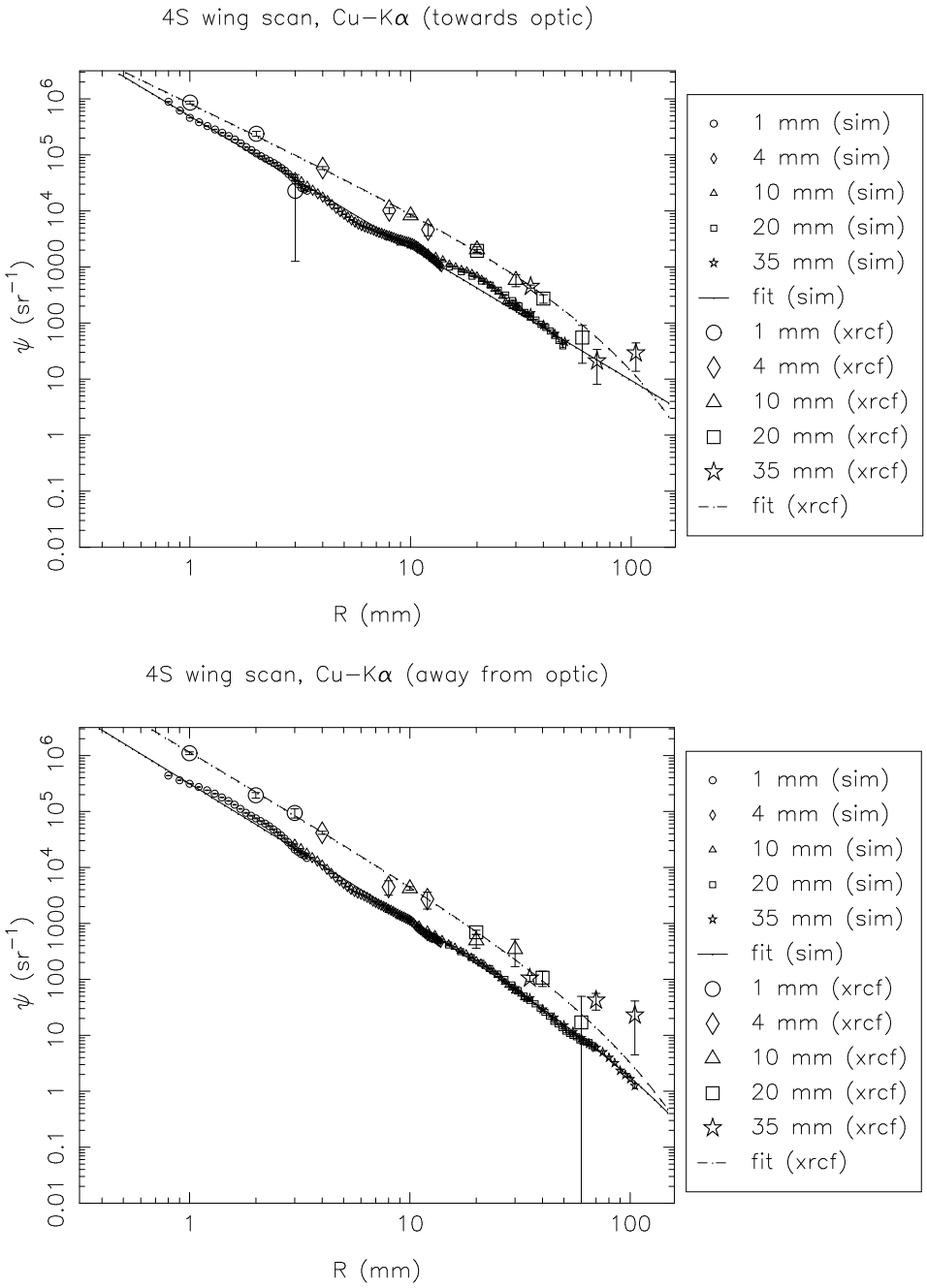

Figure 15.29: Shell 4S: Cu-Kα surface brightness, towards and away from the optic

15.2.4 Shell 6 scans

Table 15.7: Surface brightness fits and fractional excess effective area beyond the 35 mm pinhole. (Raytrace simulations, Shell 6)

Type	Quad	Line	Dir	a	b	c	fractional extra area
sim	6B	C	in	25912.900	3.142	70.000	0.000008
sim	6B	C	out	30915.300	2.895	70.000	0.000026
sim	6T	Al	in	121092.000	3.146	10000.000	0.000105
sim	6T	Al	out	116395.000	3.095	10000.000	0.000127
sim	6N	Al	in	101486.600	3.262	10000.000	0.000053
sim	6N	Al	out	120531.000	3.058	10000.000	0.000155
sim	6B	Al	in	122030.000	3.475	10000.000	0.000026
sim	6B	Al	out	109760.000	3.109	10000.000	0.000112
sim	6S	Al	in	134708.000	3.231	10000.000	0.000081
sim	6S	Al	out	96170.800	3.019	10000.000	0.000147
sim	6S	Ti	in	199568.000	2.518	70.000	0.000779
sim	6S	Ti	out	193288.000	2.421	70.000	0.001121
sim	6S	Cr	in	246680.000	2.482	70.000	0.001115
sim	6S	Cr	out	232063.000	2.388	70.000	0.001543
sim	6T	Fe	in	292414.000	2.415	70.000	0.001741
sim	6T	Fe	out	284040.000	2.373	70.000	0.002010
sim	6N	Fe	in	298852.000	2.414	70.000	0.001789
sim	6N	Fe	out	305030.000	2.354	70.000	0.002333
sim	6B	Fe	in	335773.000	2.506	70.000	0.001378
sim	6B	Fe	out	279676.000	2.356	70.000	0.002125
sim	6S	Fe	in	317636.000	2.464	70.000	0.001548
sim	6S	Fe	out	246516.000	2.352	70.000	0.001903
sim	6T	Cu	in	388002.000	2.394	70.000	0.002519
sim	6T	Cu	out	383320.000	2.453	70.000	0.001953
sim	6N	Cu	in	415306.000	2.415	70.000	0.002471
sim	6N	Cu	out	417002.000	2.436	70.000	0.002275
sim	6B	Cu	in	442238.000	2.470	70.000	0.002105
sim	6B	Cu	out	387613.000	2.437	70.000	0.002108
sim	6S	Cu	in	431805.000	2.439	70.000	0.002333
sim	6S	Cu	out	330644.000	2.368	70.000	0.002390

Table 15.8: Surface brightness fits and fractional excess effective area beyond the 35 mm pinhole. (XRCF data, Shell 6)

Type	Quad	Line	Dir	a	b	c	fractional extra area
xrcf	6B	C	in	107596.000	2.926	50.000	0.000058
xrcf	6B	C	out	61652.600	2.939	50.000	0.000031
xrcf	6T	Al	in	76735.100	2.176	12.628	0.000041
xrcf	6T	Al	out	194262.000	3.076	10000.000	0.000230
xrcf	6N	Al	in	103493.200	2.751	10000.000	0.000544
xrcf	6N	Al	out	169376.000	2.860	10000.000	0.000534
xrcf	6B	Al	in	168171.000	2.846	10000.000	0.000566
xrcf	6B	Al	out	103630.200	2.655	10000.000	0.000865
xrcf	6S	Al	in	193325.000	3.605	10000.000	0.000024
xrcf	6S	Al	out	209454.000	2.982	10000.000	0.000378
xrcf	6S	Ti	in	255254.000	2.216	98.125	0.004716
xrcf	6S	Ti	out	222456.000	2.161	76.943	0.004162
xrcf	6S	Cr	in	258517.000	2.108	46.722	0.003380
xrcf	6S	Cr	out	284988.000	2.073	38.094	0.003186
xrcf	6T	Fe	in	286282.000	1.911	35.797	0.005547
xrcf	6T	Fe	in	418386.000	2.104	40.853	0.004595
xrcf	6T	Fe	out	286282.000	1.911	35.797	0.005547
xrcf	6T	Fe	out	418386.000	2.104	40.853	0.004595
xrcf	6N	Fe	in	284232.000	1.840	19.108	0.001944
xrcf	6N	Fe	out	360357.000	2.108	46.673	0.004705
xrcf	6B	Fe	in	421488.000	2.182	55.439	0.005070
xrcf	6B	Fe	out	376848.000	2.039	36.442	0.004500
xrcf	6S	Fe	in	399255.000	2.052	38.782	0.004994
xrcf	6S	Fe	out	309988.000	1.994	36.596	0.004464
xrcf	6T	Cu	in	426542.000	1.872	24.960	0.004861
xrcf	6T	Cu	out	511460.000	1.981	20.652	0.002465
xrcf	6N	Cu	in	478480.000	1.807	14.549	0.001680
xrcf	6N	Cu	out	478914.000	1.917	17.547	0.001933
xrcf	6B	Cu	in	548984.000	2.065	32.972	0.004997
xrcf	6B	Cu	out	478089.000	1.893	19.165	0.002684
xrcf	6S	Cu	in	467525.000	1.887	19.009	0.002630
xrcf	6S	Cu	out	483961.000	1.957	15.265	0.001114

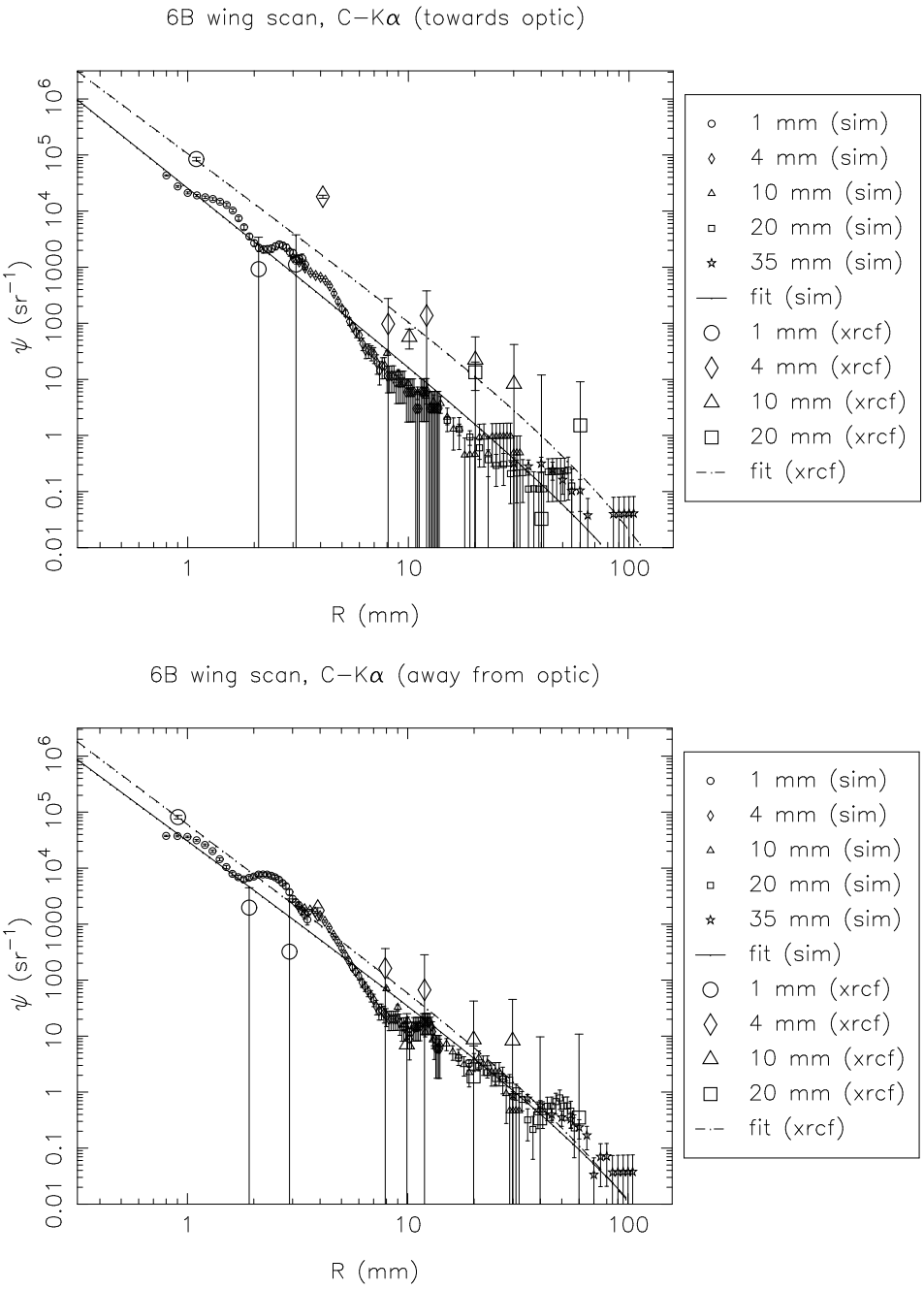

Figure 15.30: Shell 6B: C-Kα surface brightness, towards and away from the optic

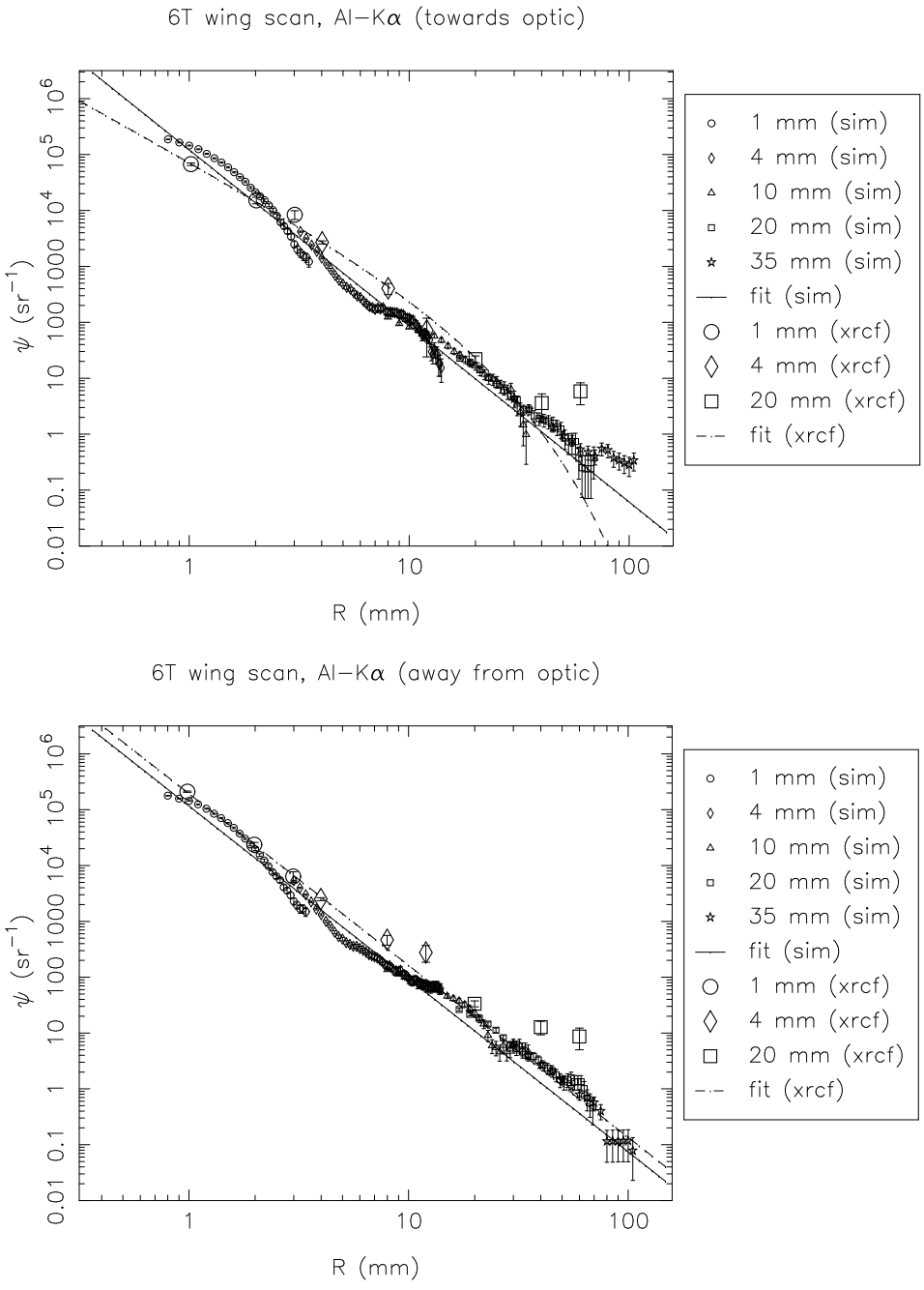

Figure 15.31: Shell 6T: Al-Kα surface brightness, towards and away from the optic

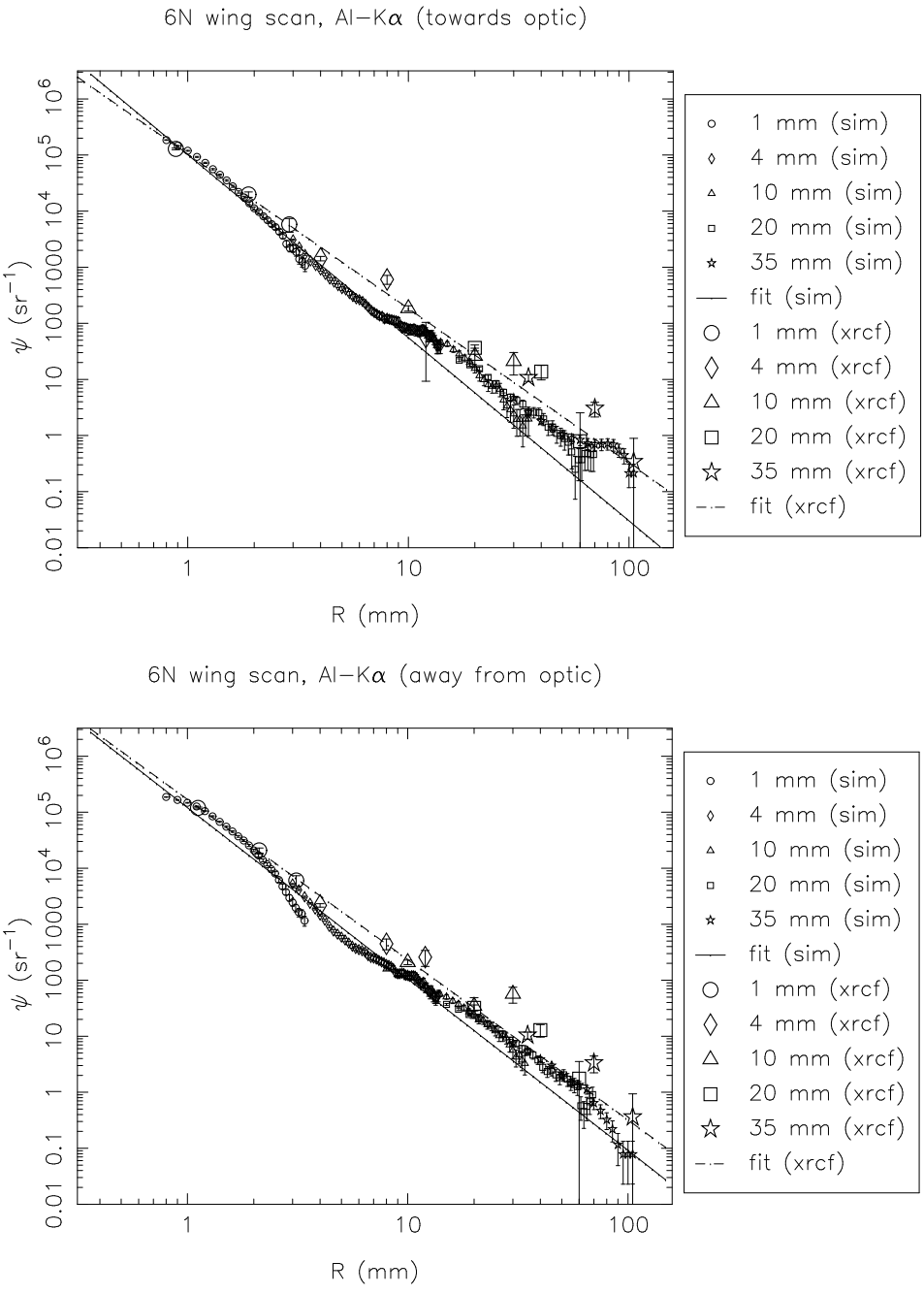

Figure 15.32: Shell 6N: Al-Kα surface brightness, towards and away from the optic

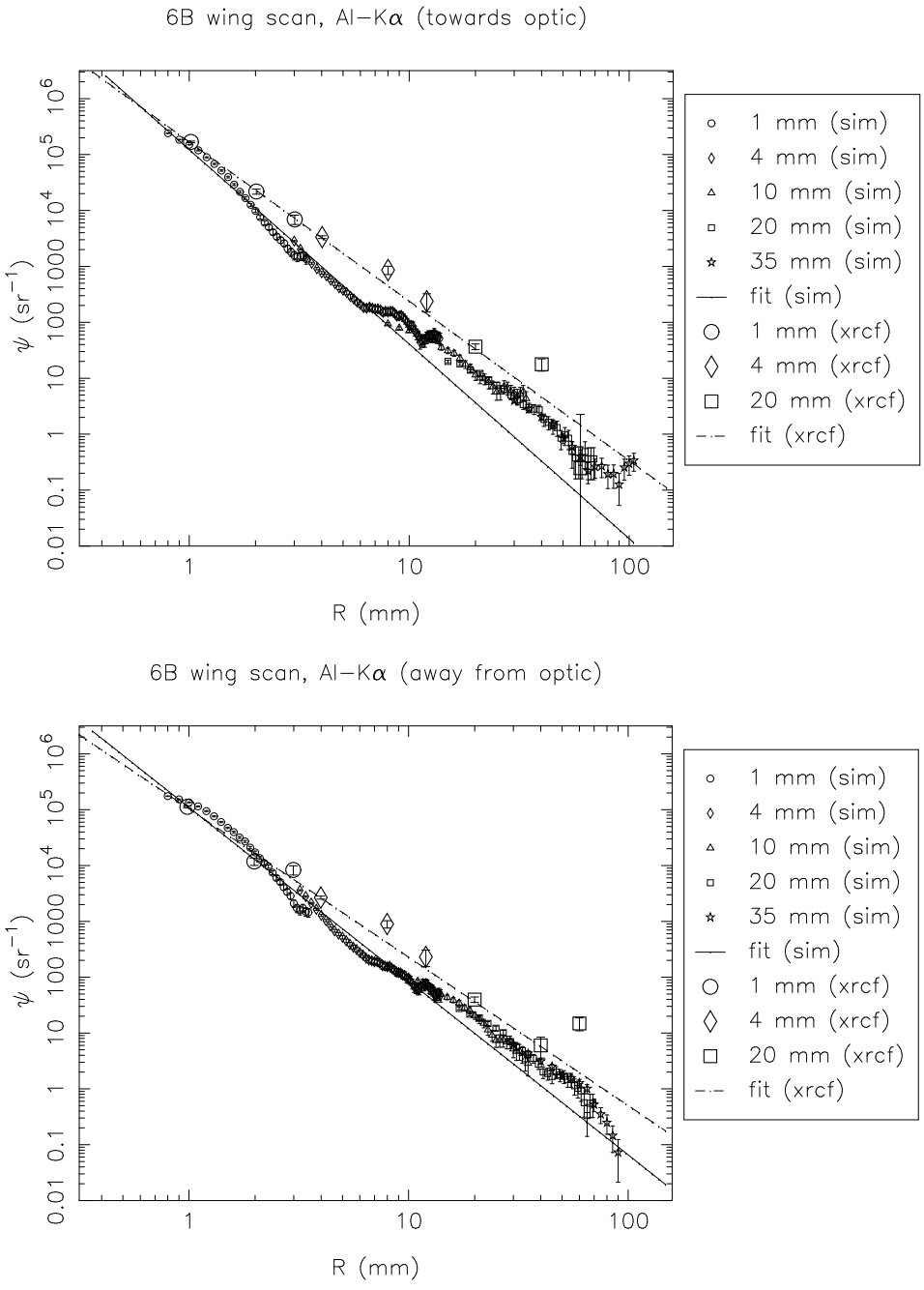

Figure 15.33: Shell 6B: Al-Kα surface brightness, towards and away from the optic

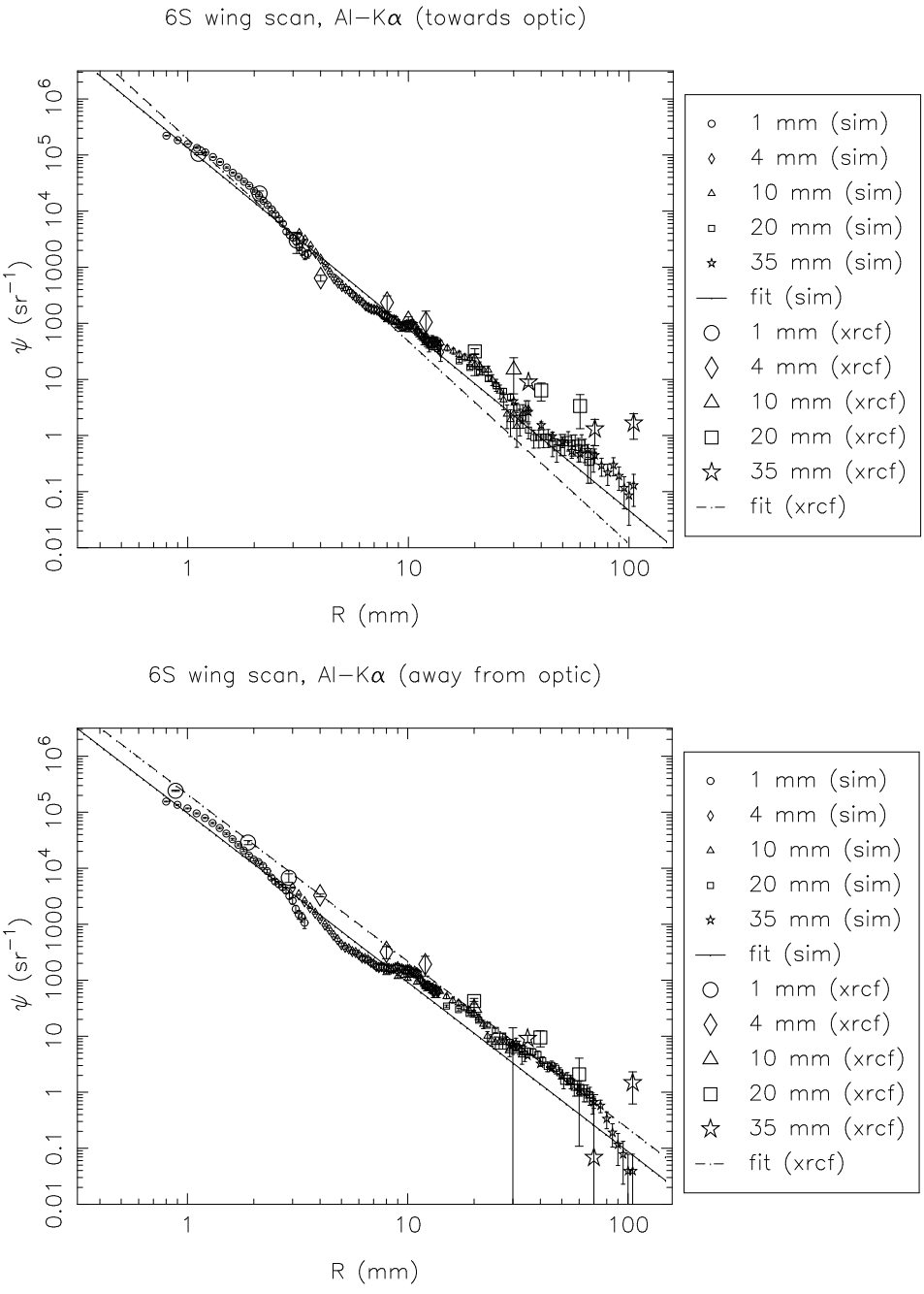

Figure 15.34: Shell 6S: Al-Kα surface brightness, towards and away from the optic

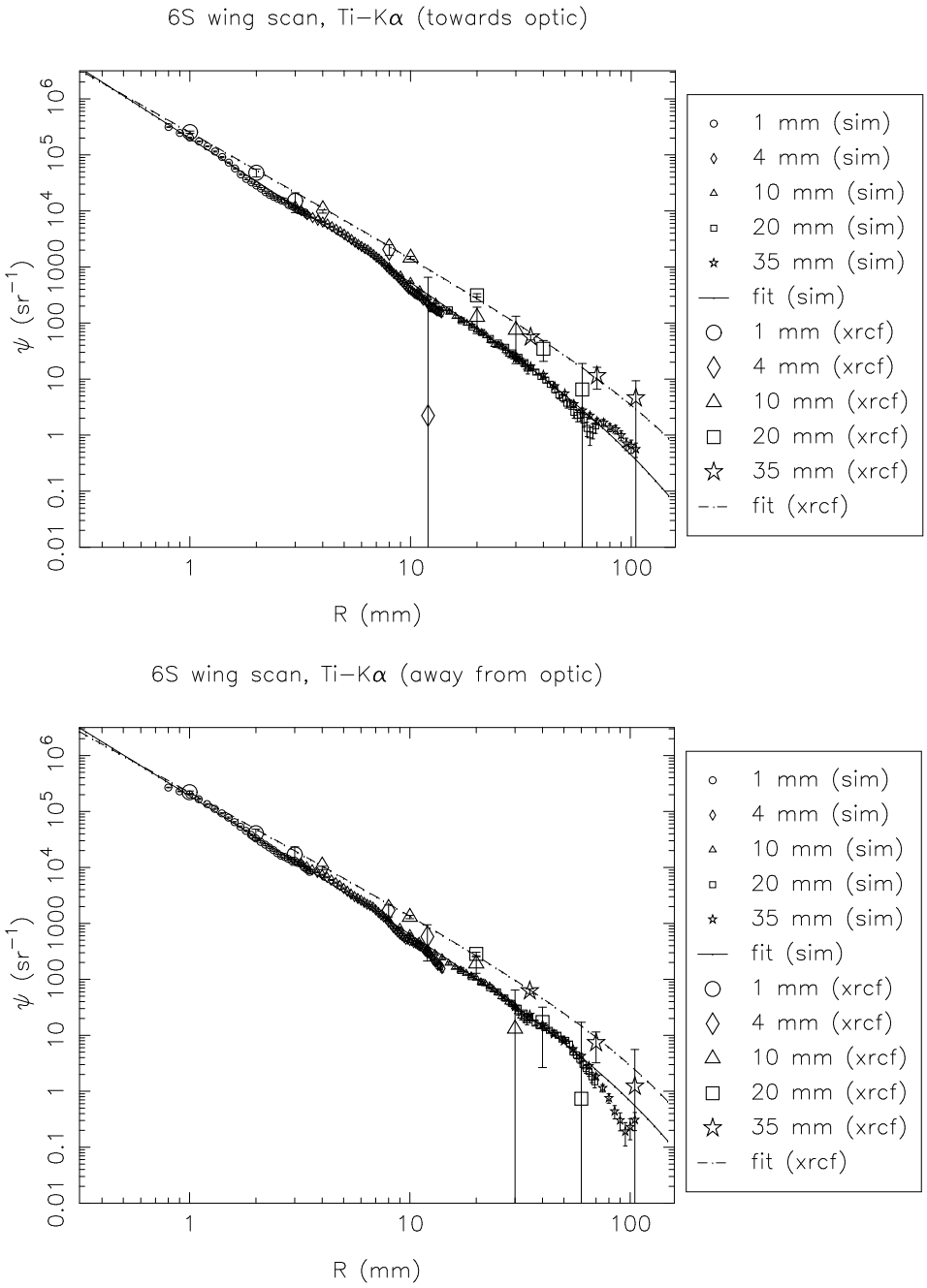

Figure 15.35: Shell 6S: Ti-Kα surface brightness, towards and away from the optic

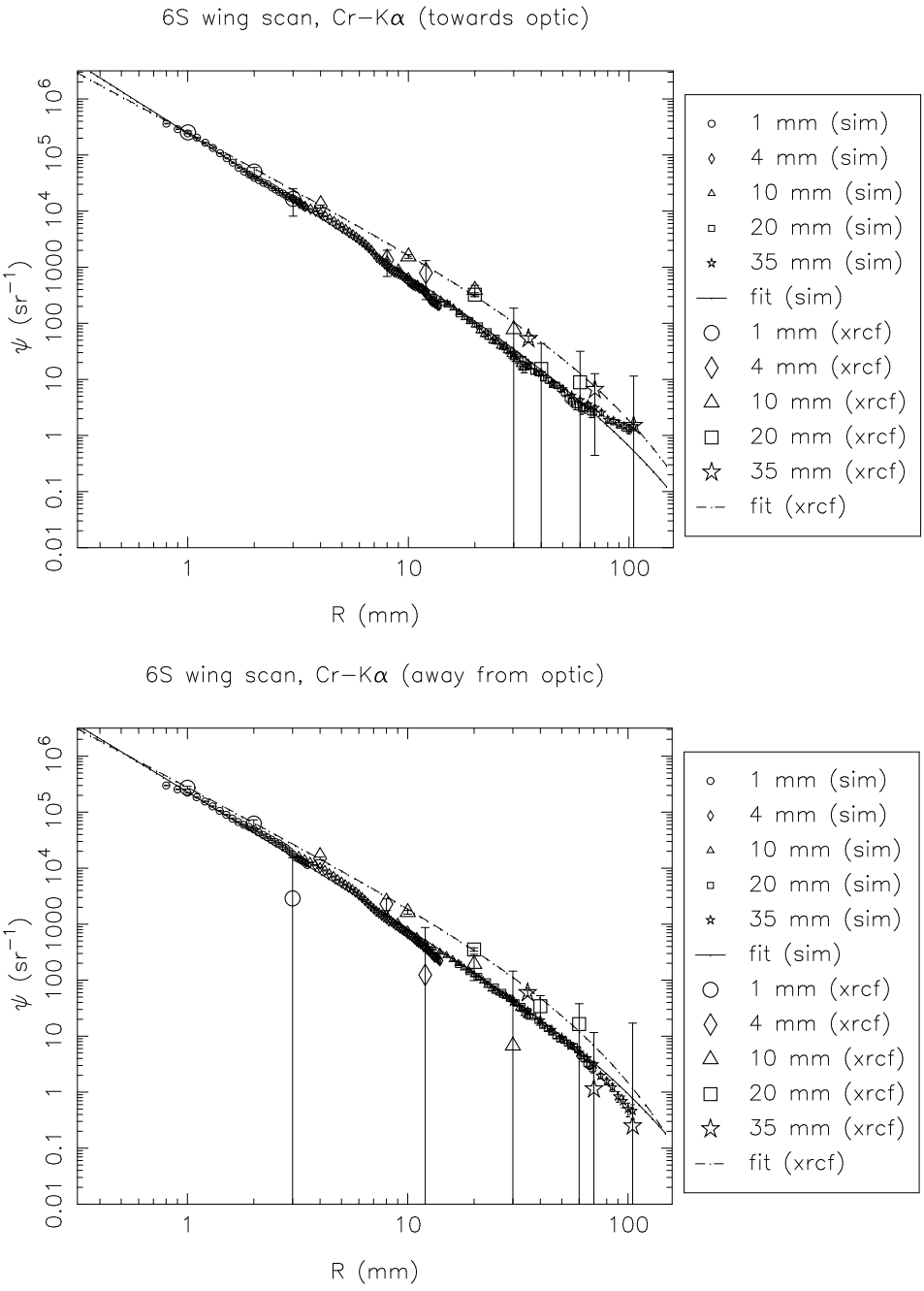

Figure 15.36: Shell 6S: Cr-Kα surface brightness, towards and away from the optic

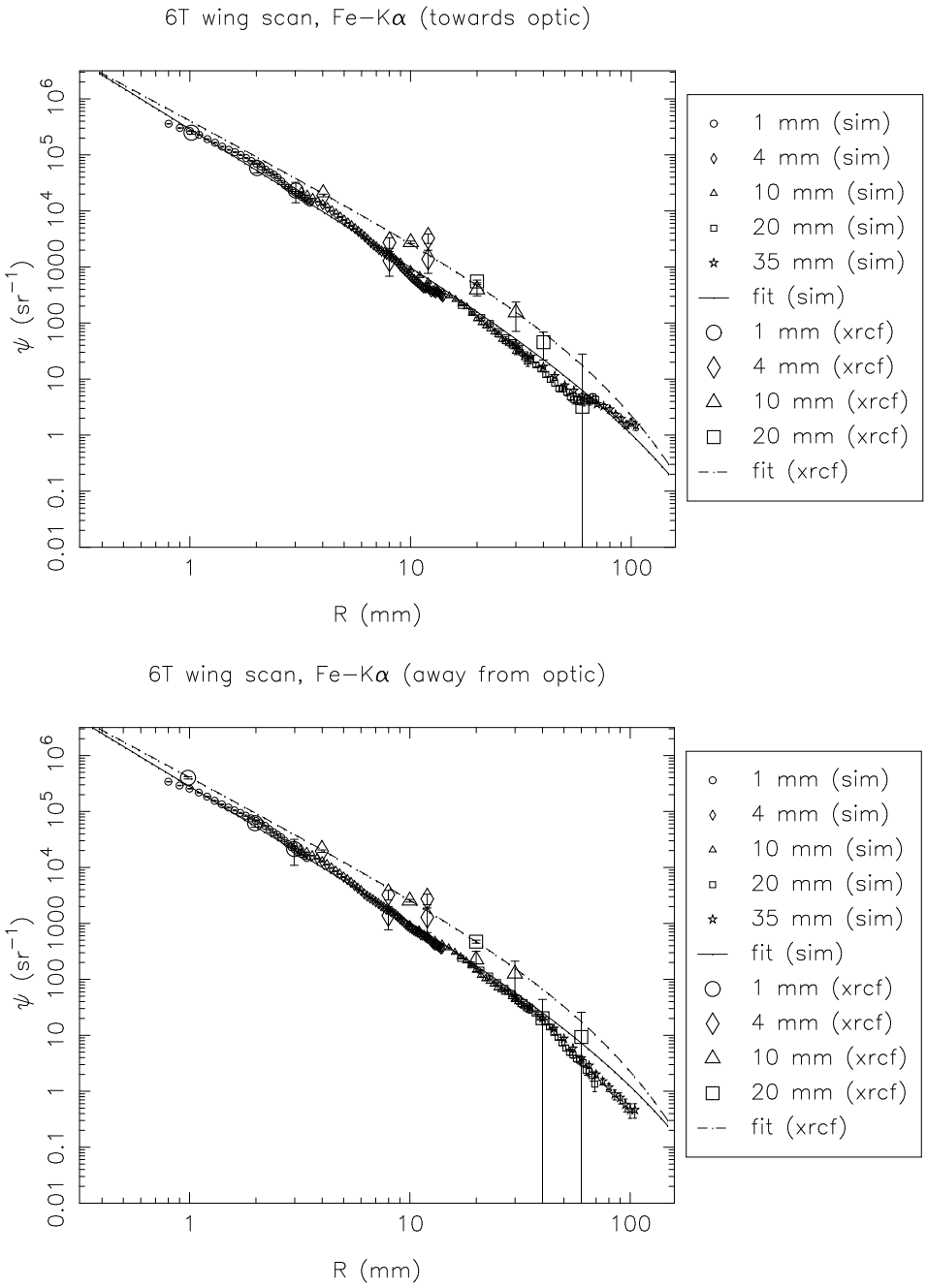

Figure 15.37: Shell 6T: Fe-Kα surface brightness, towards and away from the optic

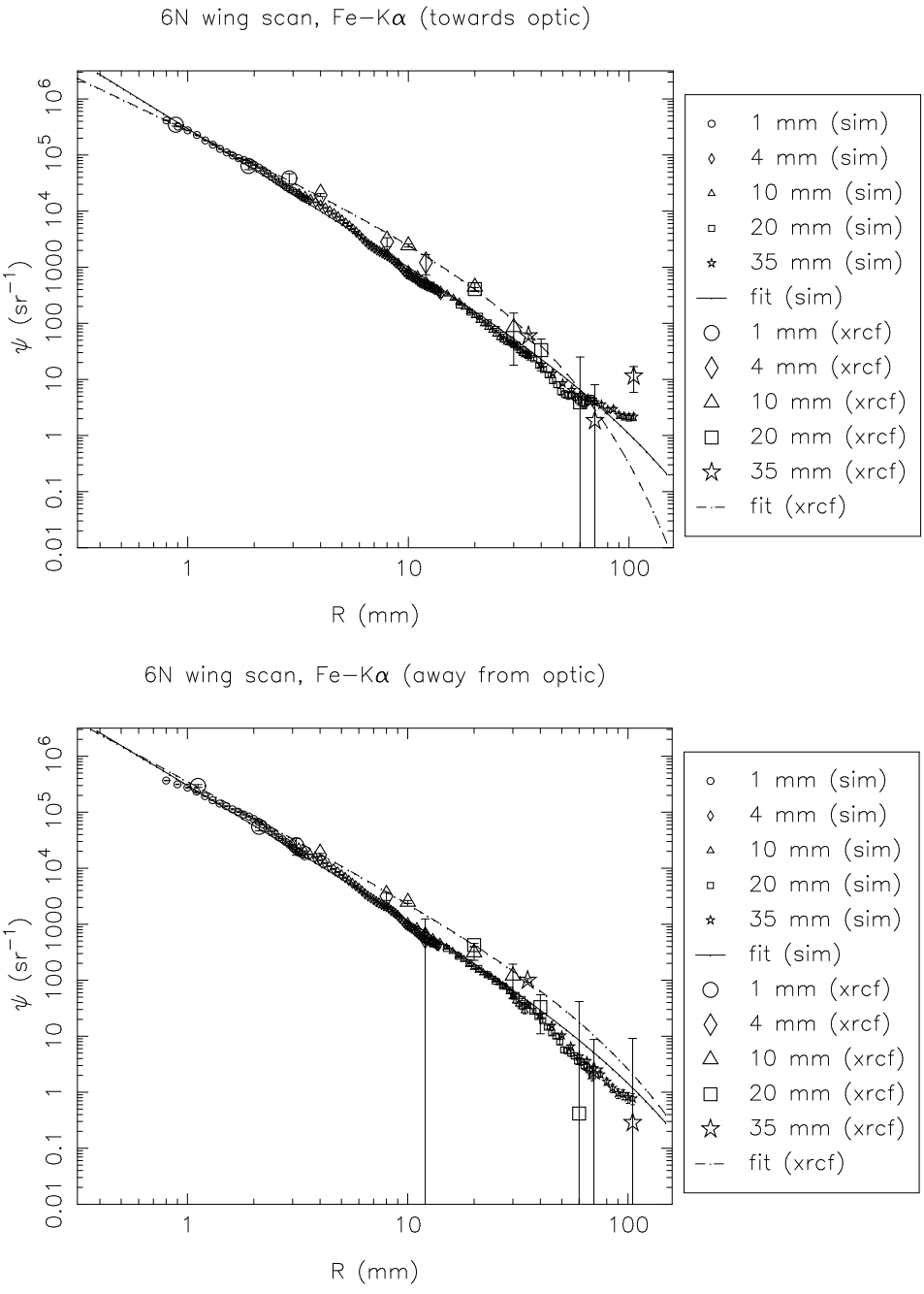

Figure 15.38: Shell 6N: Fe-Kα surface brightness, towards and away from the optic

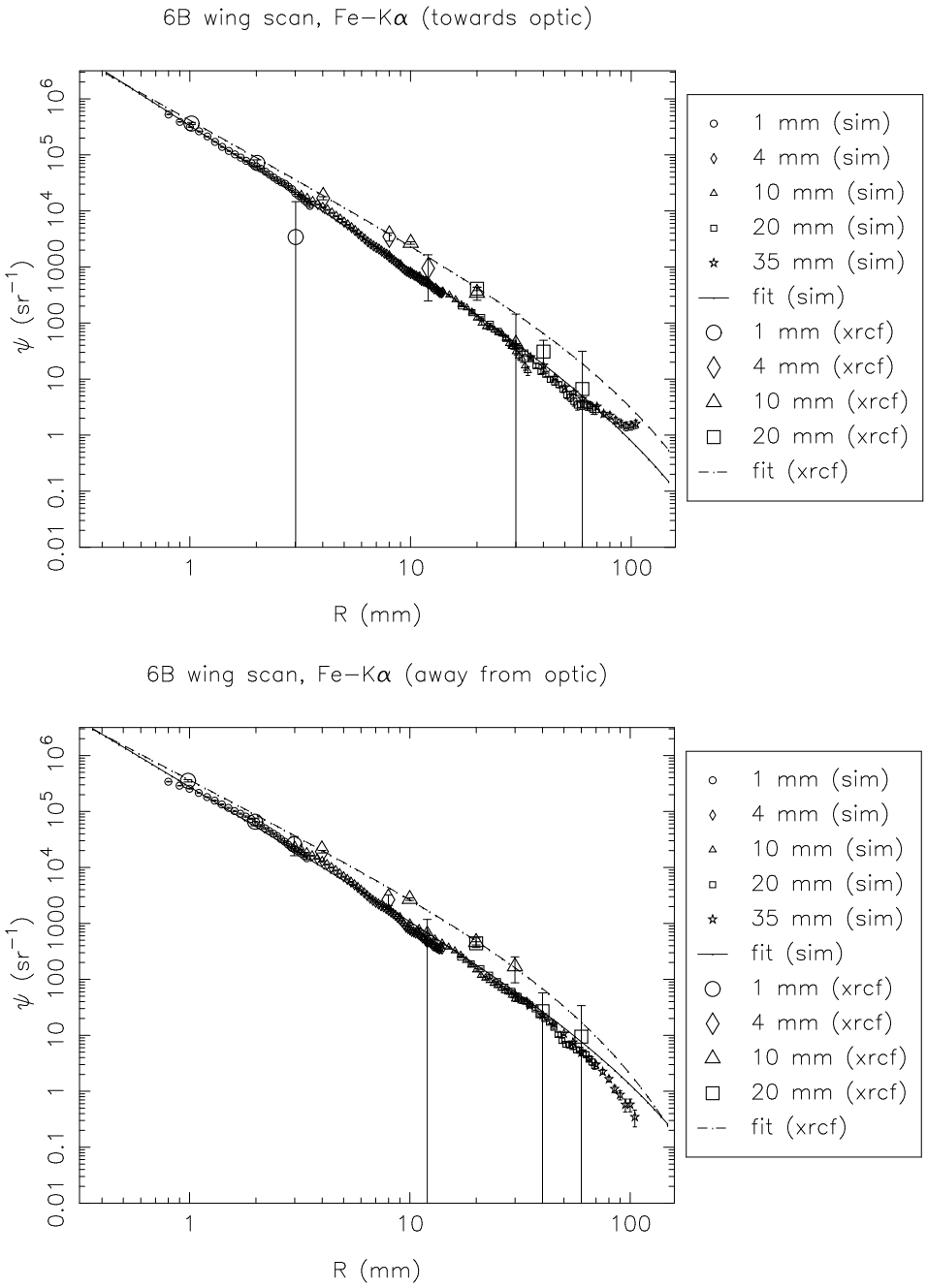

Figure 15.39: Shell 6B: Fe-Kα surface brightness, towards and away from the optic

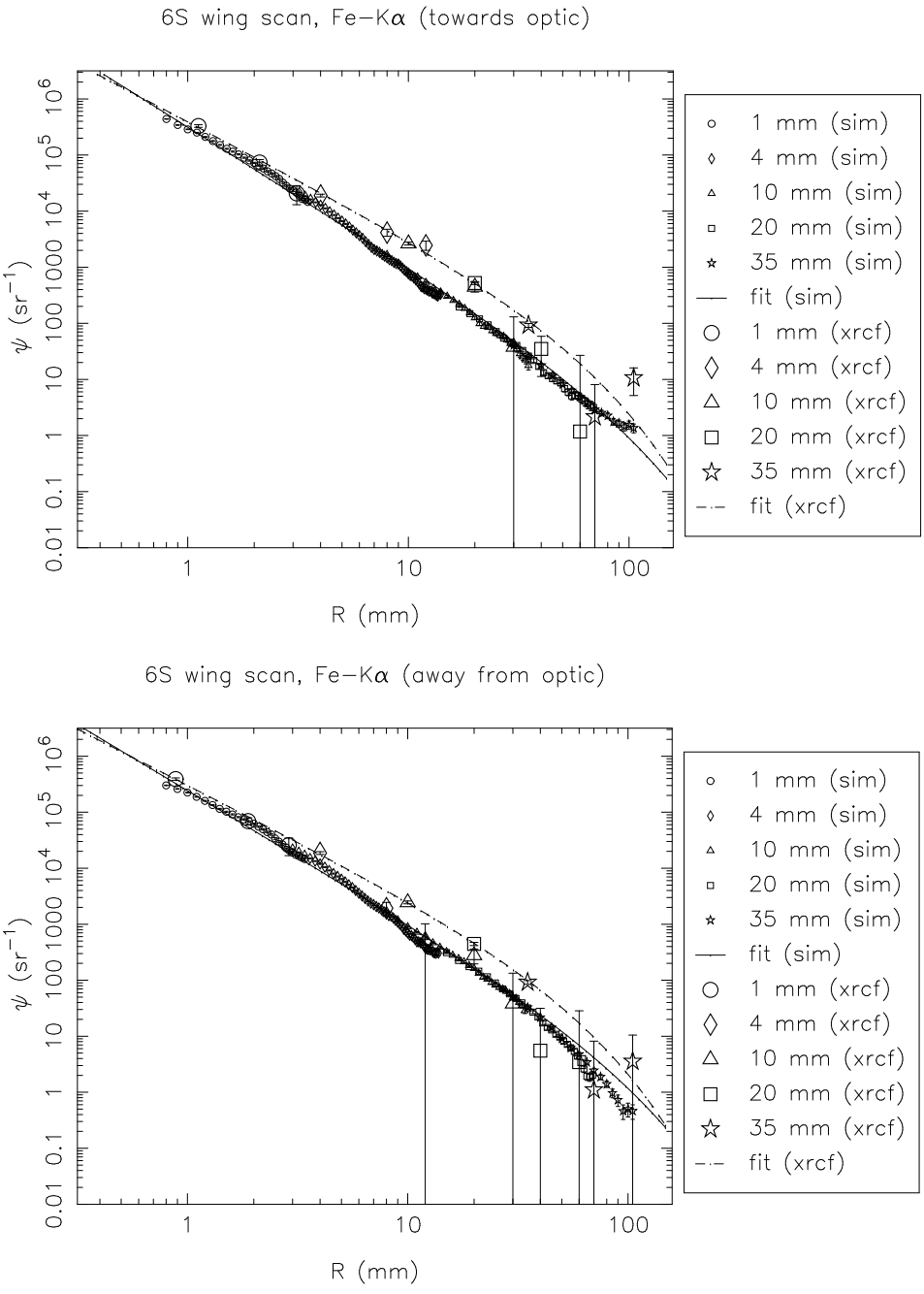

Figure 15.40: Shell 6S: Fe-Kα surface brightness, towards and away from the optic

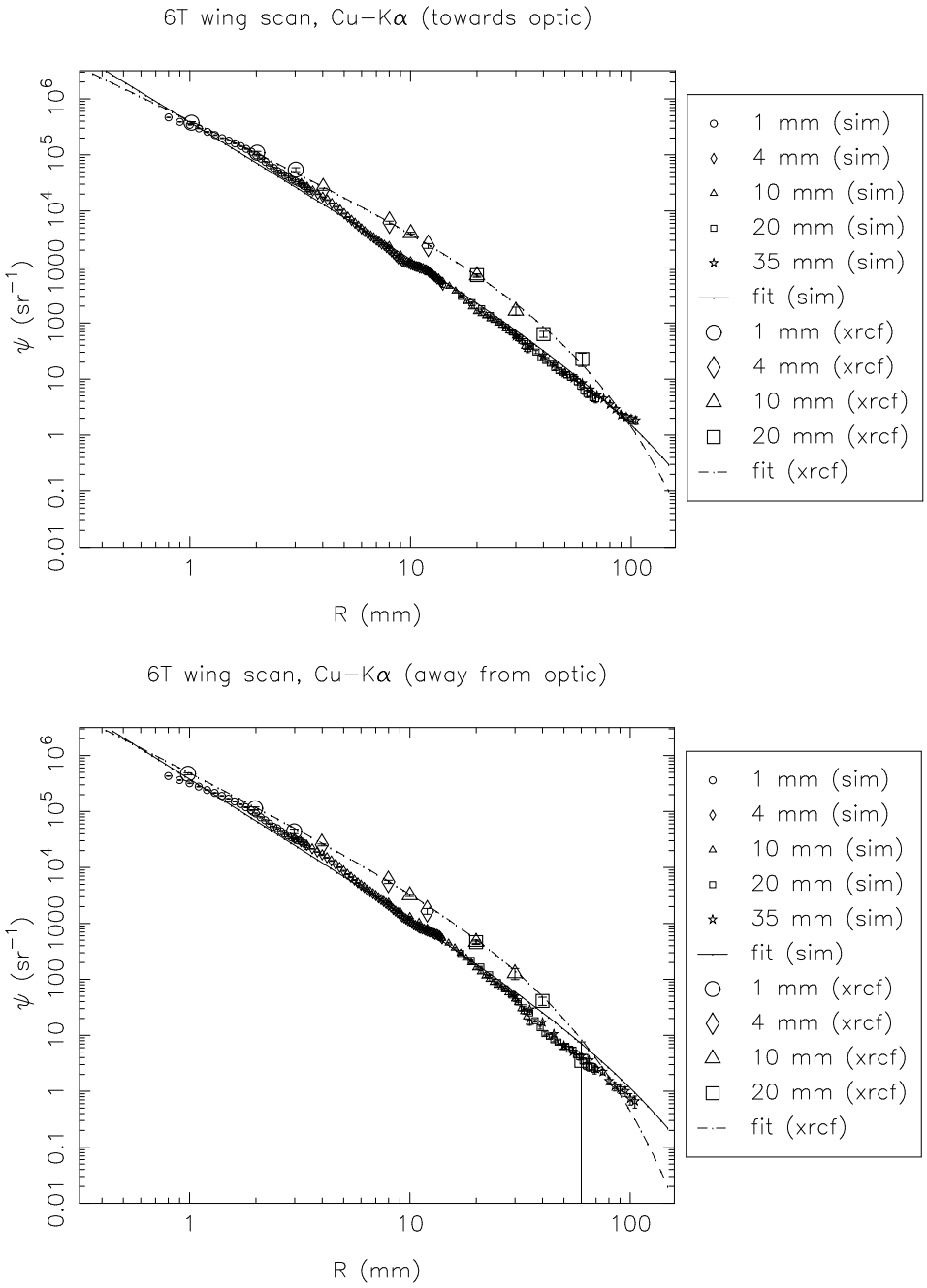

Figure 15.41: Shell 6T: Cu-Kα surface brightness, towards and away from the optic

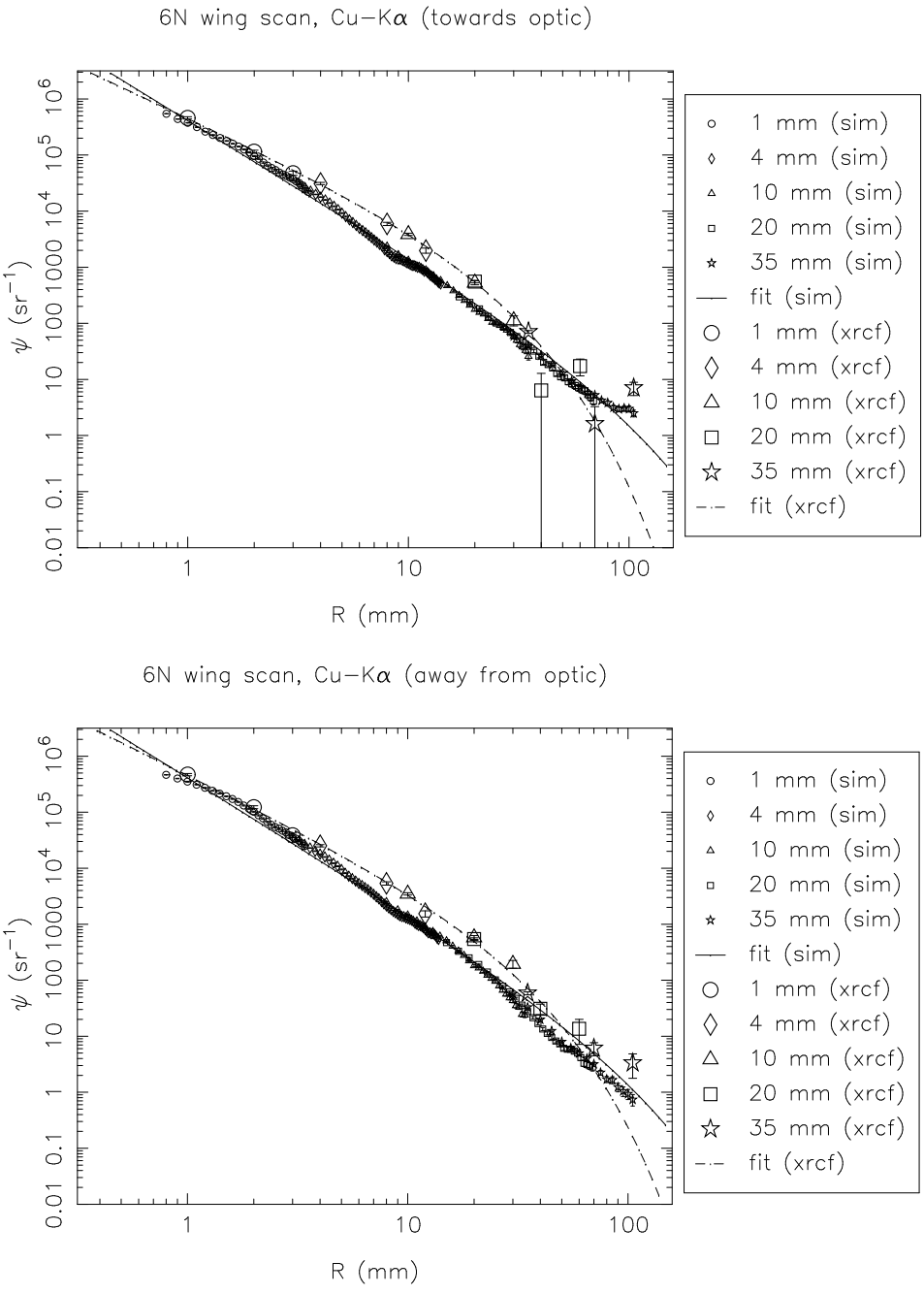

Figure 15.42: Shell 6N: Cu-Kα surface brightness, towards and away from the optic

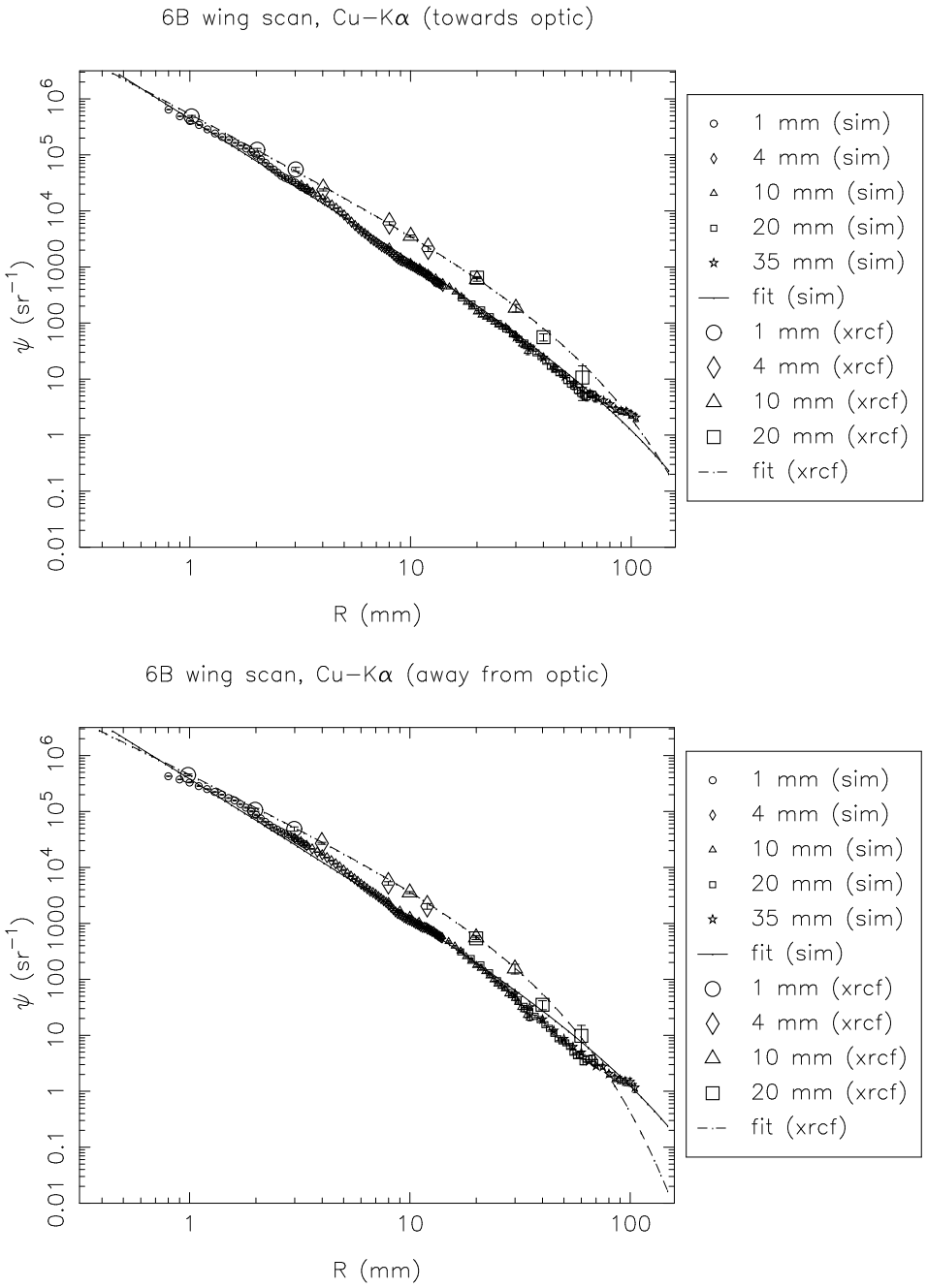

Figure 15.43: Shell 6B: Cu-Kα surface brightness, towards and away from the optic

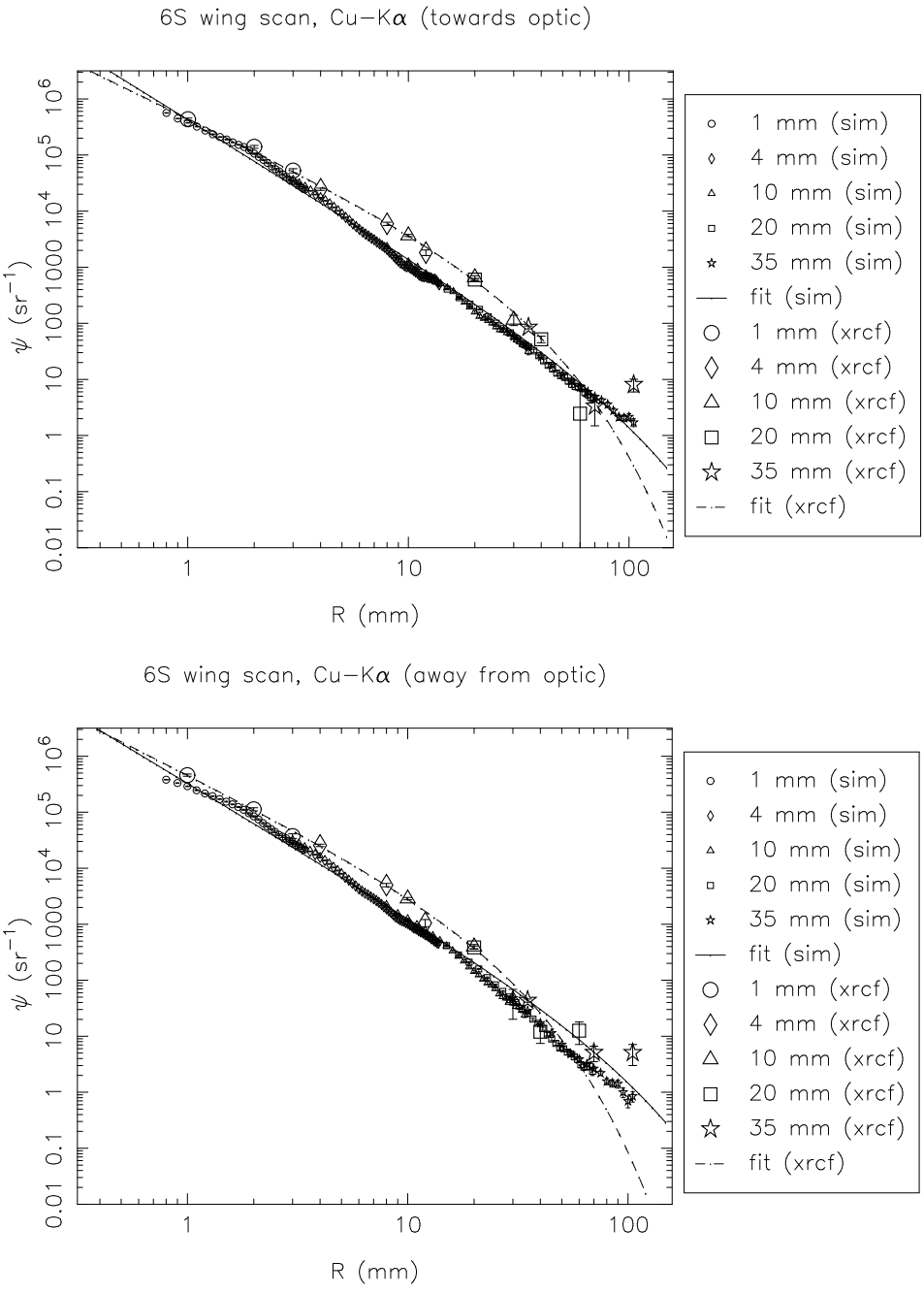

Figure 15.44: Shell 6S: Cu-Kα surface brightness, towards and away from the optic

15.2.5 Double Quadrant Scans

Table 15.9: Surface brightness fits and fractional excess effective area beyond the 35 mm pinhole. (Raytrace simulations and XRCF data, Shell 4N 4S)

Type	Quad	Line	Dir	a	b	c	fractional extra area
sim	4NS	Al	both	202617.000	3.204	10000.000	0.000137
xrcf	4NS	Al	both	254343.000	2.500	54.593	0.000825

Table 15.10: Surface brightness fits and fractional excess effective area beyond the 35 mm pinhole. (Raytrace simulations and XRCF data, Shell 6N 6S)

Type	Quad	Line	Dir	a	b	c	fractional extra area
sim	6NS	Al	both	195929.000	3.167	10000.000	0.000156
xrcf	6NS	Al	both	236995.000	2.500	35.660	0.000437

The surface brightness profiles for the double-quadrant scans are presented in Figure 15.45.

15.3 Out-of-Plane Scattering

Two sets of wing scans were conducted for which the scan was transverse to the direction of the quadrant. The first was the set of 6B Y-scans performed at C-Kα; these scans were intended to look for signs of dust scattering. The scattering from microroughness is mainly in-plane, and an excess out-of-plane component might be produced by dust scattering. The second set of scans were the 3B Y-scans at Al-Kα. These were performed in order to correct the double-quadrant wing scans (6N6S, 4N4S) for the fact that the 3B quadrant shutter was sticking and was open during the scans. The surface brightnesses based on these scans are plotted in Figure 15.46. For comparison, in-plane scans for the same shell and quadrant are also shown. Note, however, that the 3B out-of-plane scans were with HRMA at zero pitch and yaw, while the 3B in-plane scans were performed with HRMA yawed.

The out-of-plane component for the scattering due to microroughness is expected to be smaller than the in-plane component by a factor of order $\sin\alpha$ where α is the graze angle for the given shell. For shell 3 this factor would be about 1/83, while for shell 6 the factor would be about 1/130. The raytrace for the transverse scan for shell 6B at C-Kα suggests that the raytrace model may be lower in wing surface brightness by perhaps a factor of 10; however, the raytrace has very few counts in the wings, and the 10 mm pinhole positions show no counts this far into the wings. Longer raytraces are needed before the questions can be answered definitively. It is also worth noting that in the current scattering model, the out-of-plane component is calculated as $\sin\alpha$ times the in-plane component; this treatment may be too simplistic. The 3B out-of-plane scan data indicate a flatter slope than in the raytrace data, but this probably is not significant given the small number of data points and the large uncertainties in the values.

In Chapter 14, it was noted that the X-ray data for the 4 mm pinhole effective areas were peculiar in that the pinhole effective area for the position 4 mm to one side of the core was more than a factor of 10 larger than the corresponding position on the other side of the core (both for

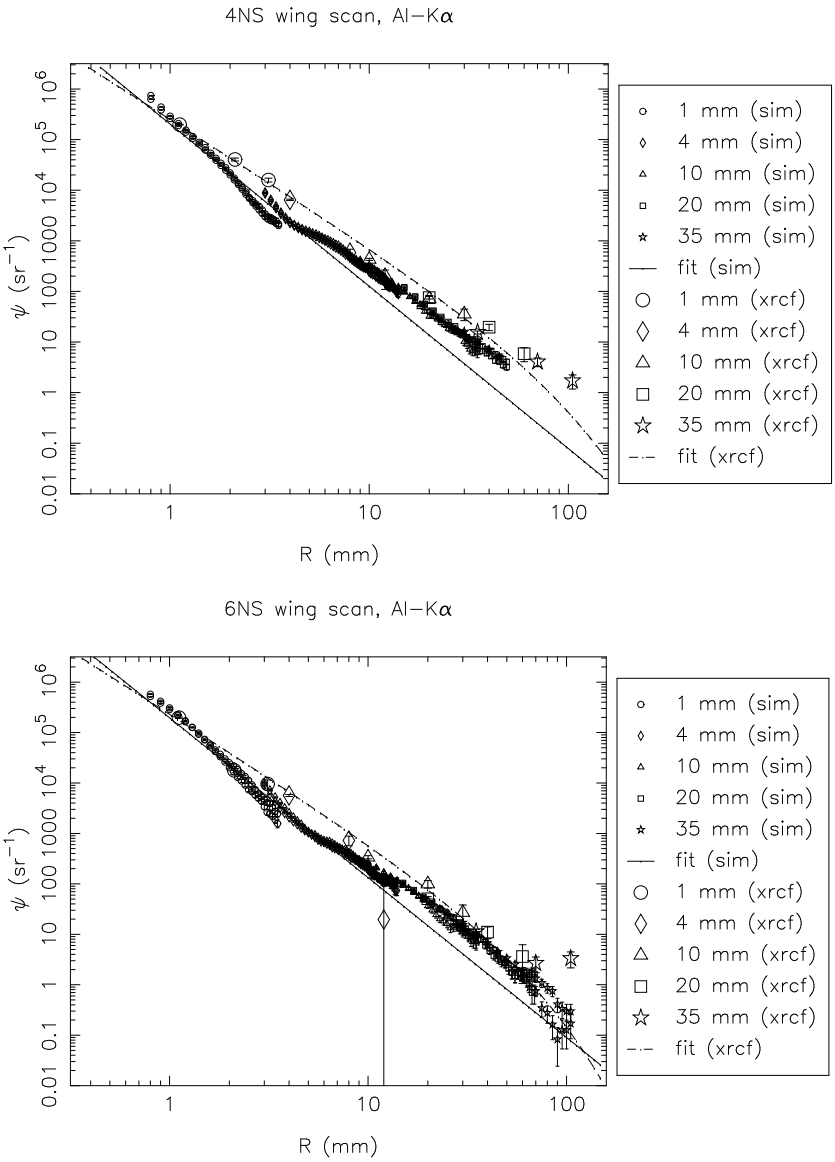

Figure 15.45: Double quadrant wing scan surface brightness: Al-Kα. Top: Shell 4, N and S quadrant. Bottom: Shell 6, N and S quadrant.

the in-plane and out-of-plane cases). In Figure 15.46 these are the diamond-shaped points at $R = 4$ mm.

15.4 Comparison with Encircled Energy Data

In order to show the consistency between the wing scan surface brightness data and the encircled energy data, we have plotted in Figure 15.47 the surface brightness profile measured in two different ways, for the one case for which this is feasible. The encircled energy tests are described in Chapter 16; these tests give a measurement of the surface brightness integrated out to the radius of a given aperture centered on the peak of the distribution, so numerically differentiating the effective area *vs.* radius curve gives us the surface brightness profile. In order to make a direct

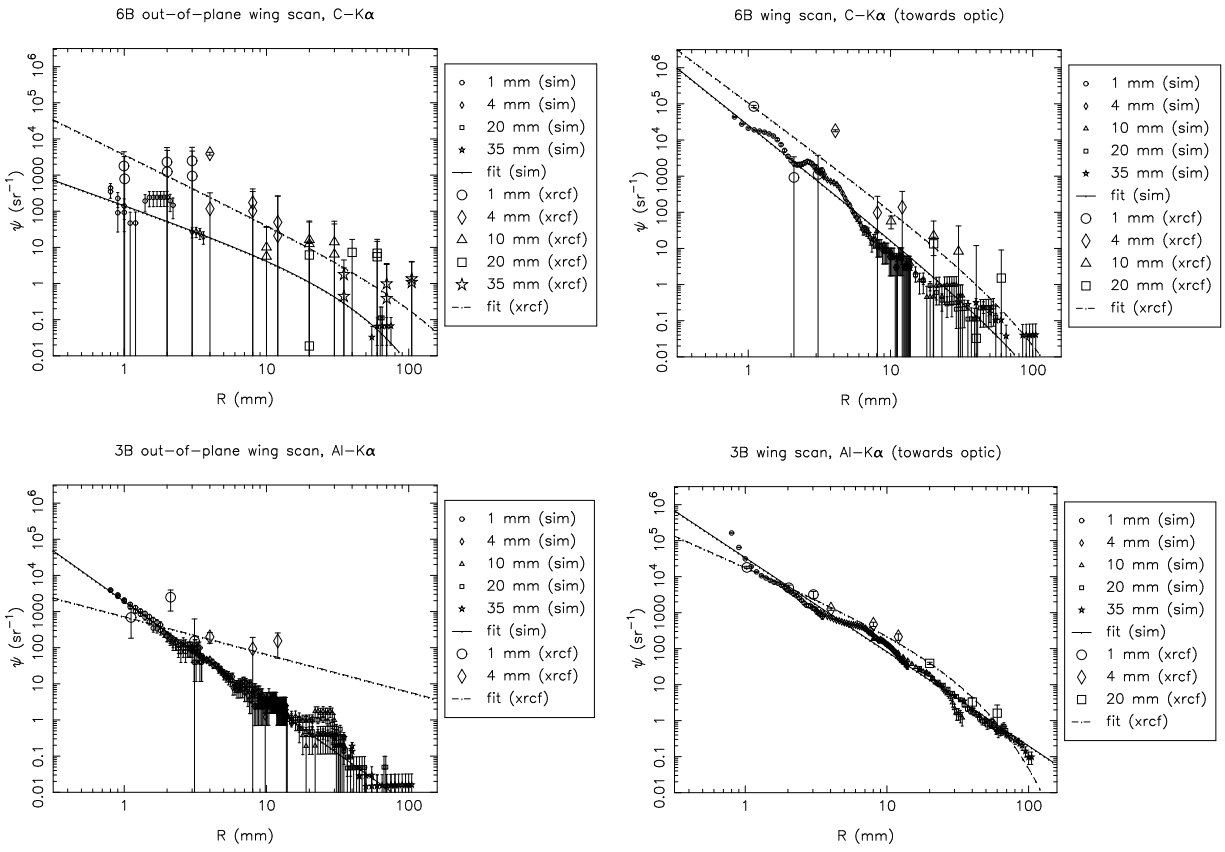

Figure 15.46: Out-of-plane scans, compared to in-plane scans. Top left: 6B Y scan at C-Kα (out of plane). Top right: 6B Z scan at C-Kα (in plane, towards optic). Bottom left: 3B Y scan at Al-Kα (out of plane). Bottom right: 3B Z scan at Al-Kα (in plane).

comparison with the wingscan surface brightness measurements, the surface brightness obtained by differentiating the effective area curve was scaled by a factor of $2 \times 88/360$ times the effective area within an on-axis 35 mm diameter pinhole, to account for the fact that the wing scans were done one quadrant at a time (see §15.2). This surface brightness and that for the 1S Ti-Kα wing scan are plotted in Figure 15.47. The case of Ti K-α for Shell 1 is unique in that the encircled energy curve is both steep enough in the outer parts and well enough measured that the numerical derivative can be computed with finite error bars. Other cases examined showed the wing scan data at a level not inconsistent with the encircled energy data, but due to the large error bars on the latter, no stronger conclusions can be drawn. Note also the HRMA was yawed by $-1'$ during this effective area experiment and by $-4.56'$ in this wing scan measurement (see §D.7.2 and Table 14.3).

15.5 "$2W_1$" Profiles

Finally, given the surface brightness profiles for various energies, the "$2W_1$" functions describing the surface can be evaluated. The value of $2W_1$ is based on equation (7) of O'Dell et al. (1992):

$$2W_1(f) \simeq \frac{f\psi(\theta)\lambda^4}{16\pi \sin^4 \alpha} \tag{15.9}$$

where $f = \theta \sin\alpha/\lambda$ is the spatial frequency, θ is the off-axis angle, α is the mean graze angle for the mirror shell, λ is the X-ray wavelength, and ψ is the surface brightness normalized to a scaled on-axis effective area measured using the largest 35 mm pinhole (see §15.2 and also the MST preliminary report).

It should be emphasized that the PSD thus calculated is *per surface*.

The resulting $2W_1$ data are fit with functions of the form

$$2W_1(f) = af^{-b}e^{-f/c}. \tag{15.10}$$

Again, the raytrace data are not fit well by this particular form; as for the surface brightness fits to the raytrace data, the exponential scale length parameter was limited to fall within a given range of values, in this case 190–10000. The lower limit (obtained by trial and error) was chosen to reproduce approximately the overall shape of the curve at large radius. As before, the overall shape fits reasonably well in some cases but not in others; in future analyses, different limit ranges should be applied on a case by case basis.

In the following tables and figures, the $2W_1$ obtained from the X-ray data are compared to the $2W_1$ based on the raytrace simulations.

The agreement between the XRCF data and the raytrace simulations seems to be generally better towards smaller f values. The agreement towards larger f gets significantly worse, particularly for the larger shells. The raytrace models for shell 6 indicate a high shoulder towards small f; the X-ray data shows some support for this (see Figures 15.60–15.63).

The mean-square "roughness" values derived from the fits also shows the increasing discrepancy towards larger values for spatial frequency. The σ^2 evaluated for 1–10 mm^{-1} agree much better

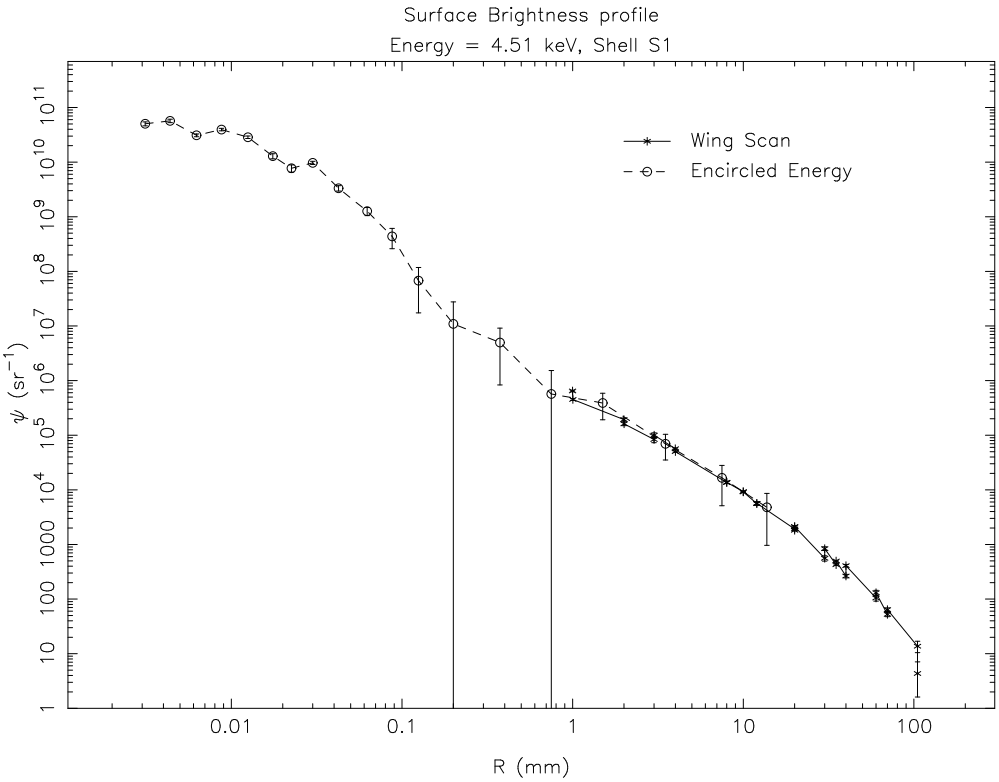

Figure 15.47: Surface Brightness *vs.* Radius for Shell 1S at Ti K-α. This is a composite plot based on both wing scan data and an encircled energy test.

than the values for 100–1000 mm^{-1}. Comparing the values derived from the fits by integrating from 1–1000 mm^{-1}, it can be seen that for shells 1 and 3, the XRCF values are about a factor of two higher than the raytrace values, about a factor of 1.7 higher for shell 4, and about 1.3 times higher for shell 6; generally, the discrepancy tends to be smaller for the smaller shells. The values for the XRCF data fits for scattering towards *vs.* away from the optic seem to be comparable except in the case of shell 3, in which case the derived roughness is considerably larger for directions away from the optic than towards the optic. As noted in the discussion of the surface brightnesses, this effect (if real, and not an artifact of the reductions and analysis) is currently not understood.

Finally, derived roughnesses from the double-quadrant scans (integrated over 1–1000 mm^{-1}) are about 3 to 3.5 times larger than the corresponding single-quadrant scans. The data were processed for the double-quadrant scans using the same value for a_{eff}^{tot} as in the single quadrant scans (see Eq. Eq. 15.1); this factor should have been a factor of two larger for the double-quadrant scans (two quadrants now contribute) so a factor of 2 of the discrepancy is explained by the normalization factor. The remaining discrepancy may be in part a result of the differences in the experimental setup (*e.g.*, the HRMA was not pitched or yawed in the double-quadrant scans), or a bias resulting from the paucity of double-quadrant data points. However, the discrepency appears to be larger than can be easily explained by such effects.

15.5.1 Shell 1 scans

Table 15.11: Single quadrant wingscan $2W_1$ fits and mean square roughness (Raytrace simulation and XRCF data, Shell 1)

Type	Quad	Dir	a	b	c	σ^2_{1-10}	σ^2_{10-100}	$\sigma^2_{100-1000}$	σ^2_{1-1000}
sim	1T	in	6.935	1.238	190.000	12.062	5.935	1.060	19.056
sim	1T	out	3.828	1.104	190.000	7.689	5.111	1.177	13.978
sim	1N	in	6.914	1.221	190.000	12.249	6.269	1.158	19.676
sim	1N	out	4.612	1.129	190.000	9.011	5.663	1.244	15.918
sim	1B	in	7.941	1.247	190.000	13.689	6.608	1.161	21.458
sim	1B	out	3.863	1.069	190.000	8.059	5.783	1.420	15.263
sim	1S	in	7.969	1.247	190.000	13.738	6.631	1.165	21.534
sim	1S	out	3.692	1.068	190.000	7.711	5.548	1.366	14.625
xrcf	T	in	6.100	1.009	761.127	13.830	12.944	8.396	35.170
xrcf	T	out	5.791	0.947	271.357	13.975	13.888	5.783	33.647
xrcf	N	in	5.891	0.921	182.656	14.553	14.440	4.498	33.491
xrcf	N	out	5.350	0.895	210.773	13.670	14.729	5.493	33.892
xrcf	B	in	5.824	1.062	800.000	12.438	10.335	6.093	28.866
xrcf	B	out	3.948	0.870	236.156	10.415	12.077	5.208	27.700
xrcf	S	in	3.844	0.871	245.184	10.135	11.789	5.236	27.160
xrcf	S	out	7.816	1.041	314.447	16.965	13.871	5.347	36.184

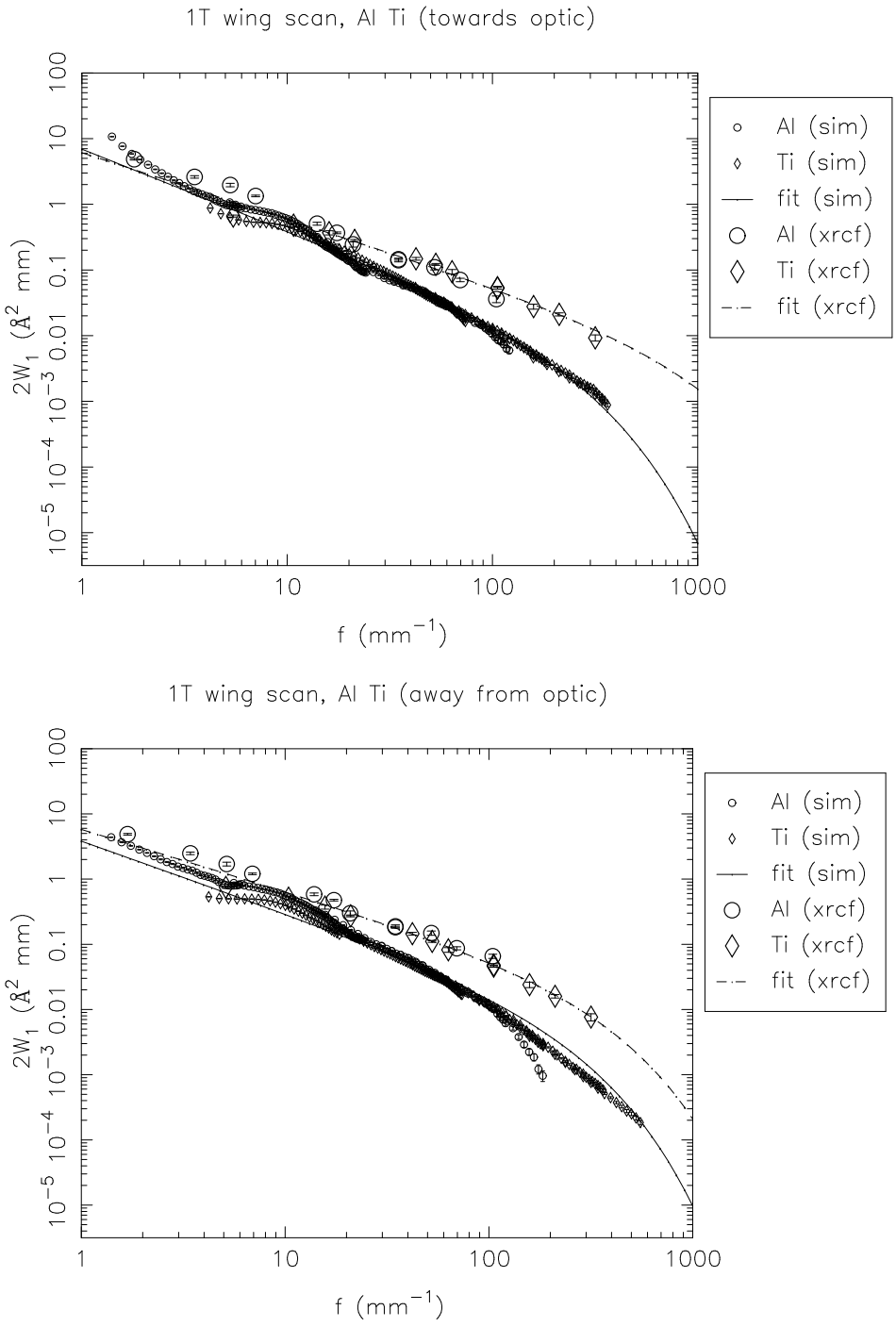

Figure 15.48: Shell 1T: $2W_1$ profiles, towards and away from the optic. XRCF data (*xrcf*) *vs.* raytrace data (*sim*).

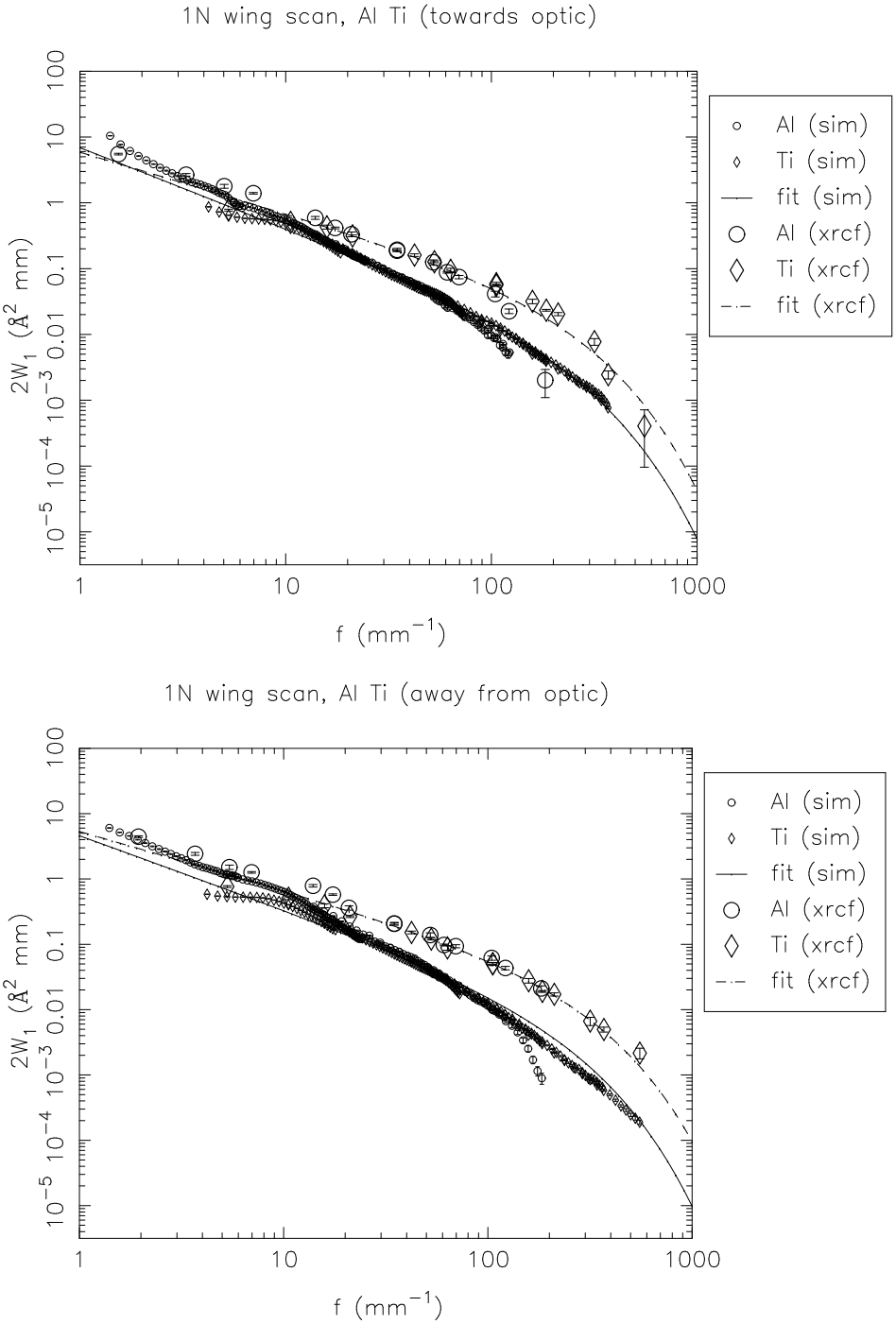

Figure 15.49: Shell 1N: $2W_1$ profiles, towards and away from the optic. XRCF data (*xrcf*) *vs.* raytrace data (*sim*).

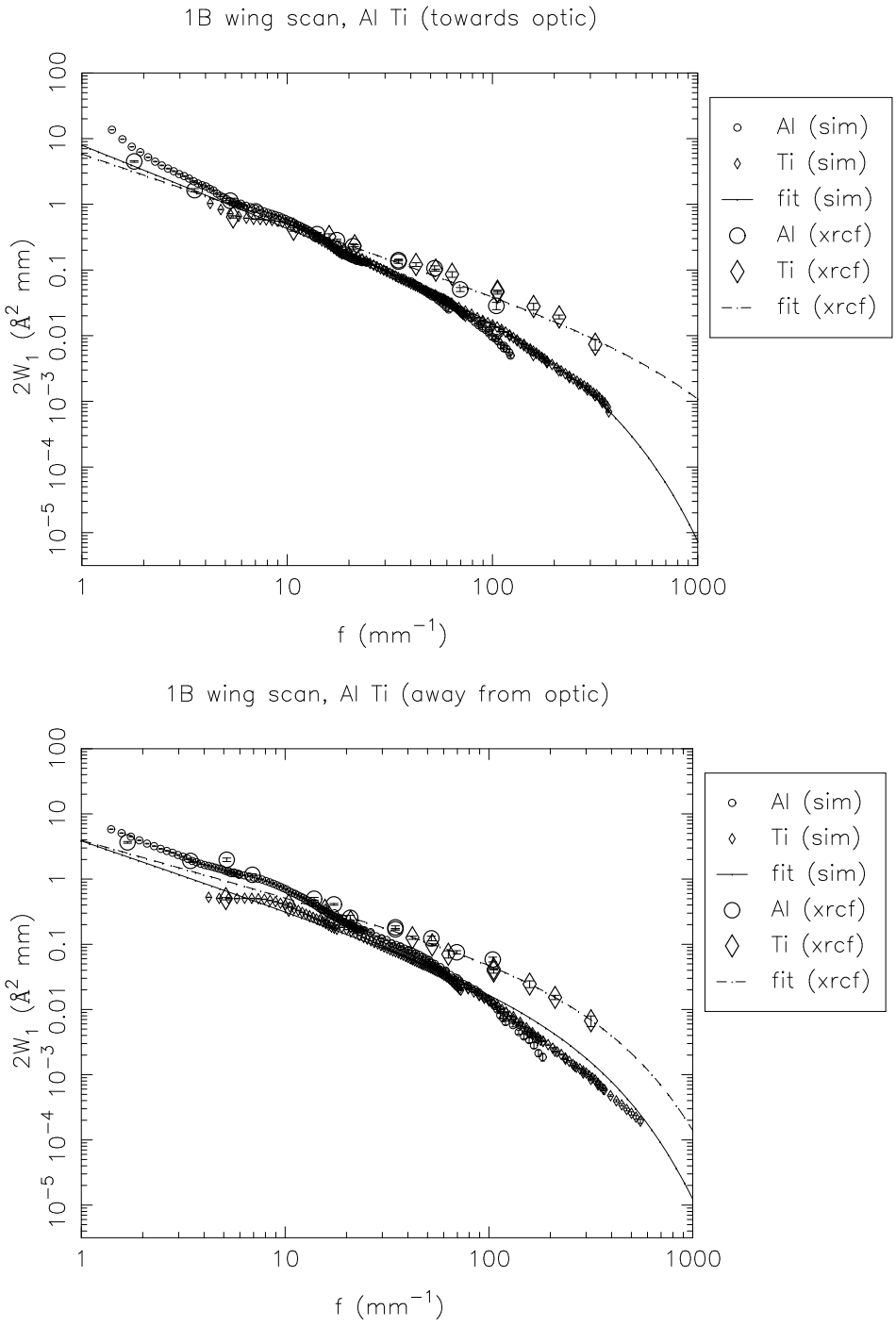

Figure 15.50: Shell 1B: $2W_1$ profiles, towards and away from the optic. XRCF data (*xrcf*) *vs.* raytrace data (*sim*).

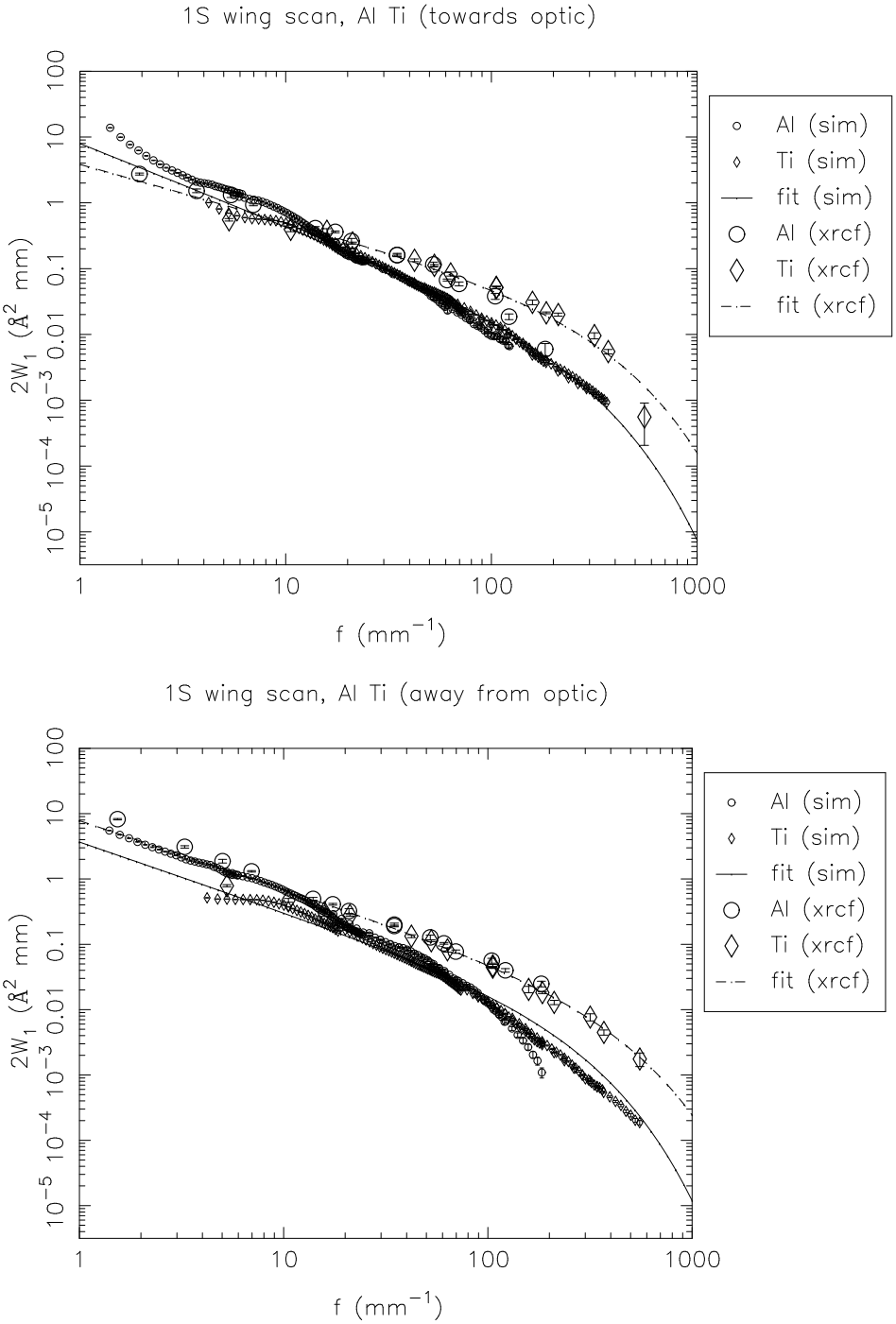

Figure 15.51: Shell 1S: $2W_1$ profiles, towards and away from the optic. XRCF data (*xrcf*) *vs.* raytrace data (*sim*).

15.5.2 Shell 3 scans

Table 15.12: Single quadrant wingscan $2W_1$ fits and mean square roughness (Raytrace simulation and XRCF data, Shell 3)

Type	Quad	Dir	a	b	c	σ^2_{1-10}	σ^2_{10-100}	$\sigma^2_{100-1000}$	σ^2_{1-1000}
sim	3T	in	3.999	1.555	2622.350	5.191	1.431	0.360	6.982
sim	3T	out	2.563	1.401	190.000	3.786	1.294	0.169	5.250
sim	3N	in	4.831	1.582	666.650	6.099	1.533	0.278	7.911
sim	3N	out	2.729	1.376	190.000	4.131	1.493	0.205	5.829
sim	3B	in	4.254	1.542	454.649	5.557	1.502	0.256	7.316
sim	3B	out	2.509	1.389	190.000	3.750	1.318	0.176	5.244
sim	3S	in	3.960	1.508	210.044	5.296	1.445	0.166	6.907
sim	3S	out	2.341	1.400	190.000	3.462	1.187	0.155	4.803
xrcf	T	in	3.283	1.215	800.000	5.936	3.477	1.475	10.888
xrcf	T	out	12.797	1.712	500.000	14.402	2.656	0.329	17.386
xrcf	N	in	2.537	1.138	360.117	4.954	3.295	1.142	9.390
xrcf	N	out	12.378	1.609	488.997	15.230	3.548	0.542	19.320
xrcf	B	in	2.069	1.021	168.669	4.546	3.558	0.855	8.959
xrcf	B	out	5.237	1.336	443.104	8.332	3.592	0.930	12.854
xrcf	S	in	2.243	1.084	287.982	4.635	3.407	1.136	9.177
xrcf	S	out	3.704	1.217	210.807	6.600	3.460	0.703	10.763

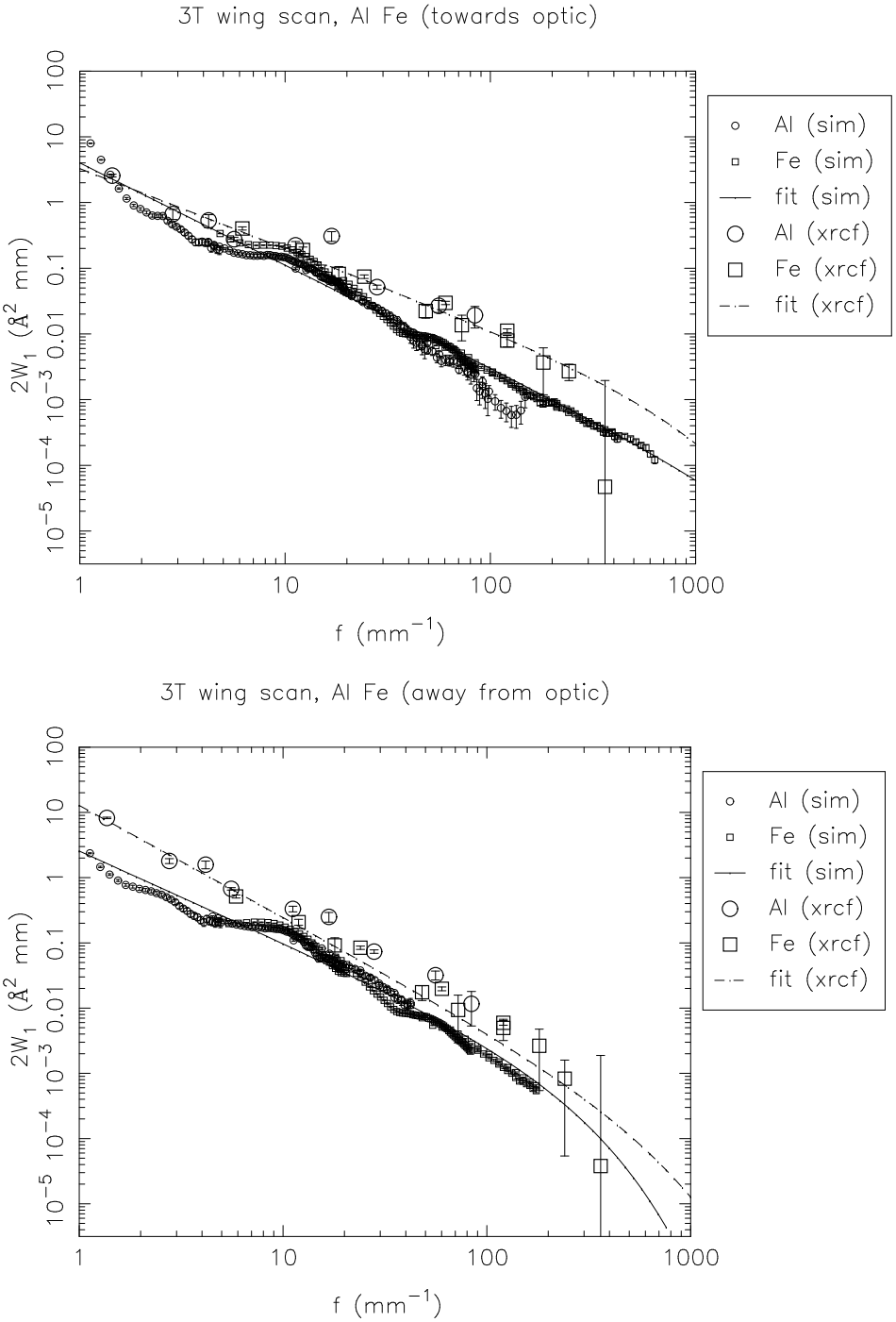

Figure 15.52: Shell 3T: $2W_1$ profiles, towards and away from the optic. XRCF data (*xrcf*) *vs.* raytrace data (*sim*).

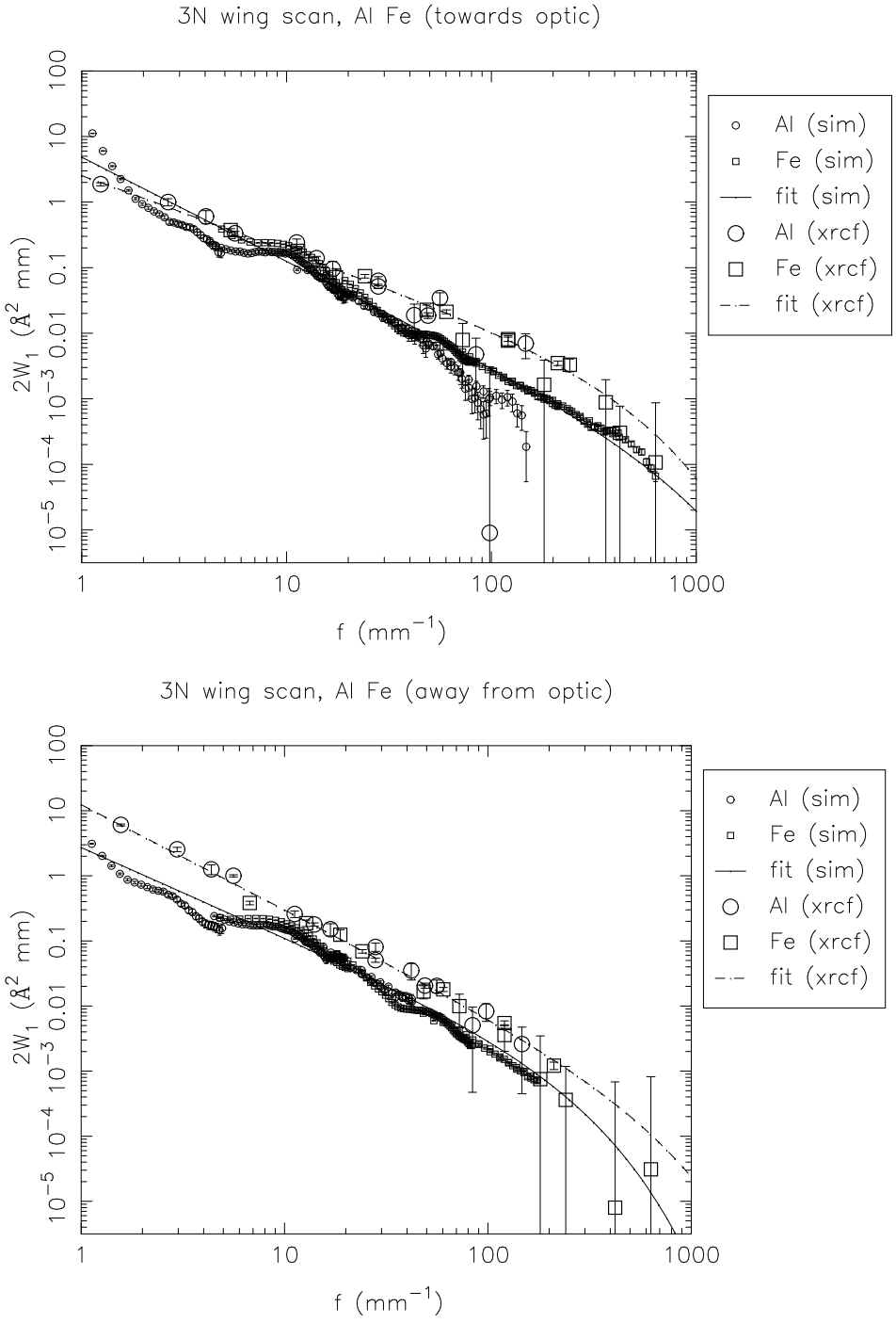

Figure 15.53: Shell 3N: $2W_1$ profiles, towards and away from the optic. XRCF data (*xrcf*) *vs.* raytrace data (*sim*).

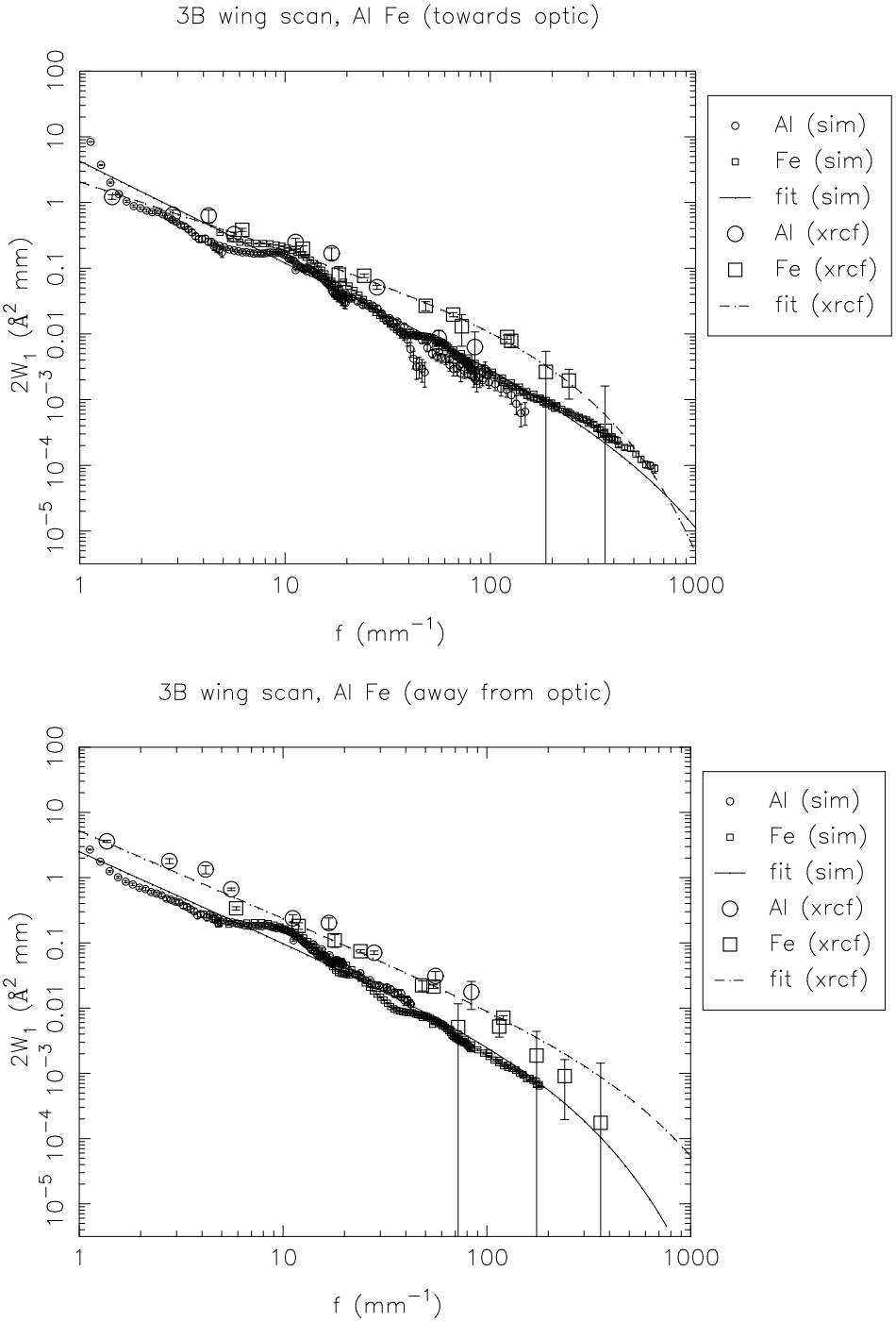

Figure 15.54: Shell 3B: $2W_1$ profiles, towards and away from the optic. XRCF data (*xrcf*) *vs.* raytrace data (*sim*).

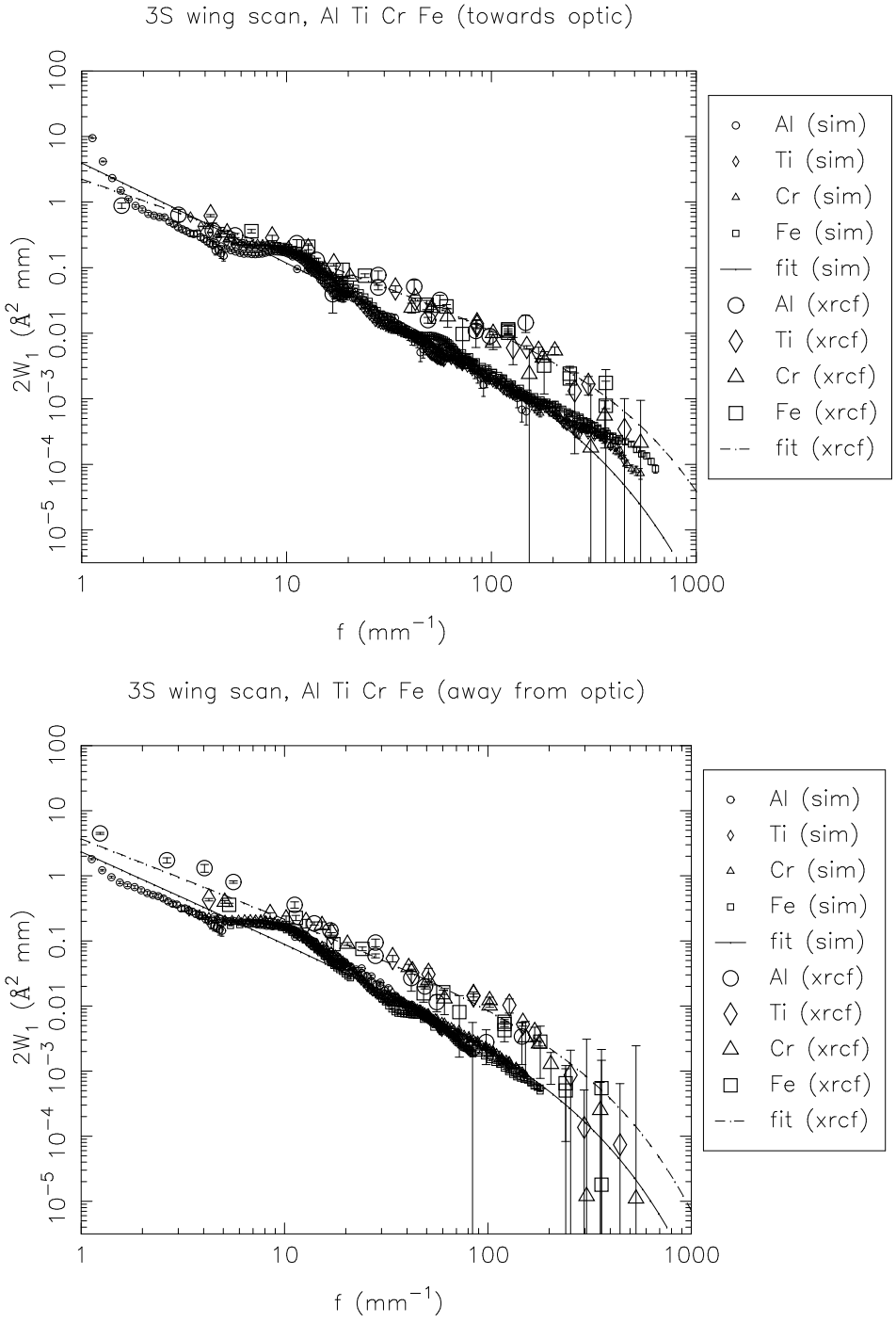

Figure 15.55: Shell 3S: $2W_1$ profiles, towards and away from the optic. XRCF data (*xrcf*) *vs.* raytrace data (*sim*).

15.5.3 Shell 4 scans

Table 15.13: Single quadrant wingscan $2W_1$ fits and mean square roughness (Raytrace simulation and XRCF data, Shell 4)

Type	Quad	Dir	a	b	c	σ^2_{1-10}	σ^2_{10-100}	$\sigma^2_{100-1000}$	σ^2_{1-1000}
sim	4T	in	4.183	1.462	10000.000	5.929	2.042	0.685	8.656
sim	4T	out	3.013	1.363	346.607	4.657	1.854	0.398	6.909
sim	4N	in	14.699	1.945	10000.000	13.784	1.560	0.173	15.518
sim	4N	out	4.619	1.438	434.562	6.648	2.268	0.470	9.386
sim	4B	in	17.226	2.029	10000.000	15.176	1.418	0.130	16.724
sim	4B	out	3.610	1.384	337.913	5.466	2.073	0.421	7.960
sim	4S	in	4.815	1.481	10000.000	6.702	2.208	0.709	9.619
sim	4S	out	2.768	1.367	427.547	4.270	1.713	0.409	6.392
xrcf	T	in	11.518	1.600	800.000	14.320	3.478	0.641	18.440
xrcf	T	out	8.829	1.563	500.000	11.323	2.933	0.498	14.754
xrcf	N	in	6.997	1.413	800.000	10.354	3.857	1.067	15.278
xrcf	N	out	7.095	1.358	500.000	11.053	4.567	1.195	16.815
xrcf	B	in	20.062	1.791	800.000	21.185	3.323	0.404	24.912
xrcf	B	out	10.651	1.505	500.000	14.407	4.259	0.818	19.484
xrcf	S	in	4.283	1.189	319.651	7.907	4.634	1.347	13.888
xrcf	S	out	5.439	1.259	259.463	9.307	4.557	1.001	14.865

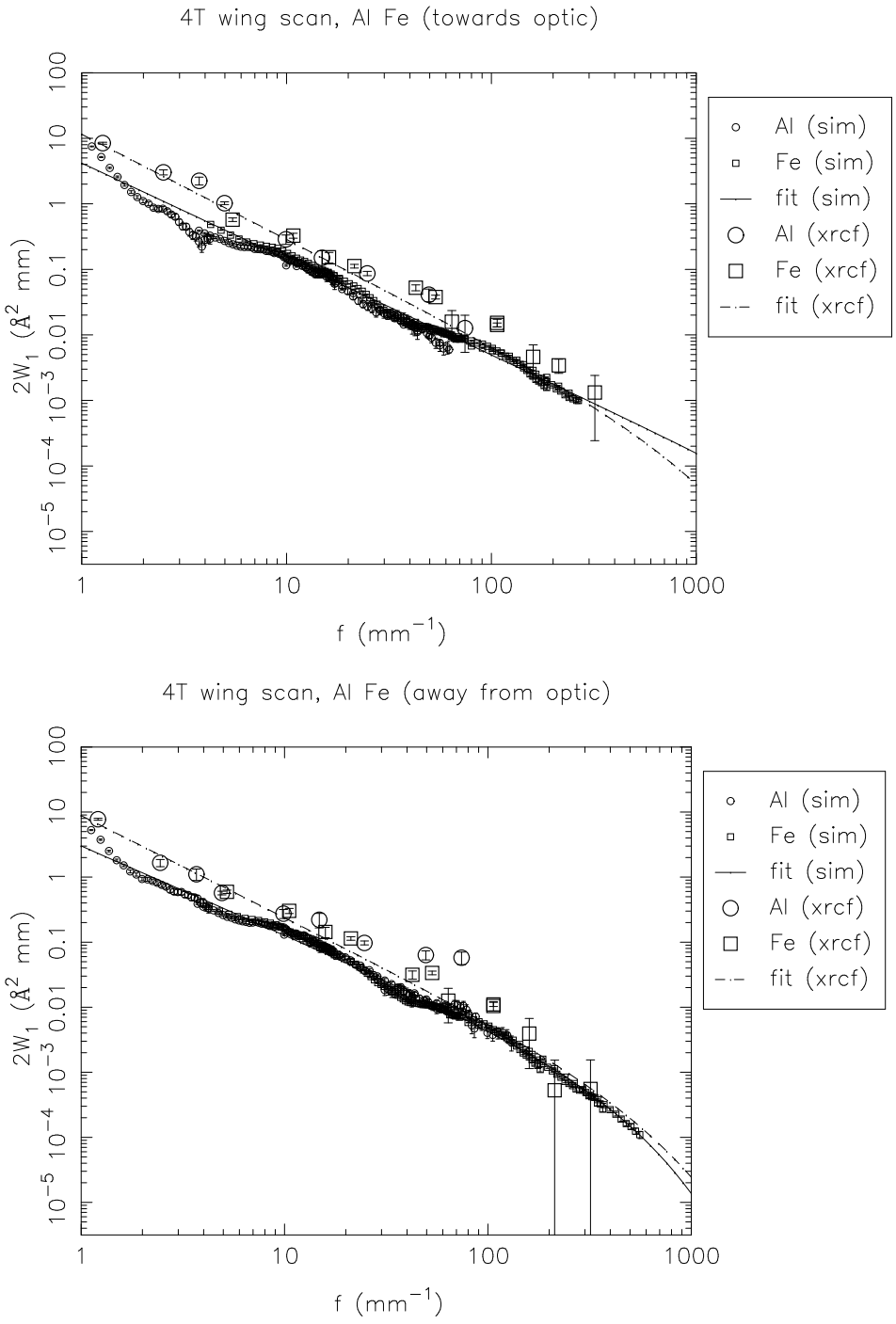

Figure 15.56: Shell 4T: $2W_1$ profiles, towards and away from the optic. XRCF data (*xrcf*) *vs.* raytrace data (*sim*).

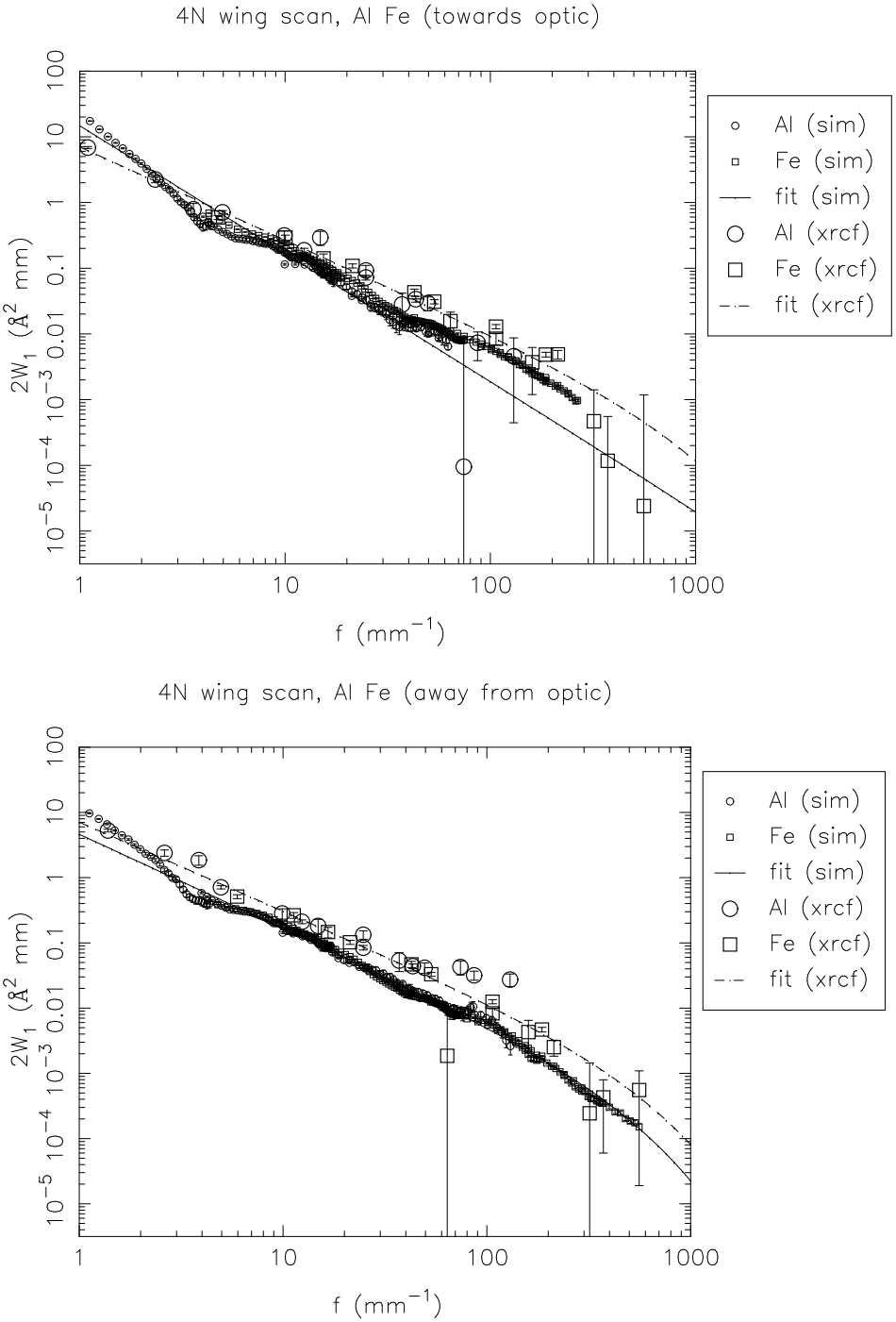

Figure 15.57: Shell 4N: $2W_1$ profiles, towards and away from the optic. XRCF data (*xrcf*) *vs.* raytrace data (*sim*).

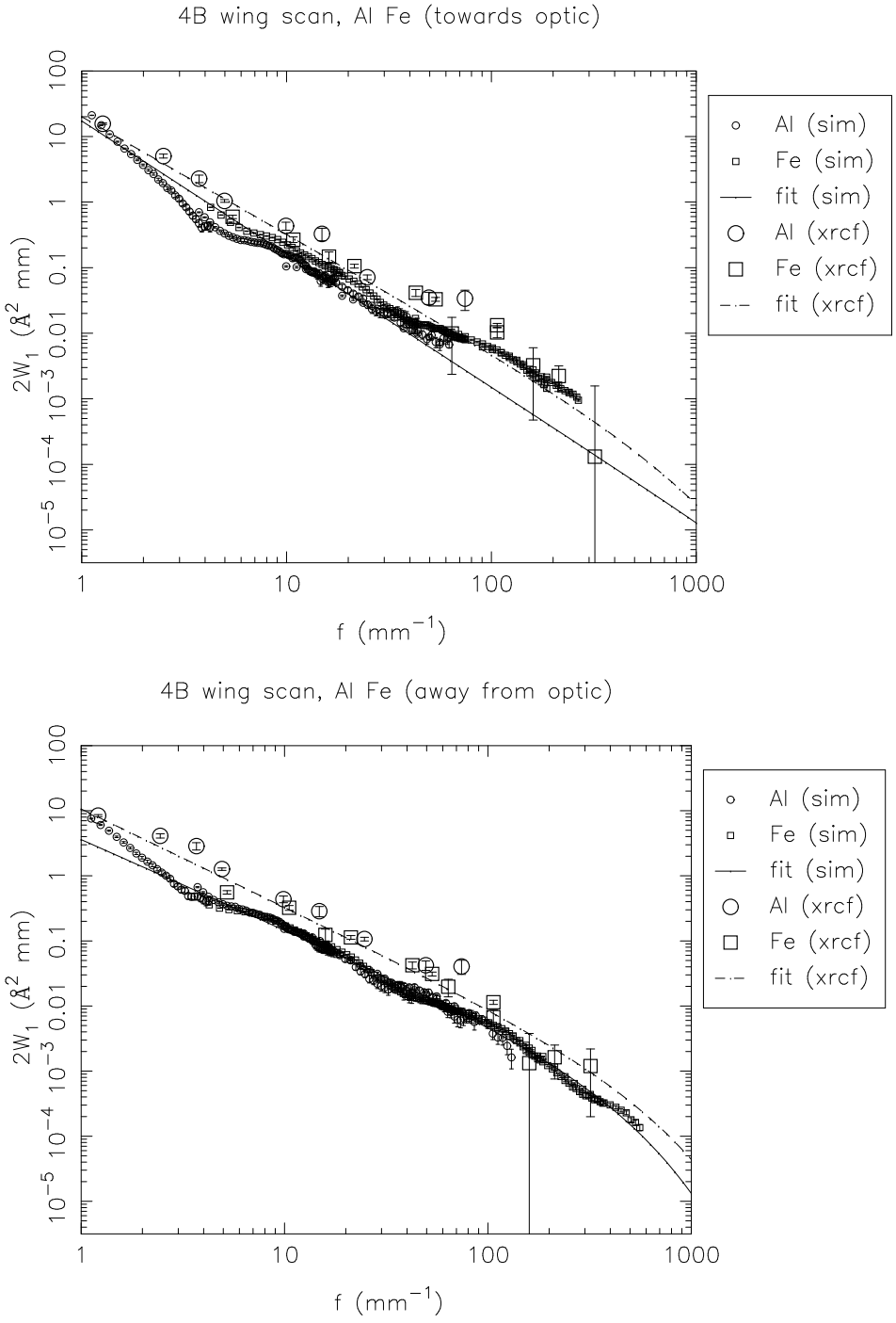

Figure 15.58: Shell 4B: $2W_1$ profiles, towards and away from the optic. XRCF data (*xrcf*) *vs.* raytrace data (*sim*).

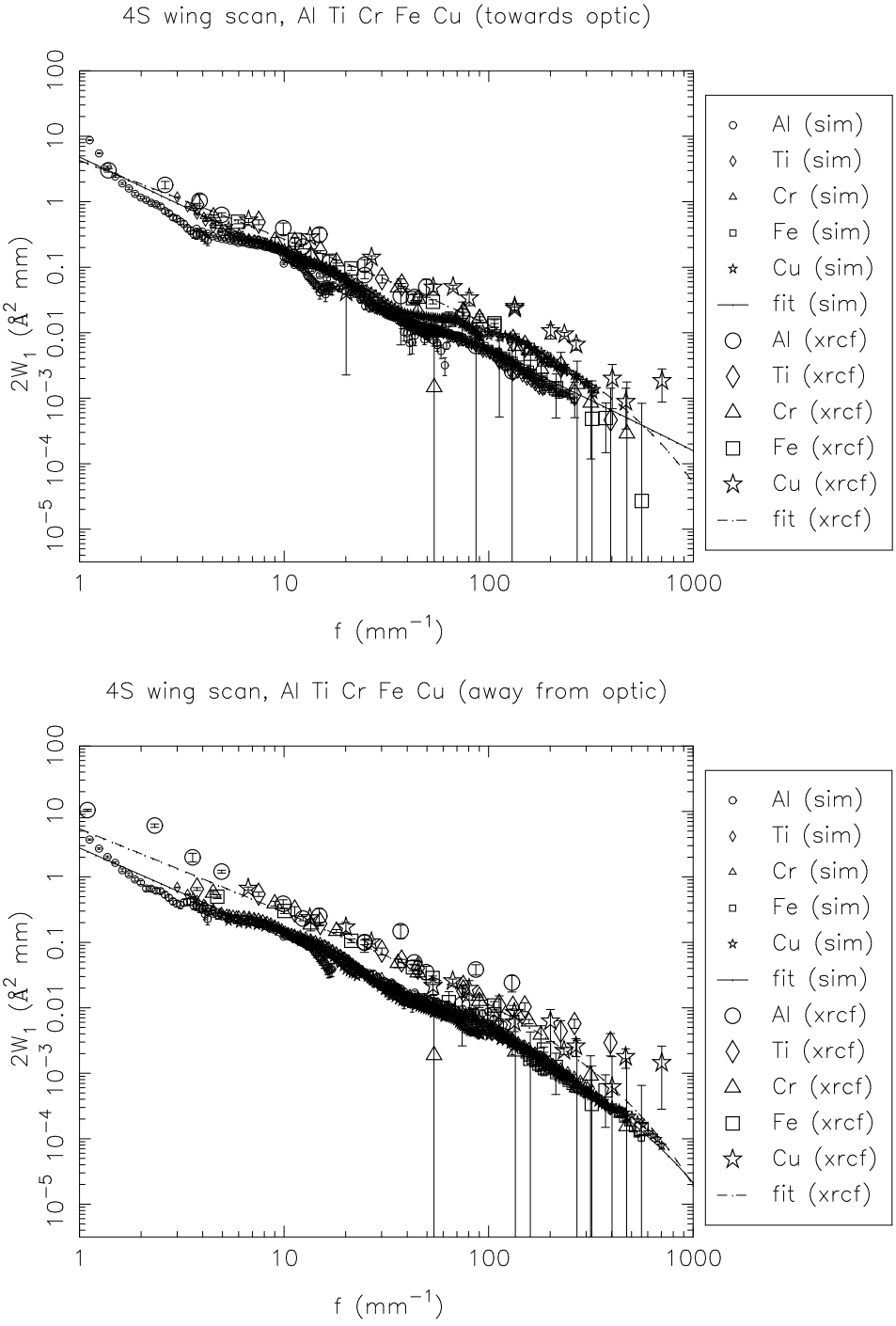

Figure 15.59: Shell 4S: $2W_1$ profiles, towards and away from the optic. XRCF data (*xrcf*) *vs.* raytrace data (*sim*).

15.5.4 Shell 6 scans

Table 15.14: Single quadrant wingscan $2W_1$ fits and mean square roughness (Raytrace simulation and XRCF data, Shell 6)

Type	Quad	Dir	a	b	c	σ^2_{1-10}	σ^2_{10-100}	$\sigma^2_{100-1000}$	σ^2_{1-1000}
sim	6T	in	5.441	1.365	190.000	8.323	3.083	0.432	11.838
sim	6T	out	4.866	1.334	190.000	7.680	3.052	0.454	11.187
sim	6N	in	5.842	1.387	190.000	8.751	3.089	0.415	12.254
sim	6N	out	5.273	1.329	190.000	8.366	3.364	0.506	12.236
sim	6B	in	10.047	1.644	1523.130	12.037	2.685	0.516	15.238
sim	6B	out	4.877	1.334	190.000	7.697	3.059	0.455	11.211
sim	6S	in	6.953	1.456	190.734	9.743	2.946	0.347	13.036
sim	6S	out	4.869	1.343	190.000	7.617	2.968	0.434	11.019
xrcf	T	in	3.785	1.027	172.717	8.264	6.412	1.558	16.233
xrcf	T	out	15.978	1.658	500.000	18.834	3.929	0.545	23.308
xrcf	N	in	4.932	1.081	107.681	10.005	6.201	0.810	17.017
xrcf	N	out	6.979	1.232	153.534	12.167	5.858	0.868	18.893
xrcf	B	in	28.228	2.147	800.000	22.787	1.581	0.088	24.456
xrcf	B	out	6.293	1.208	194.071	11.304	5.973	1.151	18.428
xrcf	S	in	4.812	1.089	135.492	9.745	6.277	1.061	17.084
xrcf	S	out	6.796	1.225	120.423	11.859	5.514	0.637	18.010

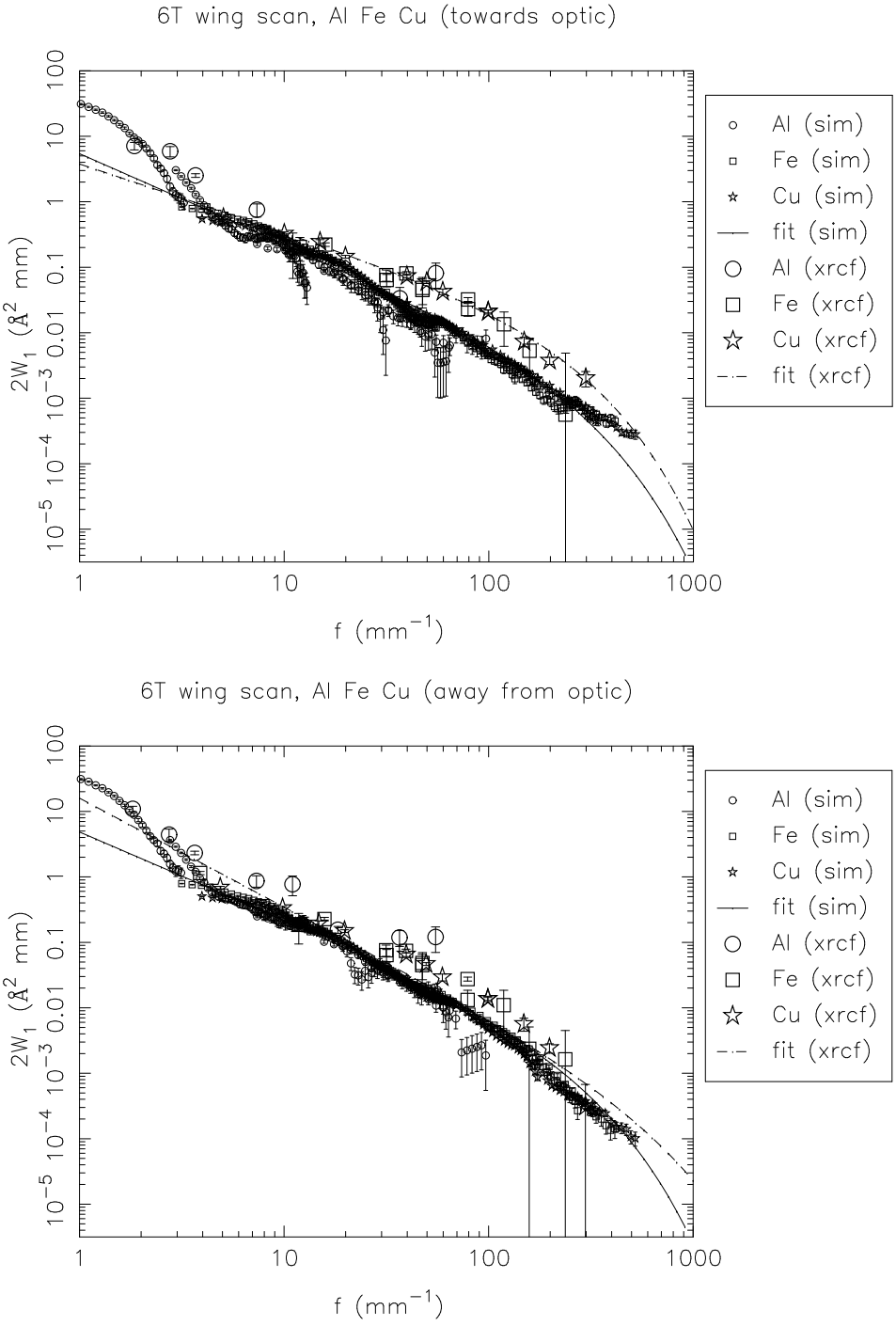

Figure 15.60: Shell 6T: $2W_1$ profiles, towards and away from the optic. XRCF data (*xrcf*) *vs.* raytrace data (*sim*).

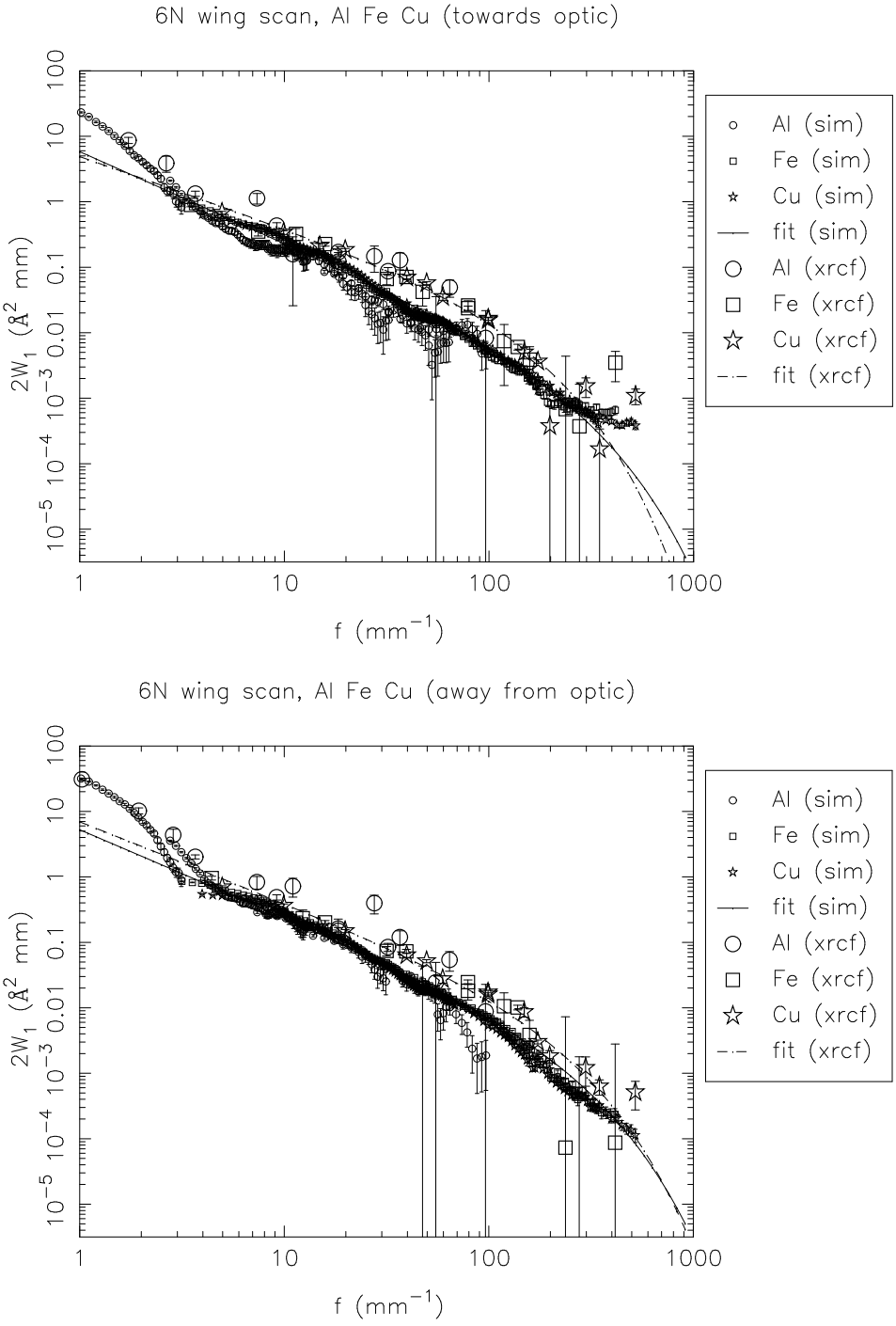

Figure 15.61: Shell 6N: $2W_1$ profiles, towards and away from the optic. XRCF data (*xrcf*) *vs.* raytrace data (*sim*).

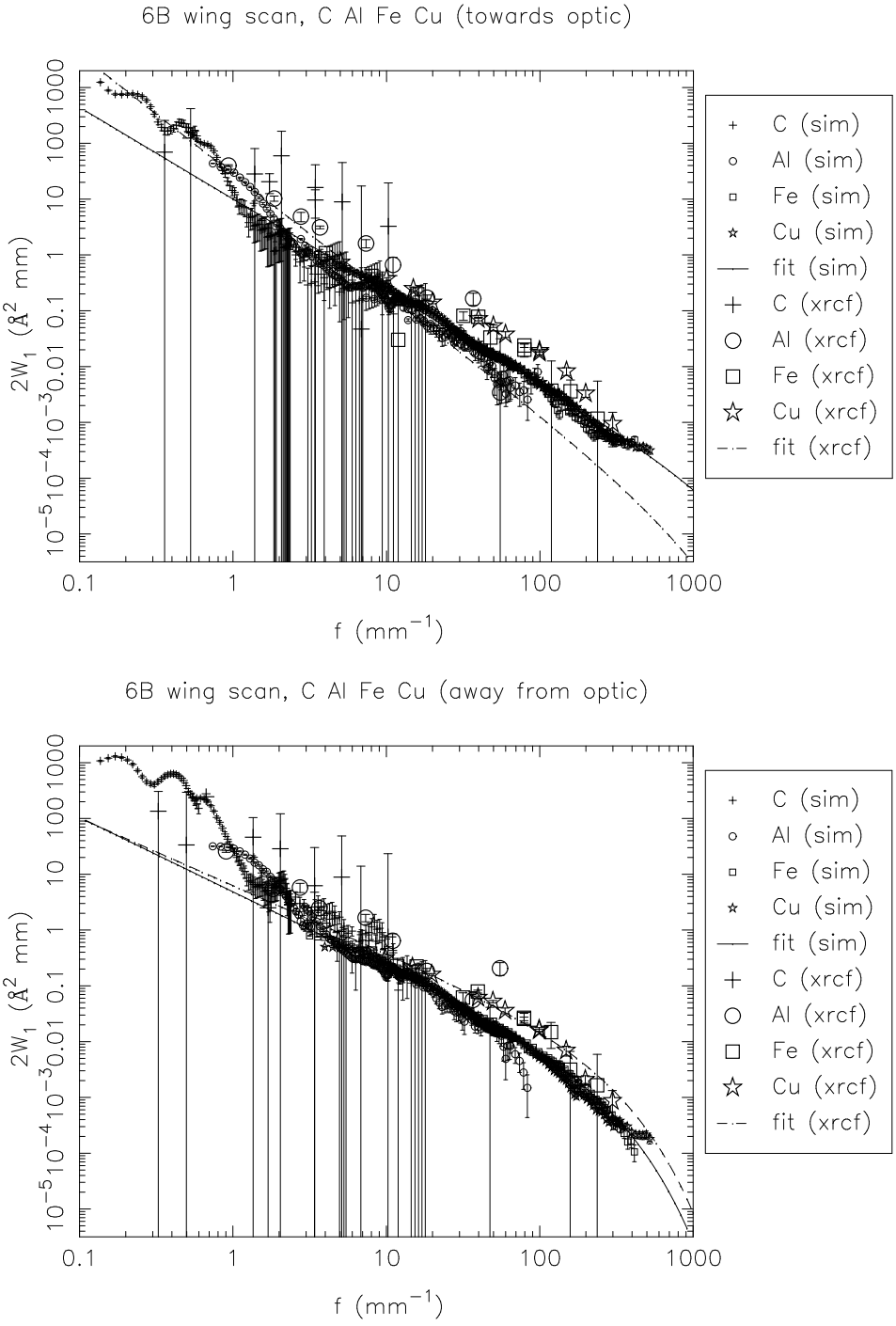

Figure 15.62: Shell 6B: $2W_1$ profiles, towards and away from the optic. XRCF data (*xrcf*) *vs.* raytrace data (*sim*).

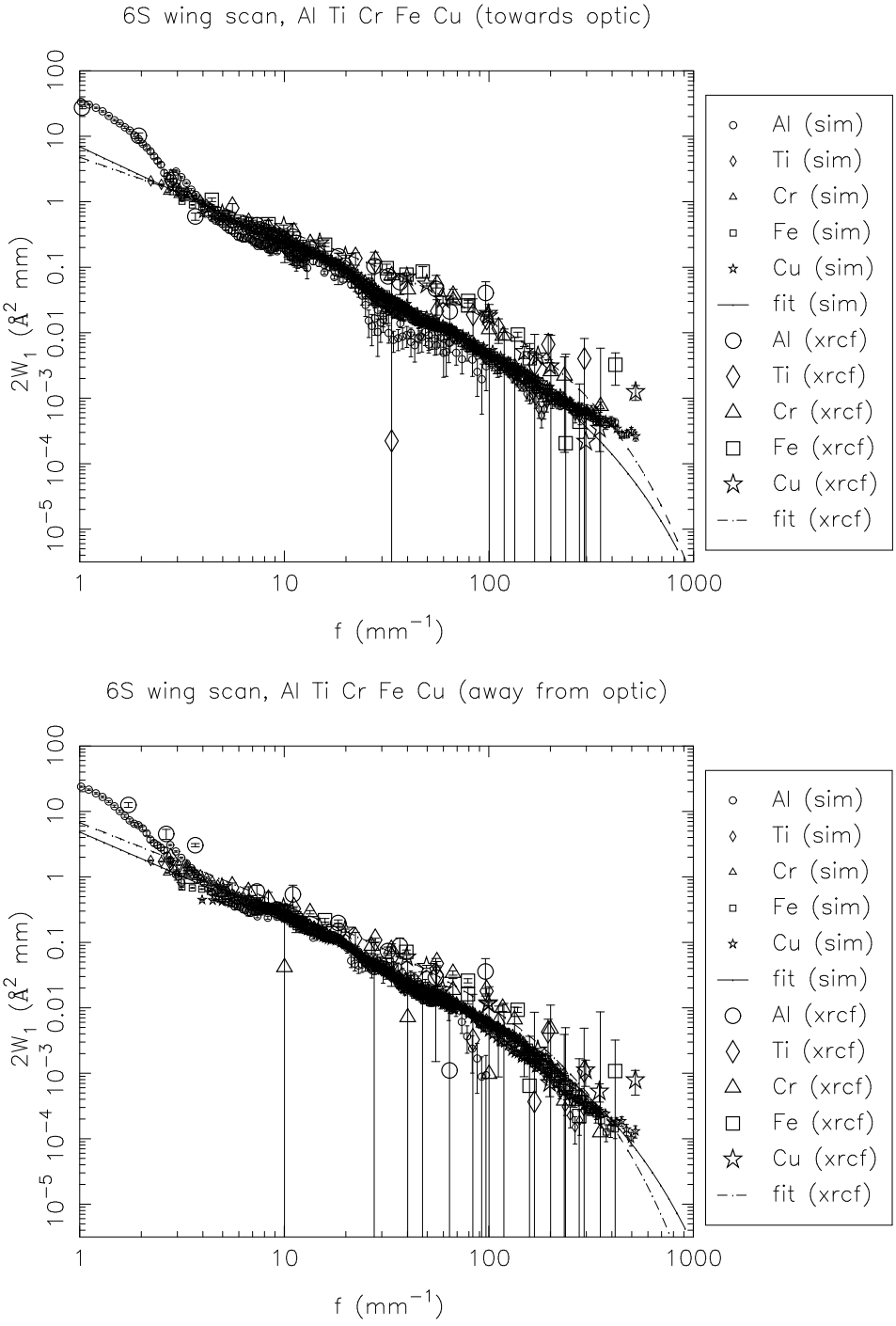

Figure 15.63: Shell 6S: $2W_1$ profiles, towards and away from the optic. XRCF data (*xrcf*) *vs.* raytrace data (*sim*).

15.5.5 2 Quadrant Scans

Table 15.15: Double quadrant wingscan $2W_1$ fits and mean square roughness (Raytrace simulation and XRCF data, Shell 4NS)

Type	Quad	Dir	a	b	c	σ^2_{1-10}	σ^2_{10-100}	$\sigma^2_{100-1000}$	σ^2_{1-1000}
sim	4NS	both	40.548	2.293	1000.000	29.687	1.480	0.062	31.230
xrcf	NS	both	38.249	1.763	800.000	41.332	6.912	0.893	49.138

Table 15.16: Double quadrant wingscan $2W_1$ fits and mean square roughness (Raytrace simulation and XRCF data, Shell 6NS)

Type	Quad	Dir	a	b	c	σ^2_{1-10}	σ^2_{10-100}	$\sigma^2_{100-1000}$	σ^2_{1-1000}
sim	6NS	both	49.306	2.280	1000.000	36.424	1.874	0.081	38.379
xrcf	NS	both	32.181	1.500	200.000	43.321	11.952	1.343	56.616

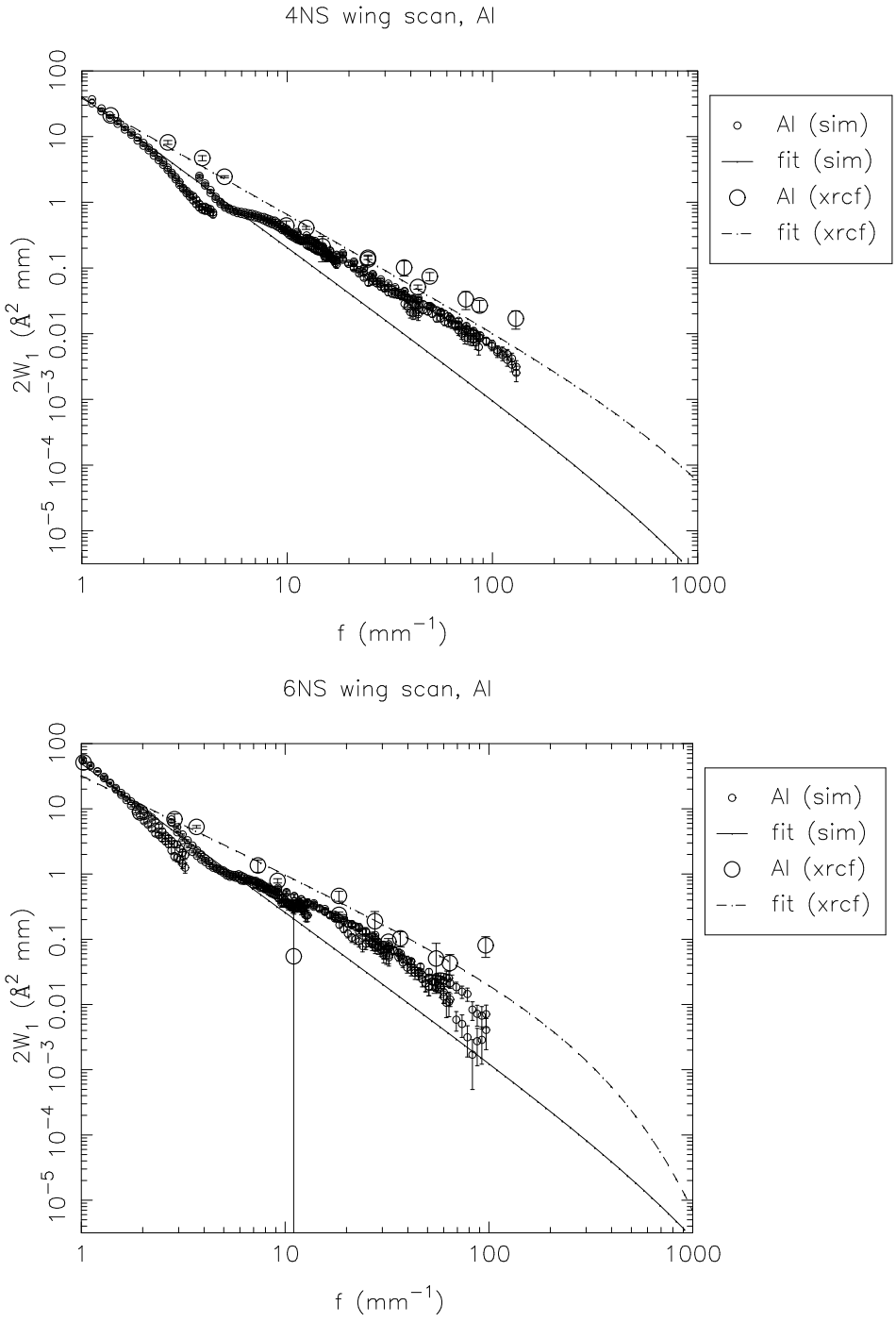

Figure 15.64: Double quadrant wing scans. Top: Shell 4 N and S quadrants: $2W_1$ profiles. Bottom: Shell 4 N and S quadrants: $2W_1$ profiles. XRCF data (*xrcf*) *vs.* raytrace data (*sim*).

15.6 Outstanding Analysis Issues

The analysis can be improved in a number of ways:

- In the case of the raytrace simulations, the fits to the surface brightness data and to the $2W_1$ data are not very good in many cases. The raytrace data show structure which is not captured by the simple fit function; on the other hand, the XRCF data set is sparse enough that a more elaborate fitting function is not really justified. In the raytrace fits, a lower limit to the exponential cutoff scale was specified. This was estimated by inspecting the resulting fits; the same cutoff value was used for all of the ψ fits (and similarly, for the $2W_1$ fits). Consequently, the fit at large radius can be bad. This affects the estimates of the fractional effective area outside the 35 mm pinhole (in the case of the ψ fits) or the mean square roughness σ^2 (in the case of the $2W_1$ fits).
- The truncation of the raytrace data sets to remove points affected by shutter vignetting was done by estimating a cutoff based on visual inspection of the curves. Raytraces with/without adjacent shutters in (shutters for other shells in the same quadrant) would provide a better handle on when the shutter vignetting kicks in.
- The surface brightness, ψ, is scaled by a a factor $2 \times 88/360$ to account for the fact that the experiment used a single quadrant at a time. This should be checked against raytraces for 1 *vs.* 4 quadrants open in a given direction, *e.g.*, nS *vs.* 1S3S4S6S, and for on-axis versus tilted HRMA cases. However, such raytraces would have to be much longer than the ones used in the current analysis. For now, this effect should more or less scale out because the raytraces were processed in the same way as the XRCF data.
- The comparison of scattering towards *vs.* away from the optic has only been given a cursory examination; further work needs to be done to determine whether there are discernible trends from quadrant to quadrant.
- The transverse wing scan data poorly understood at present. They are significantly below the corresponding in-plane measurements, but they need to be compared to raytraces in order to assess whether they are consistent with the scattering calculations.
- The double-quadrant wing scan data are *very* sparse; the analysis and interpretation of these data are incomplete at present.

15.7 Implications for Scattering Models

From the foregoing it is clear the raytrace scattering model needs to be improved. The raytraces consistently underpredict the pinhole effective area for the larger pinholes. The surface brightness plots and the $2W_1$ plots indicate a steeper power-law slope than is seen in the wing scan data. The mean-square roughness for spatial frequencies $1 - 1000$ mm^{-1} as deduced from the XRCF wing scan data are larger than that from the raytrace by about a factor of two for shells 1, 3, and 4, and about a factor 1.3 for shell 6. The disagreement between X-ray determinations and raytrace estimates get worse for larger spatial frequency f; this can also be seen in the figures in that the slopes of the $2W_1$ curves based on XRCF data tend to be flatter than the $2W_1$ curves obtained from the raytraces. The derived roughness parameter, σ^2, obtained by integrating the $2W_1$ functions over some passband, show puzzling variations: in quadrants 1S, 3T, 3N, 3B, 3S, and 4S, the σ^2 derived from the fits for scattering away from the optic surface are considerably larger than those for scattering towards the optic surface. In addition, the roughness derived from the double-quadrant scans is a factor of about 2 larger than that obtained from the single quadrant scans (taking into account the difference in normalization); this may result in part from the different illumination

pattern (tilted *vs.* untilted HRMA), but further investigation is warranted.